



University of Coimbra  
Faculty of Sciences and Technology  
Department of Physics

# Swept Source Optical Coherence Tomography for Small Animals: System Control and Data Acquisition

Master's Degree in Physics Engineering

José Adriano de Almeida Agnelo

September 2013





University of Coimbra  
Faculty of Sciences and Technology  
Department of Physics

# Swept Source Optical Coherence Tomography for Small Animals: System Control and Data Acquisition

Thesis submitted for obtaining the degree of Master in Physics Engineering

Supervisor: Prof. José Paulo Pires Domingues, Ph.D.

José Adriano de Almeida Agnelo

September 2013



# Acknowledgements

First, I would like to express my deepest thanks to my advisor, José Domingues, who, besides the timetable flexibility demonstrated in the project execution, gave me invaluable guidance and encouragement to conduct and finish this project.

I would also like to thank my labmate, Susana Silva, for her willingness, for helping me in the project setup and for giving me good suggestions.

Very special thanks to my wife, Vânia Tomé, who gave me the encouragement to undertake the Master Degree and who assisted me in the revision of the English text in this thesis.

Finally, I wish to express my gratitude to my old friend, fellow countryman and colleague in Coimbra University, Ricardo Coimbras, who helped me in the application programming developed.

To all, my sincere thanks.



# Abstract

In the field of biomedical research, small animals are very often used to develop, validate and test new techniques and therapies. Since imaging can give researchers the means to understand physiology, pathology and phenotypes of intact living systems similar to human beings, high speed swept source OCT for retinal imaging will be a valuable tool for retinal physiology research.

The main objectives of this project were to analyze and optimize the setup of the high speed swept source OCT started in a previous work (Oliveira, João. *Development of an optical coherence tomography for small animal retinal imaging*. A thesis submitted for the degree of Master in Biomedical Engineering, Coimbra University, September 2012) and to develop a program user-customizable which contains the basic components for system control, data acquisition, processing and 2D (B-Scan) image reconstruction.

After an introduction to a piece of history of OCT, the operation principle and different possible implementations are explained and compared. The explanation and experimental determination of different characteristic OCT parameters, such as optical resolution, sensitivity and noise, which essentially influence OCT image quality, are also discussed. After that, a summary overview of the development of OCT technology, in different medical applications, is made.

Next, a presentation and an explanation of the SS-OCT setup used in this project are performed. The system developed has the main components separated in several blocks: swept laser source, 2D scanning galvo system, fiber optic paths, couplers and circulators, reference and sample arms with respective collimators and objectives, balanced light detector and two boards, one for fast data acquisition and the other for controlling the position of the galvo system. So, the main characteristics and the choices made in the selection of these individual components are also described. Furthermore, some important optical and electronic parameters related to the assembly used are also determined.

The software developed is then explained and some results are presented. Currently, the application developed is able to provide flexible control of the data acquisition; A-scan range and T-scan size (control the X-axis of the galvo). The OCT data may be displayed only by sampling, real-time interference data, FFT (fast Fourier transform) and 2D (B-scan) images (5-6 images per second). The software also allows

recording the data and image into disk files (image data file can be saved into standard image files or into data values).

The sensitivity, sensitivity roll-off, dynamic range, axial resolution, and imaging speed parameters of the system were measured and are still below the intended.

The system needs to be improved and continued but I consider that there is progress regarding the previous work.



# Contents

<b>ACKNOWLEDGEMENTS .....</b>	<b>V</b>
<b>ABSTRACT .....</b>	<b>VII</b>
<b>CONTENTS .....</b>	<b>IX</b>
<b>LIST OF FIGURES .....</b>	<b>XI</b>
<b>INTRODUCTION.....</b>	<b>1</b>
<b>OVERVIEW OF OPTICAL COHERENCE TOMOGRAPHY .....</b>	<b>3</b>
2.1. - ARISING .....	4
2.2. - PRINCIPLES OF OPERATION AND BASIC SETUP .....	8
2.3. - DIFFERENT APPROACHES.....	12
2.3.1. <i>Time domain OCT (TD-OCT)</i> .....	13
2.3.2. <i>Frequency domain OCT (FD-OCT)</i> .....	15
2.3.3. <i>Comparison of different implementation techniques</i> .....	19
2.4. - OPTICAL PARAMETERS.....	20
2.4.1. <i>Point spread function</i> .....	20
2.4.2. <i>Axial resolution</i> .....	21
2.4.3. <i>Lateral resolution</i> .....	22
2.4.4. <i>Sensitivity</i> .....	23
2.4.5. <i>Dynamic range</i> .....	25
2.4.6. <i>Noise contributions</i> .....	26
2.4.7. <i>SNR - Signal-to-noise ratio</i> .....	28
2.5. - OCT PROGRESS AND APPLICATIONS IN MEDICINE.....	31
2.6. COMPARING OTHER BIOMEDICAL IMAGING TECHNIQUES .....	35
<b>EXPERIMENTAL SETUP AND ANALYSIS.....</b>	<b>39</b>
3.1 - SWEPT SOURCE OCT SETUP.....	40
3.2 - SWEPT SOURCE .....	43
3.2.1. <i>Light wavelength ranges for OCT</i> .....	43
3.2.2. <i>Swept sources for OCT</i> .....	45
3.2.3 - <i>Axsun Swept Source</i> .....	45

3.3. BALANCED DETECTOR .....	51
3.4. DATA ACQUISITION AND FUNCTION GENERATOR .....	55
3.5. FIXED FOCUS COLLIMATOR.....	58
3.6. SCAN LENS.....	59
3.7. 2D SCANNING GALVO SYSTEM.....	61
3.8. FIBER OPTIC CIRCULATOR .....	66
3.9. FIBER OPTICAL COUPLER.....	67
3.10. VARIABLE FIBER OPTICAL ATTENUATOR .....	68
3.11. GOLD MIRROR .....	68
<b>SYSTEM CONTROL AND DATA ACQUISITION SOFTWARE.....</b>	<b>71</b>
4.1. SOFTWARE DEVELOPMENT TOOLS.....	72
4.2. MAIN WINDOW .....	74
4.3. OPENING AND INITIALIZING THE BOARDS .....	75
4.4. CONFIGURATION OF THE DATA STREAMING.....	80
4.5. CONTROLLING THE GALVANOMETER.....	83
4.6. START DATA ACQUISITION AND CONTROL.....	85
4.7. SIGNAL PROCESSING AND DATA DISPLAY.....	91
<b>RESULTS AND PROJECT ANALYSIS .....</b>	<b>99</b>
<b>CONCLUSION AND FUTURE WORK.....</b>	<b>109</b>
<b>BIBLIOGRAPHY.....</b>	<b>111</b>

# List of Figures

Fig. 1 - Experimental setup for photographing light pulses in flight used by Duguay <i>et al.</i> [1].....	5
Fig. 2 - Schematic of picosecond range-gated angular scattering experiment used by Bruckner [2].....	5
Fig. 3 - Schematic of femtosecond optical ranging experiment used by Fujimoto <i>et al.</i> [3]...	5
Fig. 4 - Optics of the interferometer used to measure the length of the optic axis of the human eye <i>in vivo</i> used by Fercher <i>et al.</i> [4].....	6
Fig. 5 - Schematic of the first attempt to apply optical low-coherence reflectometry [5]. ....	7
Fig. 6 - Schematic of the first OCT scanner used by Huang <i>et al.</i> in 1991 [6].....	7
Fig. 7 - Schematic of a Michelson interferometer used in OCT.....	8
Fig. 8 - Schematic of Time Domain OCT System.....	14
Fig. 9 - Schematic of Spectral Domain OCT System .....	16
Fig. 10 - Schematic of Swept Source OCT System.....	17
Fig. 11 – Axial resolution as a function of the center wavelength and the bandwidth of the light source in air. [From Optics and Plasma Research Department, Risø National Laboratory, Denmark]. .....	22
Fig. 12 - Schematic of generic OCT sample arm optics .....	22
Fig. 13 - Low NA focusing maximizes lateral resolution and increases depth range. ....	23
Fig. 14 - High NA focusing minimizes lateral resolution and decreases depth range.....	23
Fig. 15 - Performance of FD/SS-OCT. (a) Sensitivity as a function of depth: R-number values of sensitivity roll-off were found to be 11.1 dB/mm; (b) axial resolution as a function of the depth; (c) point-spread function of the axial resolution near 0.7-mm depth [21].....	25
Fig. 16 - SNR as a function of reference-arm reflectivity (SNR). Also shown are the signal-to-receiver-noise ratio $SN_{rc}R$ , the signal-to-shot-noise ratio $SN_{sh}R$ and the signal-to-excess-noise ratio $SN_{ex}R$ . The calculations assume that $R_s = 1$ , $R_x = 0.0005$ , $\rho = 0.95$ A/W, the receiver noise current is 2 pA/Hz, an unpolarized optical source provides 20 mW of power at 1300 nm with 50-nm linewidth, and $B = 1$ MHz [22]. .....	30
Fig. 17 - Schematic for the operation of optical Doppler tomography. The basic OCT system is as described in the previous sections. The sample arm is held at some angle $\theta$ to the direction of flow. Therefore, an optical signal with wave-vector $k_0$ falls on a particle	

moving with velocity $u$ . The light scattered back into the sample objective is Doppler shifted and has wave-vector $k_d$ [42].	33
Fig. 18 - Experimental arrangement for polarization sensitive OCT. The polarizing beam-splitter (PBS) splits the optical output signal into its transverse electric (TE) and transverse magnetic (TM) parts [42].	34
Fig. 19 - Experimental set-up for thermal-light full field OCT. Instead of scanning the sample laterally, two-dimensional data are obtained simultaneously from each layer by the CCD. Time-domain reference mirror scanning acts as an axial probe [42].	35
Fig. 20 - Performance of most common medical imaging technologies with respect to image depth and achievable resolution. Adapted from [57].	36
Fig. 21 - Schematic of the swept-source OCT imaging system used. BD: Fixed gain balance detector; CIR: Single mode fiber optic circulator; CL: Fixed focus collimator; LN: Scan lens; SCDA - System control and data acquisition; GV: 2D Galvo system; AT: Variable fiber optical attenuator; OC: 2x2 Single mode fused fiber optic couplers. Adapted from [43].	40
Fig. 22 - Reference arm setup. CL: Fixed focus collimator; LN: Scan lens.	41
Fig. 23 - Pre-objective scanning setup (CL: Fixed focus collimator; LN: Scan lens; GV: 2D Galvo system).	41
Fig. 24 - Picture of the swept-source OCT imaging system used. BD: Fixed gain balance detector; CIR: Single mode fiber optic circulator; CL: Fixed focus collimator; LN: Scan lens; GV: 2D Galvo system; AT: Variable fiber optical attenuator; OC: 2x2 Single mode fused fiber optic couplers.	42
Fig. 25 - Absorption coefficient for freshly distilled water at 22 °C dependent on wavelength, in a logarithmic representation, adapted from [44]. The local minimum of the absorption coefficient close to 1060 nm allows retinal imaging at higher wavelengths, which can facilitate high-quality imaging of structures beneath the retinal pigment epithelium.	44
Fig. 26 - Axsun OCT Swept Source Engine - Benchtop Version.	46
Fig. 27 - Axsun Micro-Electro-Mechanical System (MEMS) Tunable Filter technology [48].	46
Fig. 28 - Time averaged power output of a typical SSOCT-1060 Engine [47].	47
<b>Fig. 29</b> - Trigger signal generated from the SSOCT-1060 engine after passing a digital delay/pulse generator	48
Fig. 30 - Axsun SS-OCT laser enclosure [47].	48
Fig. 31 - Schematic of external clock generator [43].	49
Fig. 32 - Clock signal obtained from an MZI signal [43].	49

Fig. 33 - The trigger, optical power, clock signal and clock frequency for a typical OCT-1060 engine. Adapted from [47].	50
Fig. 34 - Functional block diagram for the Thorlabs PDB145C balance detector [50].	51
Fig. 35 - Thorlabs PDB145C balance detector.	52
Fig. 36 - Typical responsivity curve for the Thorlabs PDB145C balance detector. Adapted from [50].	52
Fig. 37 - Typical frequency response curves of PDB145C [50].	53
Fig. 38 - Interferometric signal observed in an oscilloscope with a time scale of 500 ns/div.	53
Fig. 39 - Typical spectral noise curves of PDB145C [50].	54
Fig. 40 - XMC module X5-400M (left) and PCI express x8 module interface (right) [51].	56
Fig. 41 - XMC module X5-400M block diagram. Adapted from [51].	56
Fig. 42 - National Instruments PCI-6010 board (left); National Instruments CB-37F-LP terminal block (right below) and National Instruments SH37F-37M cable (right above) [51].	57
Fig. 43 - Thorlabs F260APC-C collimator photo (left) and schematic (right). Adapted from [54].	58
Fig. 44 - AR coating of the collimator Thorlabs F260APC-C as a function of the wavelength. Adapted from [54].	59
Fig. 45 - Thorlabs LMS03-BB lens photo (left) and typical OCT application (right) [54].	60
Fig. 46 - Scanning galvo systems GSVM002 from Thorlabs Inc. assembled on the experimental setup. Adapted from [54].	62
Fig. 47 - Scanning galvo systems GSVM002 from Thorlabs Inc.: Servo Driver Board Schematic Diagram [54].	63
Fig. 48 - Reflectance of the silver mirror scanning galvo systems GSVM002 as a function of the wavelength. Adapted from [54].	63
Fig. 49 - Schematic of an A-scan together with transverse scans (T-scan) to build up B-scan images.	64
Fig. 50 - Trajectory of light by rotation of the X-axis mirror keeping the Y-axis mirror stationary.	64
Fig. 51 - Signal currently used to control the X-axis mirror in 256 steps/points. The optical scan angle is $\theta_x \pm 2^\circ$ (the scaling factor of control board is 1 V/ $^\circ$ ) and the oscillatory period of the galvo mirror is $T \approx 175$ ms.	65
Fig. 52 - Thorlabs CIR1064-APC fiber optic circulator photo (left) and schematic (right) [54].	66
Fig. 53 - Photo of a bidirectional 2x2 single mode fused fiber coupler [54].	67

Fig. 54 - Schematic of a bidirectional 90:10 2x2 single mode fused fiber coupler [54].	67
Fig. 55 - Thorlabs VOA1064-APC variable fiber optical attenuator photo (left) and schematic (right) [54].	68
Fig. 56 - Reflectance of the gold mirror Thorlabs PF10-03-M01 as a function of the wavelength. Adapted from [54].	69
Fig. 57 - Main window of the OCTSystem program.	74
Fig. 58 - Flowchart of detection the boards.	75
Fig. 59 - Flowchart of opening and initializing the boards.	76
Fig. 60 - Data acquisition setup tab.	80
Fig. 61 - X5-400M Framework Logic Data Flow [51].	82
Fig. 62 - Settings of the X-axis mirror of the galvanometer to execute a T-scan.	84
Fig. 63 - Flowchart of start streaming.	86
Fig. 64 - Flowchart of data acquisition control and positioning of the galvo.	88
Fig. 65 - Flowchart of a new data packet receipt.	90
Fig. 66 - Display Buttons: Signal, FFT and Image.	91
Fig. 67 - Signal plot window.	91
Fig. 68 - Flowchart of processing and plotting a data frame.	93
Fig. 69 - FFT plot window.	94
Fig. 70 Flowchart of processing and plotting the FFT of a data frame.	95
Fig. 71 - B-Scan Image window.	96
Fig. 72 - Flowchart of processing and construction of the B-scan image.	98
Fig. 73 - FFT of the interference fringes for twelve positions, equally spaced (0-240 $\mu\text{m}$ ), of the sample arm (mirror). The first position (greater amplitude) is the PSF of the system.	99
Fig. 74 - Image of the A-Scan for a sample mirror on six different positions (0-500 $\mu\text{m}$ ). The galvo is not moving. The first image corresponds to the PSF of the system at $z = \Delta z$ .	100
Fig. 75 - Peak of the FFT signal for sixteen positions, equally spaced (0-300 $\mu\text{m}$ ), of the sample arm (mirror). The reference position (0 $\mu\text{m}$ ) is the PSF of the system at $z = \Delta z$ .	101
Fig. 76 - FFT of the PSF (black) and the noise floor (red) in a window centered at $z = \Delta z$ .	101
Fig. 77 - Peak maxima of the FFT for different PSFs depths (logarithmic representation) equally spaced by 20 $\mu\text{m}$ (0-300 $\mu\text{m}$ ).	102
Fig. 78 - Correlation between the FFT signal and the imaging depth $\Delta z$ . The reference mirror is moved with a micrometer in increments of 20 $\mu\text{m}$ (0-300 $\mu\text{m}$ ).	104

Fig. 79 - Image of the A-Scan for a sample mirror in position 0 and 500  $\mu\text{m}$ . The galvo is not moving. The first A-Scan corresponds to the PSF of the system at  $z = \Delta z$ .....104

Fig. 80 - Measurement of FWHM of the signal peak of the FFT for a PSF corresponding to the imaging depth at  $z=\Delta z$ .....105

Fig. 81 - B-Scan images for four different T-Scan ranges positions (256 - A, 512 - B and D, 1024 - C). The mechanical scan angle of the X-axis mirror is  $1^\circ$  (D) and  $2^\circ$  (A, B and C). The sample arm is a mirror. ....106

Fig. 82 - Sensitivities measured with a 57.6dB reflector. Blue, without an EO (electro-optic phase modulator) phase modulator; red, with an EO phase modulator [56]......107





# Chapter 1

## Introduction

Optical coherence tomography (OCT) is a non-invasive biomedical procedure able to provide three-dimensional imaging *in vivo*. It has a broad range of applications in medical diagnostic, of which the most prominent example is retinal imaging in the human eye.

In this technique, the optical beam is scanned transversally over the surface of the sample (usually biological tissue), whereas the intensity depth-resolved profile (with micrometer scale resolution and millimeter scale depth range) is continuously determined by measuring the time delays of backscattered light. This is realized on the basis of an interferometric measurement using a Michelson interferometer setup with a reference and a sample arms.

At the moment, research in the field of OCT focuses on the frequency domain approach based on wavelength-swept narrow-band light sources (operated in the near-infrared wavelength), where the optical frequency is changed repetitively, so that frequency is directly encoded in time. The wavelength needs to be repetitively swept over a broad wavelength range within a time of a few microseconds in order to guarantee sufficiently high axial resolution and imaging speed. Additionally, the swept light source must provide a narrowband instantaneous spectrum to enable a sufficient depth range.

One crucial parameter, which has become increasingly important, is acquisition speed because, for many medical applications, the possibility to acquire and processing, in a clinically relevant way, large sampled volumes in a minimum time is highly desirable. Among other reasons, it allows real time images.

This new need for high-speed image processing requires the inclusion of an image processing scheme comprising an efficient computational arrangement, faster data acquisition board with programmable firmware, graphic processor unit, and optimized software that enables real-time display of processed images at rapid line rates.



# Chapter 2

## Overview of Optical Coherence Tomography

A large part of the project focuses on the system control and data acquisition on an experimental setup for OCT. Therefore, it is essential to give an introduction to this biomedical imaging technique, which is the topic of this chapter.

After an introduction to a piece of history of OCT, the operation principle and different possible implementations are explained and compared. The following part of the section focuses on the explanation of different characteristic OCT parameters, such as optical resolution, sensitivity and noise which essentially influence OCT image quality. Besides addressing the theoretical background, the experimental determination of the parameters is discussed. After that, this section ends with an overview of the development of OCT technology also addressing different medical applications.

## 2.1. - Arising

OCT is an imaging technique frequently compared to ultrasound imaging, which is based on time delay measurement of backscattered sound waves. However, the measurement procedure using light waves instead of sound waves is different. Whereas in ultrasound-based diagnostic imaging technique the time delay is measured directly through electronics, this is not possible for optical imaging. The reason is due to the fact that the light speed exceeds  $\approx 10^5$  the speed of sound. Thus, in order to obtain an axial resolution of at least 100  $\mu\text{m}$ , time durations inferior to  $\approx 330$  fs would have to be resolvable, which is impossible with a purely electronic approach. Using light instead of ultrasound is advantageous since shorter wavelengths permit imaging at a higher resolution.

Moreover, no contact media is required, as the difference in optical impedance, the refractive index between air and tissue, is not as large as the difference in acoustic impedance between air and tissue. As a result, alternative methods had to be developed to solve this difficulty and thus allow measurement of optical echoes.

One first solution to this problem appeared in 1971, with Duguay *et al.* in their work *Ultrahigh Speed Photography of Picosecond Light Pulses and Echoes* [1], where a fast optical shutter, based on Kerr effect and triggered by intense picoseconds framing times ( $\approx 10$  ps), was presented that enabled photographing light pulses on their way through scattering liquid (Fig. 1). The authors were the first to suggest and recognize the possible medical applications of this technique, in other words, that high-speed optical gating could be used to see inside biological tissue, rejecting light backscattered from unwanted layers: *An incentive for pursuing this work may arise in the near future if subpicosecond pulses become readily available. These would permit picture ranging with submillimeter resolution and this might lead to interesting medical applications, such as seeing through the human skin* [1].

In 1978, Bruckner in his work, *Picosecond light scattering measurements of cataract Microstructure* [2], makes reference to the use of the picosecond range-gated light scattering technique (Fig. 2) to measure the microstructure of cataracts in the albino rabbits' eyes, with an axial resolution in the order of 1 mm.

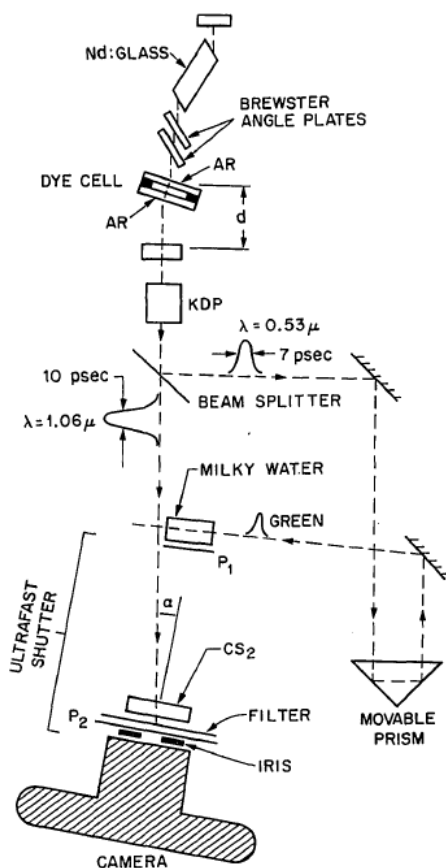


Fig. 1 - Experimental setup for photographing light pulses in flight used by Duguay *et al.* [1].

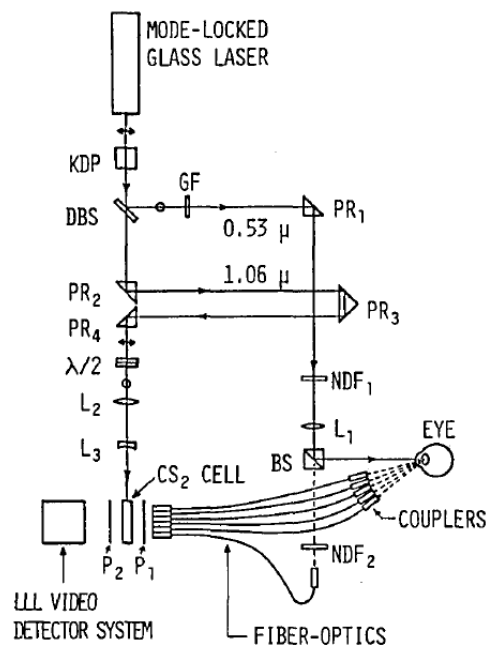


Fig. 2 - Schematic of picosecond range-gated angular scattering experiment used by Bruckner [2].

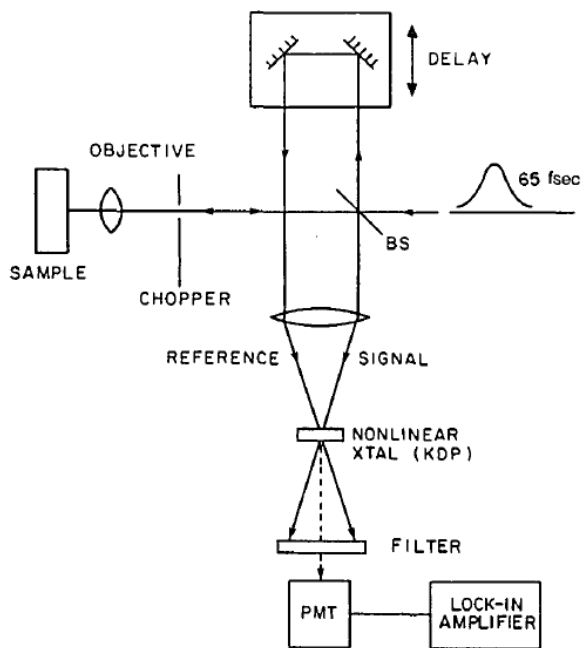
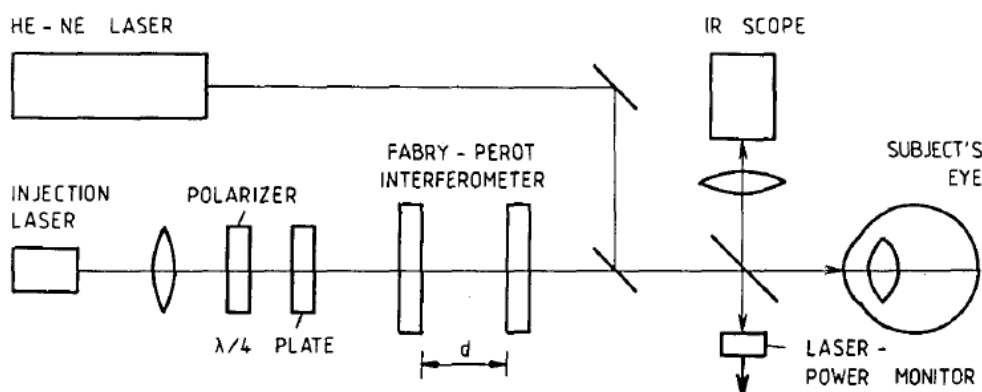


Fig. 3 - Schematic of femtosecond optical ranging experiment used by Fujimoto *et al.* [3].

Another approach in the investigation of the microstructure of biological systems is demonstrated by Fujimoto *et al.* in 1985 in their paper *Femtosecond optical ranging in biological systems* [3]. In this work, ultra-short optical pulses (femtosecond laser pulses) in combination with a background-free nonlinear cross-correlation setup are applied to measure the cornea in rabbits' eyes *in vivo* (Fig. 3).

Nonlinear cross-correlation gating is realized and generates a second harmonic generation signal only if the superposed pulses returning from reference and sample arm coincide temporally. This second-harmonic signal is used as an indicator for the path-length matching. Due to the pulse duration of  $\approx 65$  fs, boundaries separated by  $\approx 15$   $\mu\text{m}$  can be resolved [3]. However, the sensitivity, defined as the ratio of illuminating to the minimum detectable power, was  $\approx 70$  dB which is still too small for high-quality imaging of most of the biological tissue.

Finally, the breakthrough was achieved with the technique of white light interferometry or low coherence interferometry, which is based on using a spectrally broadband, temporally incoherent light source. Consequently, an interference signal can only be measured within very small path length differences that do not exceed the coherence length. In this way, the light which is backscattered from different closely spaced layers can be effectively distinguished. A first application of this technique in biological tissue *in vivo* to measure axial length of the human eye, was made by Fercher *et al.* as described in their paper *Eye-length measurement by interferometry with partially coherent light* [4], in 1987. In their work the interferometric technique was accomplished by using a statistically stationary fluctuating light beam emitted by a semiconductor laser and by analyzing the cross correlation of the field amplitudes of the measurement beam and the reference beam rather than that of the intensities (Fig. 4).



**Fig. 4** - Optics of the interferometer used to measure the length of the optic axis of the human eye *in vivo* used by Fercher *et al.* [4].

They considered the following: *If the laser emits 10 or more freely oscillating radiation modes we have, to a good approximation, statistically stationary field amplitude and phase fluctuations. In this case the light beam is a train of random light pulses with fluctuating amplitudes and phases. If the delay path length equals the measurement path length, interference will be seen and can be used as an indicator for the path-length matching. An estimate of the resolution can be obtained by considering the length of the corresponding light pulses* [4].

The semiconductor laser that was used in the experience has a spectral bandwidth  $\Delta\lambda$  of approximately 2 nm or a coherence length of approximately 25  $\mu\text{m}$  and they have succeeded in measuring the optical length of the eye within a precision of 0.03 mm.

Other biological applications were followed, such as the work of Clivaz *et al.*, *High-resolution reflectometry in biological tissues* [5], in August 1991, where optical low-coherence reflectometry was applied for the first time to investigate diffusive biological tissues with a single-mode fiber probe (Fig. 5). However, it was in November 1991 that Huang *et al.* [6] showed, for the first time, cross sectional images of biological tissue using light interferometry with an experiment setup (Fig. 6) which they called optical coherence tomography, an extension of the previous low-coherence reflectometer system.

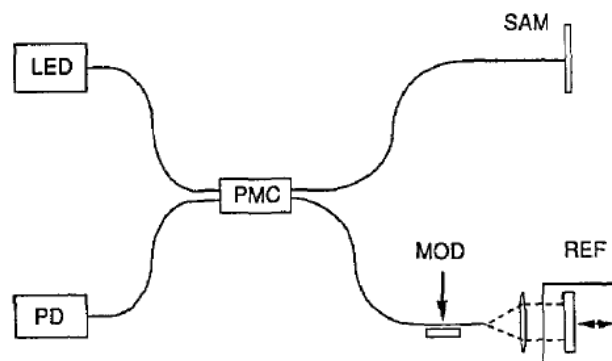


Fig. 5 - Schematic of the first attempt to apply optical low-coherence reflectometry [5].

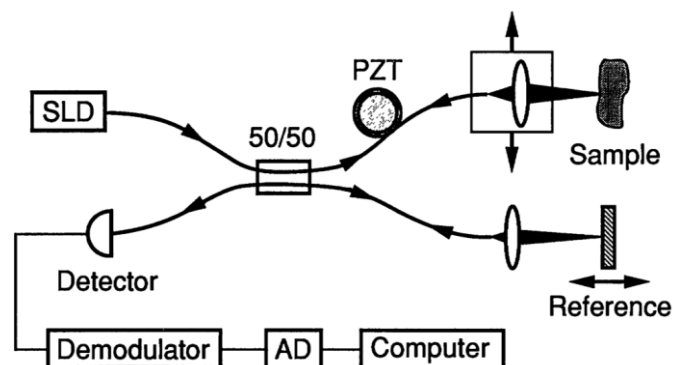


Fig. 6 - Schematic of the first OCT scanner used by Huang *et al.* in 1991 [6].

This was the first demonstration of the new field of OCT and, in their own words, *...is a promising technique for both basic research and clinical application* [1].

## 2.2. - Principles of Operation and Basic Setup

A typical OCT setup uses a standard Michelson Interferometer with a low-coherence light source (Fig. 7). OCT measures interference rather than back reflection through the use of an interferometer, which consists of a reference arm.

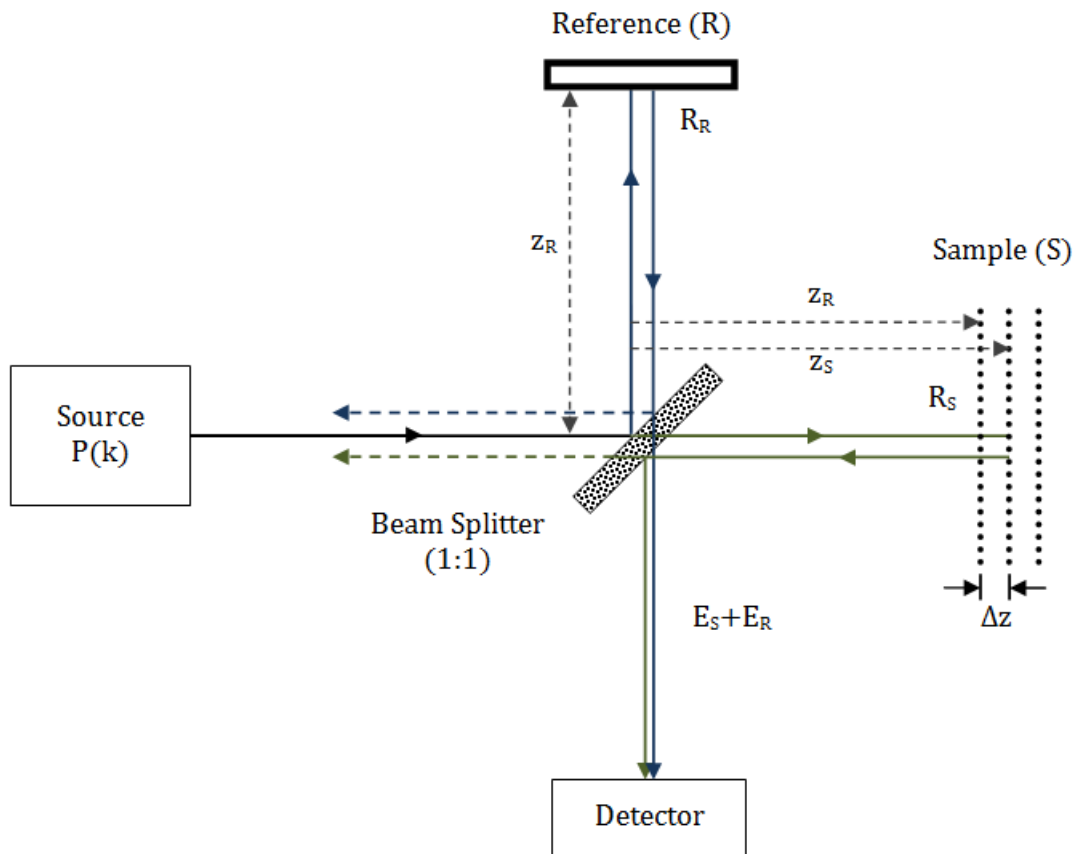


Fig. 7 - Schematic of a Michelson interferometer used in OCT.

The reference arm is needed since the back reflection intensity cannot be measured directly due to the high speed associated with the propagation of light, which is why OCT uses the intensity of interference to assess back reflection intensity indirectly [7].



In the interferometer, the incoming broadband beam source of light is split into the reference path and the sample path which are recombined after the back-reflection from the reference mirror and the multiple layers of the sample, respectively, to form an interference signal. The broadband nature of light causes interference of the optical fields which only takes place when the path lengths of the reference and the sample arms match the coherence length of the light. Part of this interference signal is then directed onto a detector and carries information about the sample at a depth determined by the reference path length.

The electric field originated from the source at a given position  $\mathbf{z}$  in function of time  $t$  is described as a superposition of monochromatic plane waves:

$$E(t) = \sum_{\mathbf{k}} E(\mathbf{k}, t) \quad (1)$$

The monochromatic wave at a defined position  $\mathbf{z}$  can be written as [7]:

$$E(\mathbf{k}, t) = a(\mathbf{k}) \cos(kz - \omega t - \varphi_{\mathbf{k}}) \quad (2)$$

where  $a(\mathbf{k})$  is the electric field amplitude, the wavenumber  $\mathbf{k}$  and the angular frequency  $\omega$  are respectively the spatial and temporal frequencies of the spectral component of the field having wavelength  $\lambda$ . They are linked by the dispersion relation [8]:

$$\frac{\omega}{k} = \frac{c}{n(\lambda)} \text{ where } k = \frac{2\pi}{\lambda}, \omega = 2\pi\nu \text{ and } \frac{c}{n(\lambda)} = \lambda\nu \quad (3)$$

where  $c$  is the vacuum speed of light and the wavelength  $\lambda$  and frequency  $\nu$  are coupled by the index of refraction  $n(\lambda)$  (which is wavelength-dependent in dispersive media).

In the following considerations, the analysis is restricted to a monochromatic wave. Furthermore, the reflection from only one single depth in the sample (distance  $\mathbf{z}_S$  to beam splitter) is considered. For simplicity reasons, the corresponding electric field reflectivity  $\mathbf{r}_S$  is assumed to be a real value and the power reflectivity  $\mathbf{R}_S = \mathbf{r}_S^2$ . This situation is equivalent to replacing the sample with a mirror of electric field reflectivity  $\mathbf{r}_S$  located at a distance  $\mathbf{z}_S$  from the beam splitter. Analogously, in the reference arm, the distance from the beam splitter to the reference mirror is  $\mathbf{z}_R$ , the electric field reflectivity of the reference mirror is denoted as  $\mathbf{r}_R$  and the power reflectivity  $\mathbf{R}_R = \mathbf{r}_R^2$ .

The following considerations also include phase jumps of the electric field of  $\pi$  for the reflection at the sample arm mirror and the reference arm mirror [7]. The optical beam splitter is assumed to be lossless with an ideal, wavelength-independent (achromatic) power splitting of 1:1. The following derivation considers phase jumps of the electric field of  $\pi$  for reflections at the beam splitter as well as, necessarily, phase shifts of

$\pi/2$  for light transmitted through the beam splitter [7]. This is a direct consequence of power conservation of the beam splitter and the resulting general expression of the scattering matrix for a lossless  $2 \times 2$  beam splitter [7]. Moreover,  $\mathbf{z} = \mathbf{0}$  is defined as the location of the beam splitter and the phase  $\varphi_{\mathbf{k}}$  is set to zero.

After light passing the interferometer, the electric field directly at output leading to detection is the sum of the electric fields  $\mathbf{E}_S$  (light returning from sample arm) and  $\mathbf{E}_R$  (light returning from reference arm), which is read [7]:

$$\begin{aligned} E_S(\mathbf{k}, t) &= \frac{1}{2} r_S a(\mathbf{k}) \cos\left(2kz_S - \omega t + \frac{\pi}{2}\right) \\ E_R(\mathbf{k}, t) &= \frac{1}{2} r_R a(\mathbf{k}) \cos\left(2kz_R - \omega t + \frac{\pi}{2}\right) \end{aligned} \quad (4)$$

where the factor 2, in  $z_S$  and  $z_R$ , accounts the round-trip path length to each sample/reference reflection.

What is measured by the detector is the irradiance and not the electric field, then assuming an optical detector with an electronic bandwidth  $B_W$ , corresponding to integration time  $T_i$  [9]:

$$T_i = \frac{1}{2B_W} \quad (5)$$

with a detector responsivity  $\rho$ , supposed to be independent from  $\mathbf{k}$ , the detector current  $I_D(\mathbf{k})$  can be written as the time average of the square of the electric field [8]:

$$I_D(\mathbf{k}) = \gamma \rho \langle |E_R(\mathbf{k}, t) + E_S(\mathbf{k}, t)|^2 \rangle_{T_i} \quad (6)$$

where,  $\gamma$  is a proportionality factor and:

$$\langle x(t) \rangle_{T_i} = \frac{1}{T_i} \int_0^{T_i} x(t) dt \quad (7)$$

is denoted as the average over the time  $T$ .

In the following, the identities are used:

$$\cos(a) \cos(b) = \frac{1}{2} \cos(a - b) + \cos(a + b)$$

$$\Delta z = z_R - z_S \quad (8)$$

$$\langle \cos^2(kz - \omega t) \rangle_T = \frac{1}{2}$$

$$\langle \cos(kz - 2\omega t) \rangle_T = 0$$

Under consideration of equations 4-8 and substituting them by the power reflectivities  $\mathbf{R}_R$  and  $\mathbf{R}_S$  and the spectral power of the light source [7]:

$$P(k) = \frac{1}{2} \gamma a(k)^2 \quad (9)$$

the detector current  $I_D(\mathbf{k})$  reads [8]:

$$I_D(k) = \frac{\rho}{4} P(k) (\mathbf{R}_R + \mathbf{R}_S \pm 2\sqrt{\mathbf{R}_R} \sqrt{\mathbf{R}_S} \cos(2k\Delta z)) \quad (10)$$

This eliminates the terms dependent upon the temporal angular frequency  $\mathbf{w} = 2\pi\mathbf{v}$ , which is reasonable since  $\mathbf{v}$  oscillates much faster than the response time of any practical detector [8].

The last equation (eq. 10) shows that the detector current consists of three different contributions. The first two terms only reflect the spectral power of the light source (DC irradiance from sample and reference arms) and do not carry any important information for OCT since they are independent of  $\Delta z$ . By contrast, the last interference term depends on  $\Delta z$  and is the basis for the derivation of the intensity depth profile.

Since under typical OCT conditions the backscattered power from the sample is very small ( $\mathbf{R}_S \ll \mathbf{R}_R$ ), the second term can be neglected.

Note that the last term is proportional to  $\sqrt{\mathbf{R}_R \mathbf{R}_S}$ . This is why OCT is based on heterodyne gain, meaning that the signal gain can be adjusted via control of the power of the returning reference arm light. Therefore, very high sensitivities superior to 100 dB can be achieved, which is crucial to enable high-quality imaging.

So far, the analysis has been restricted to a single reflection from one depth in the sample. An extension of the treatment, considering  $\mathbf{n}$  reflections with different  $\mathbf{r}_S(\mathbf{n})$  but neglecting possible autocorrelation terms, yields the interference term [8]:

$$\frac{\rho}{2} P(k) \sqrt{\mathbf{R}_R} \sum_n (\sqrt{\mathbf{R}_S(n)} \cos(2k\Delta z(n))) \quad (11)$$

Until now, the analysis has been based on a monochromatic wave. However, the derivation of the depth profile  $\mathbf{R}_S(\Delta z)$  of the backscattered intensity requires the use of a light source generating a wide range of frequencies. There are different approaches in OCT that enable a determination of  $\mathbf{R}_S(\Delta z)$ .

## 2.3. - Different Approaches

In OCT, one can distinguish between different implementations which differ considerably on the procedure how the intensity depth profile, which is called A-scan, is determined. On the one hand, there is the time domain OCT (TD-OCT), which is the traditional technique that was exclusively used during the first years after the introduction of OCT and is based on white light interferometry.

The interference fringe signals are detected as a function of optical time delay between the sample and reference arms. The envelope of the interference fringe signals yields the depth profile for the sample.

All spectral components of a broadband light source are measured instantaneously with a photodiode. Due to the small temporal coherence, only light that is backscattered from depths very close to the zero delay point contributes to the signal. Thus, by moving the reference mirror and therefore by shifting the point of zero delay in the sample, a whole A-scan can be recorded. The time required for one A-scan is given by the speed of the mirror movement.

On the other hand, there is the field of frequency domain OCT (FD-OCT), sometimes also referred to as Fourier domain OCT, which emerged a few years later and where almost all OCT research is currently focused on, since it provides many advantages compared to TD-OCT. In FD-OCT, the reference arm mirror is static and a further differentiation is made between spectral domain OCT (SD-OCT) (also called spectrometer based OCT), and swept source OCT (SS-OCT) (also called optical frequency domain imaging or OFDI).

SD-OCT also requires a broadband light source. However, instead of a photodiode, a spectrometer is used to measure the different spectral components of the light after the interferometer.

In SS-OCT, the principle is similar. Here, a narrowband light source, where wavelength changes with time and over a large wavelength range, a so called wavelength-swept light source, is used and the light from the output of the interferometer is recorded during this wavelength sweep using a photodiode. However, in both cases the measured interference signal (in the space of  $\mathbf{k}$  or time  $\mathbf{t}$ ) must be Fourier transformed after data acquisition, since the backscattered intensity from each depth  $R_s(\Delta z)$  is proportional to a

certain frequency component of the signal. Unlike TD-OCT, in FD-OCT the information of backscattered intensity from all depth is contained in the entire A-scan signal.

### 2.3.1. Time domain OCT (TD-OCT)

In TD-OCT, an interference pattern is obtained by moving the reference mirror in a linear fashion to change the reference path length and match multiple optical paths due to reflections within the sample (Fig. 8).

The photodetector detects the average intensity over all range of frequencies. Therefore, for a specific reference mirror position, the detector current is obtained by integration over  $\mathbf{k}$  [8]:

$$I_D(z_R) = \int_0^\infty \tilde{I}_D(\mathbf{k}) d\mathbf{k} \quad (12)$$

where  $\tilde{I}_D(\mathbf{k})$  is the spectral density of the current.

In the following equation, the spectrally integrated power of the source is introduced [8]:

$$P_0 = \int_0^\infty \tilde{P}(\mathbf{k}) d\mathbf{k} \quad (13)$$

where  $\tilde{P}(\mathbf{k})$  is the power spectral density of the light source, which is assumed to have a Gaussian shape (Gaussian shaped light source spectrum is convenient in modeling OCT, because it approximates the shape of actual light sources);  $\mathbf{k}_0$  is the center wavenumber and  $\Delta\mathbf{k}_{FWHM}$  is the full-width of half maximum (FWHM) of  $\tilde{P}(\mathbf{k})$ .

Assuming a reflection from a single depth in the sample  $\mathbf{z}_S$ ,  $\tilde{I}(\mathbf{k})$  is given by equation 10 (replacing  $\mathbf{P}(\mathbf{k})$  by  $\tilde{P}(\mathbf{k})$  and  $\mathbf{z}_R = \Delta\mathbf{z} + \mathbf{z}_S$ ).

Integrating  $\tilde{I}(\mathbf{k})$  over  $\mathbf{k}$  then results in a detector current that reads [8]:

$$I_D(z_R) = \frac{\rho}{4} P_0 \left( R_R + R_S \pm 2\sqrt{R_R R_S} e^{-\frac{(z_R - z_S)^2 \Delta\mathbf{k}_{FWHM}^2}{4 \ln 2}} \cos(2k_0(z_R - z_S)) \right) \quad (14)$$

The detected signal consists of a DC term and an interference term that contains the sample information.

Obviously, the interferometric part includes two terms depending on  $\mathbf{z}_R$ . The envelope of the signal is proportional to  $\sqrt{R_R R_S}$  and decays with the exponential term.

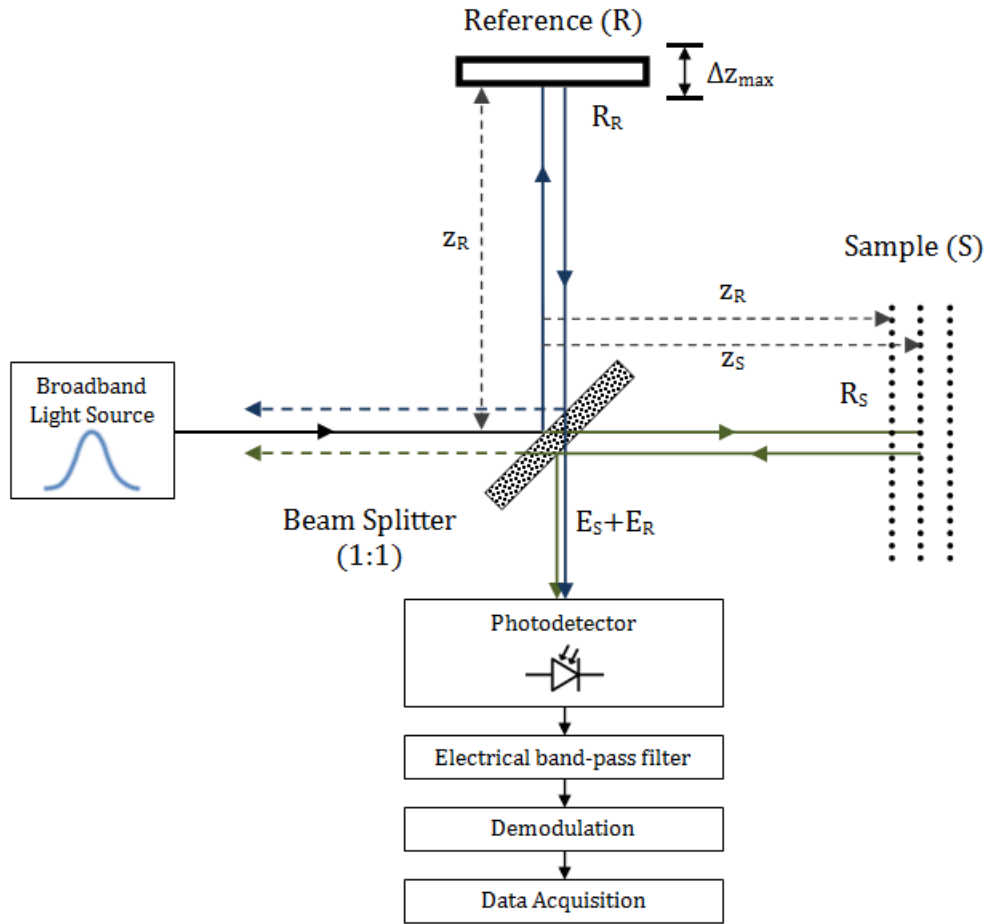


**Fig. 8** - Schematic of Time Domain OCT System

Additionally, the signal is modulated by a co-sinusoidal carrier wave modulation with a frequency proportional to the center wavenumber  $k_0$ .

Generally, the function describing the decay of the envelope is the so called coherence function  $\gamma(\Delta z)$  which is directly linked to the spectral power density of the light source  $\tilde{P}(k)$  by Fourier transformation **FT** [8]:

$$\gamma(z) \overset{\text{FT}}{\leftrightarrow} \tilde{P}(k) \quad (15)$$

Note that equation 15 is a direct consequence of the Wiener-Khinchin theorem, which states that spectral power density and the electric field autocorrelation function are linked by Fourier transformation [8].

Since, in TD-OCT, the reference arm length  $z_R(t)$  is scanned over the desired imaging range  $\Delta z_{max}$  in the A-scan time  $\Delta T$  with a constant speed  $v$ :

$$v = \frac{\Delta z_{max}}{\Delta T} \quad (16)$$

the detector current becomes time-dependent and the carrier modulation frequency  $\nu$  reads [10]:

$$v = \frac{1}{\pi} k_0 v \quad (17)$$

To ensure optimal sensitivity and resolution, an electrical band-pass filter is used centered at the carrier frequency with an optimal bandwidth  $B_w$ , which equals approximately twice the FWHM power bandwidth of the signal and therefore is proportional to the spectral width and the scan speed [10]. Furthermore, the signal is demodulated before data acquisition. In this way, the DC-offset can be rejected and the signal envelope can be measured allowing the determination of  $R_s(\Delta z)$ .

### 2.3.2. Frequency domain OCT (FD-OCT)

In FD-OCT, the reference mirror is static and the backscattered intensity profile is derived by Fourier transformation of the signals generated by measuring the different spectral components. One possibility to apply FD-OCT is spectral domain OCT (SD-OCT), which is based on a spectrometer used for detection after the interferometer output. A typical SD-OCT system consists of a broadband light source, a Michelson interferometer and a spectrometer (Fig. 9).

The first attempts to use this technique occurred in 1995, when Fercher *et al.* [11] enabled the measurement of intraocular distances on a model eye and on a human eye *in vivo*. Only in 2002, SD-OCT was first demonstrated, showing *in vivo* tomograms of human retina obtained by Fourier domain optical coherence tomography [12].

The depth profile of the measured sample is retrieved by spectral analysis of the spectral interferograms detected by a spectrometer. Typically, the spectrometer consists of a diffractive grating which disperses the light, an objective lens and a pixel array integrated in a line scan camera which simultaneously measures the different spectral components.

The A-scan time  $\Delta T$  is given by the time the camera needs to read out all pixels. Since the signal of each pixel is integrated over a time  $\Delta T$ , the electrical bandwidth  $B_w$  is [9]:

$$B_w = \frac{1}{2\Delta T} \quad (18)$$

Assuming a single reflection from the sample and a detection of all spectral components with infinite accuracy, the spectrally dependent current reads as denoted in equation 10.

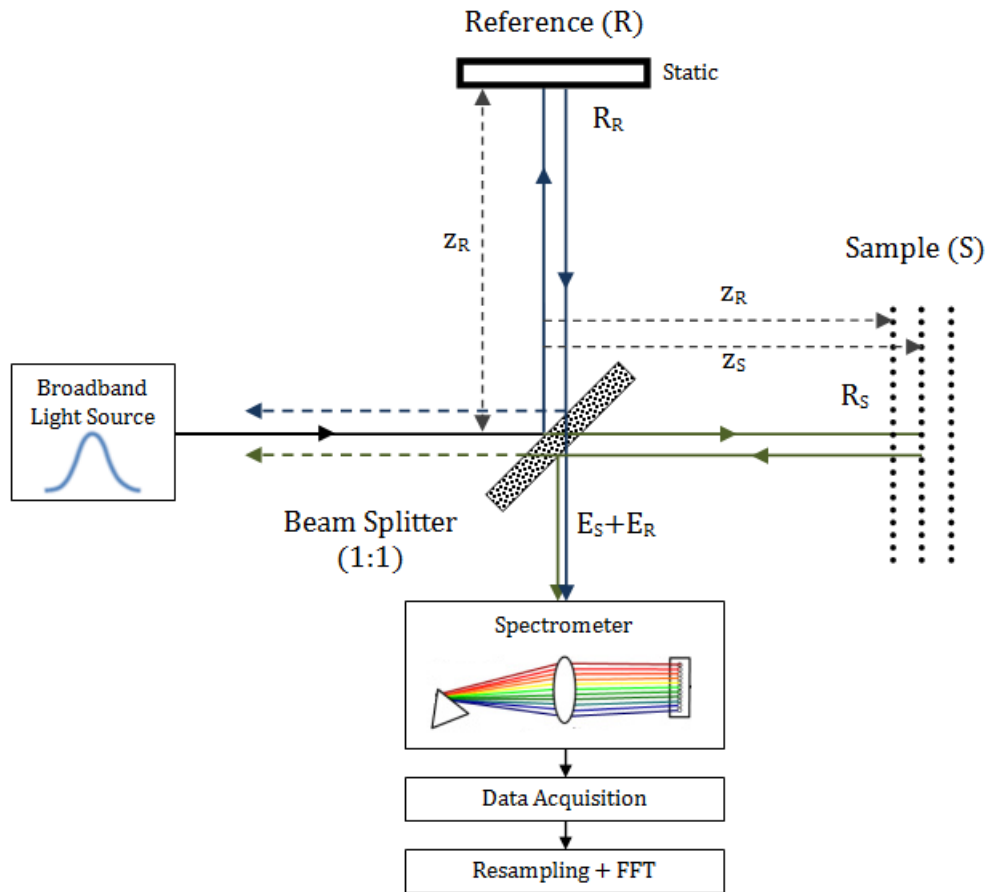


Fig. 9 - Schematic of Spectral Domain OCT System

The second technique associated to the field of FD-OCT is swept source OCT (SS-OCT), which is not based on using broadband light sources, but on narrowband wavelength-swept light sources instead (Fig. 10). The principle has already been used since the early 1980's for measurements in fiber optics but the first demonstration of this technique for OCT was only presented in 1997 [13].

The wavenumber of the light generated in a wavelength-swept light source changes repetitively and monotonically within a certain range  $\Delta k$  as a function of time  $t$ . Unlike SD-OCT, where different spectral components are separated in space, in SS-OCT the spectral information is encoded in time.

The segment of the light field comprising the spectral width  $\Delta k$  (the total optical bandwidth through which the narrowband source is swept) and the temporal width  $\Delta T$ , which defines the A-scan time, is called a sweep.



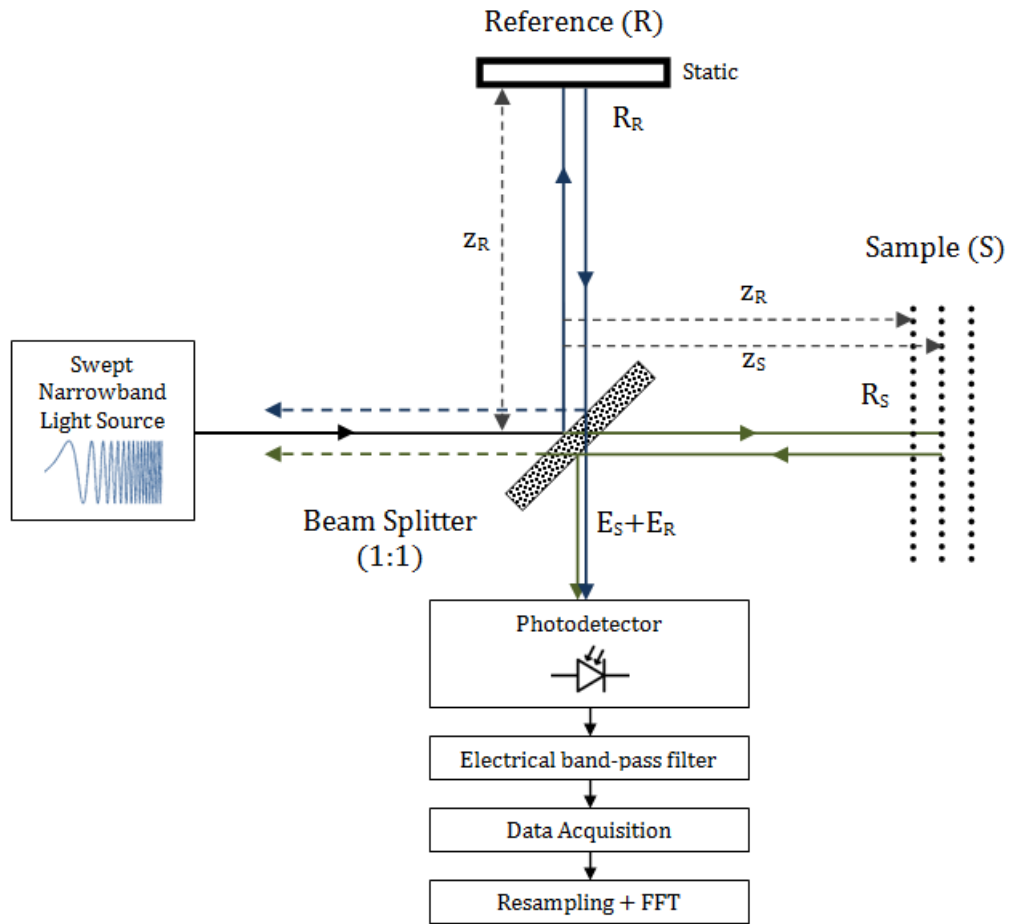


Fig. 10 - Schematic of Swept Source OCT System

To simplify things, only a single ascending sweep is considered which is assumed to exhibit a linear time-wavenumber characteristic. The wavenumber then can be written as [14]:

$$k(t) = k_i + \frac{\Delta k}{\Delta T} t \quad (19)$$

where  $k_i$  is the starting wavenumber.

Thus, assuming a single reflection from the sample, the detector current, which is measured with the photodetector, can be derived in a similar way as shown earlier and reads [8]:

$$I_D(t) = \frac{\rho}{4} P(k(t)) (R_R + R_S \pm 2\sqrt{R_R}\sqrt{R_S} \cos(2k(t)\Delta z)) \quad (20)$$

Substituting the interferometric term of  $I_D(t)$  by  $k(t)$ , it will oscillate with an angular frequency  $\omega_I$ :

$$\omega_I = 2 \frac{\Delta k}{\Delta T} \Delta z \quad (21)$$

This result can easily be understood if one considers the fact that the optical frequencies of the two light waves, which return from both interferometer arms, incident on the photodiode, always differ by an amount that is proportional to the path length difference  $2\Delta z$ . The detectable signal then simply exhibits a frequency equal to the difference frequency or beat frequency of these two light waves. Therefore, in SD-OCT as well as in SS-OCT, the signal which is acquired over the A-scan time  $\Delta T$ , and usually referred to as fringe signal, oscillates with a frequency that is proportional to the path length difference  $2\Delta z$ , exhibiting an amplitude that is proportional to  $\sqrt{R_S}$ , assuming a single reflection. Thus, Fourier transformation is the appropriate means to determine  $R_S(\Delta z)$  in case of multiple reflections, since it decomposes the fringe signal in its different frequency components, each representing light reflected from a certain depth in the sample. If one assumes that the spectral components can perfectly be resolved by the FD-OCT system and under consideration of equation 10 or equation 20, the resulting Fourier transformed signal for a single reflection can be written as follows [8]:

$$i_D(z) = \frac{\rho}{8}\gamma(z)(R_R + R_S) + \frac{\rho}{4}\sqrt{R_R}\sqrt{R_S}(\gamma[z + \Delta z] + \gamma[z - \Delta z]) \quad (22)$$

Here,  $\gamma(\mathbf{z})$  is the coherence function which is the Fourier transformation of the spectral power density  $\tilde{\mathbf{P}}(\mathbf{k})$ . It is important to know that Fourier transformation decomposes the fringe signal with regard to time delay or path length difference between the interferometer arms which is twice the optical distance in the sample ( $2\Delta z$ ).

Obviously, the coherence function appears three times in the Fourier transform. It is centered at  $\mathbf{z} = \mathbf{0}$ , representing the DC components (non-interferometric terms), at  $\mathbf{z} = -\Delta\mathbf{z}$  and at  $\mathbf{z} = \Delta\mathbf{z}$  representing the reflection at  $\Delta\mathbf{z}$ , where the maximum of the coherence function is proportional to  $\sqrt{R_S}$ .

The fact that  $i_D(\mathbf{z})$  is always symmetric with regard to  $\mathbf{z} = \mathbf{0}$ , meaning that the complete information about backscattered intensity is contained twice in the Fourier transform, is called the complex conjugate artifact in FD-OCT. This is a direct consequence of the fact that the detected fringe signal is real and the Fourier transformation therefore must be Hermitian symmetric. Light reflected from the opposite side of the zero delay point in the sample appears as a mirror image.

### 2.3.3. Comparison of different implementation techniques

Today, almost all research in optical coherence tomography focuses on FD-OCT. The reasons for this are the superior imaging speed and higher sensitivity, two main advantages of FD-OCT compared to TD-OCT.

Since in TD-OCT, the A-scan time is dependent on the mechanical movement of the reference mirror, A-scan rate and therefore imaging rate is typically limited to a few kHz. In FD-OCT, the A-scan rate is defined by the read-out rate of the CCD camera (SD-OCT) or by the sweep rate of the wavelength-swept light source (SS-OCT). However, in both cases, typical A-scan rates and imaging speeds exceed those of TD-OCT by a factor of 100 or more [15]. Imaging speed is of great importance for OCT, since it provides many advantages, such as, the possibility of three dimensional visualization or acquiring large densely sampled volumetric datasets in a short time. In retinal OCT, for example, the patient's eye motion and blinking make imaging more difficult. Furthermore, high imaging speed enables effective use of averaging and filtering.

The other main advantage of FD-OCT, in comparison to TD-OCT, is an inherent sensitivity advantage of  $\approx(20-30)$  dB [14] assuming the same power incident on the sample and the same A-scan rate. As a direct consequence, FD-OCT can detect considerably smaller signals which are backscattered from the sample improving image quality. However, there are also some disadvantages of FD-OCT compared to TD-OCT. One example is the sensitivity roll-off with increasing imaging depth, which appears only in FD-OCT. Furthermore, numerical resampling is not necessary. Another advantage of TD-OCT is the possibility to dynamically shift the focus in the sample within the imaging range without changing the path length of the sample arm [16]. In this way, it is possible to achieve a situation where the zero delay point (center of coherence gate) and the focus position in the sample are always identical. Therefore, the transversal resolution is almost the same over the whole imaging range and focusing with a higher numerical aperture NA becomes feasible, improving transversal resolution. In OCT without dynamic focus adjustment, this is not possible, since higher NA-focusing results in a decrease in depth of field, reducing the available depth range [16]. This technique is not applicable for FD-OCT, since here the information about backscattered intensity from each single depth in the sample is encoded in the entire A-scan signal.

Comparing SD-OCT with SS-OCT, in terms of imaging speed or sensitivity roll-off, requires a closer look at the current availability of fast spectrometers or fast wavelength swept light sources in the desired wavelength range. However, it is generally true to say that, currently, the fastest high-quality OCT imaging can be realized with SS-OCT and that

SS-OCT can show a considerably less pronounced sensitivity roll-off than SD-OCT. One has to recognize that both FD-OCT techniques have the same sensitivity advantage compared to TD-OCT; however, the lack of dual balancing capability in SD-OCT can be a disadvantage. Also worth mentioning is an effect called fringe washout which occurs in FD-OCT due to unwanted axial motion of the sample during image acquisition degrading sensitivity [17]. The reason why it happens is a decrease of the amplitude of the fringe signal due to the averaging of the signal over the integration time in each spectral channel of the detector. In SD-OCT, averaging in all spectral channels (CCD-pixels) happens simultaneously with an integration time of approximately the A-scan time  $\mathbf{T}$ , whereas, in SS-OCT, it happens sequentially ( $\mathbf{M}$  samples in A-scan time  $\mathbf{T}$ ) and the integration time therefore is  $\approx \mathbf{T}/\mathbf{M}$ . Consequently, in comparison to SD-OCT, SS-OCT systems exhibit fringe washout effects which are negligibly small or play a comparable role only for  $\approx \mathbf{M}$  times faster axial movement [18]. Generally, fringe washout effects decrease with increasing imaging speed (shorter A-scan time). Note that in SS-OCT, axial motion of the sample gives rise to other effects, like spatial image distortion caused by Doppler shift or blurring of images caused by degradation of axial resolution [17], which, in the case of very low A-scan rates, can also significantly deteriorate image quality.

## 2.4. - Optical Parameters

In this section and the ones that follow, several important characteristic parameters for OCT imaging are defined and corresponding measurements determining these parameters are introduced. Since within the research work presented in this thesis all OCT imaging was based on the swept source approach, the following analysis is restricted to SS-OCT. However, the principle can be easily transferred to other OCT techniques.

### 2.4.1. Point spread function

The point spread function (PSF) is defined as the impulse response of a focused optical system. In OCT, this is the signal that is obtained if a mirror is placed in the sample arm representing a single reflection from a certain depth in the sample with  $\mathbf{R}_S(\Delta\mathbf{z}) = \mathbf{1}$ . Consequently, measuring the PSF is the procedure of choice for determining the axial

resolution in an OCT system. Assuming perfect resampling and neglecting the sensitivity roll-off, the PSF in FD-OCT is given by the last term in equation 22, picking only the contribution from one side of the Fourier transform due to complex conjugate artifact. The peak of the PSF is centered at  $\mathbf{z} = \Delta\mathbf{z}$  and the shape is only defined by the coherence function  $\gamma(\mathbf{z})$  (equation 15).

## 2.4.2. Axial resolution

If one assumes a spectral power density  $\tilde{\mathbf{P}}(\mathbf{k})$  exhibiting a Gaussian shape, where  $\Delta\mathbf{k}_{\text{FWHM}}$  is the spectral FWHM,  $\mathbf{k}_0$  is the center wavenumber and  $\mathbf{P}$  is an arbitrary power,  $\tilde{\mathbf{P}}(\mathbf{k})$  can be written as follows [8]:

$$\tilde{\mathbf{P}}(\mathbf{k}) = \frac{\mathbf{P}}{\Delta\mathbf{k}_{\text{FWHM}}} \frac{2\sqrt{\ln 2}}{\sqrt{\pi}} e^{-\frac{4 \ln(2)(\mathbf{k}-\mathbf{k}_0)^2}{(\Delta\mathbf{k}_{\text{FWHM}})^2}} \quad (23)$$

In SS-OCT,  $\tilde{\mathbf{P}}(\mathbf{k})$  is equal to the time-dependent power spectral density  $\tilde{\mathbf{P}}(\mathbf{t}) = \tilde{\mathbf{P}}(\mathbf{k}(\mathbf{t}))$ . Fourier transformation then yields the coherence function [8]:

$$\gamma(\mathbf{z}) = \mathbf{P} \cdot e^{-z^2 \frac{(\Delta\mathbf{k}_{\text{FWHM}})^2}{4 \ln 2}} \quad (24)$$

The axial resolution  $\Delta\mathbf{z}_{\text{FWHM}}$ , defined as the FWHM of  $\gamma(\mathbf{z})$ , can be determined to [8]:

$$\Delta\mathbf{z}_{\text{FWHM}} = \frac{4 \ln(2)}{\Delta\mathbf{k}_{\text{FWHM}}} = \frac{2 \ln(2)}{\pi} \cdot \frac{\lambda_0^2}{\Delta\lambda_{\text{FWHM}}} \quad (25)$$

Here,  $\lambda_0$  is the center wavelength and  $\Delta\lambda_{\text{FWHM}}$  is the FWHM of the spectral power density in terms of wavelength. As expected, the axial resolution is indirectly proportional to the spectral sweep range of the wavelength swept light source and it increases with the center wavelength (Fig. 11).

Based on the same assumptions and because of the round trip propagation of the sample and the reference beam, we can define the coherence length  $l_c$  (coherence length means the length within which two beams are correlated) as a double of the axial resolution [8]:

$$l_c = \frac{4 \ln(2)}{\pi} \cdot \frac{\lambda_0^2}{\Delta\lambda_{\text{FWHM}}} \quad (26)$$

Thereby, it is important to know that the derivation of the last equation is based on the assumption that the refractive index  $\mathbf{n} = \mathbf{1}$ , defining the resolution in air. Therefore, the effective axial resolution in biological tissue is smaller since its index of refraction is greater [45].

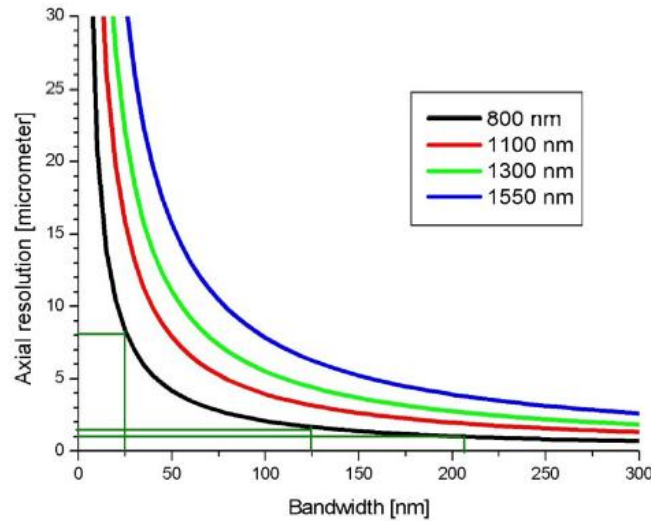


**Fig. 11** – Axial resolution as a function of the center wavelength and the bandwidth of the light source in air. [From Optics and Plasma Research Department, Risø National Laboratory, Denmark].

### 2.4.3. Lateral resolution

The lateral (or transversal) resolution in OCT is mainly dependent on its ability to focus the incident sample beam. Using Gaussian beam optics, the lateral resolution  $\Delta x$  in the focus, defined as twice the beam waist (Fig. 12), is given by (approximation of small angles) [9]:

$$\Delta x = \frac{4\lambda_0 f}{\pi D} = \frac{2\lambda_0}{\pi \cdot NA} \text{ where } NA = \frac{D}{2f} \tag{27}$$

Here,  $D$  is the spot size of the beam incident on the objective lens,  $f$  is the corresponding focal length and  $NA$  is the numerical aperture.

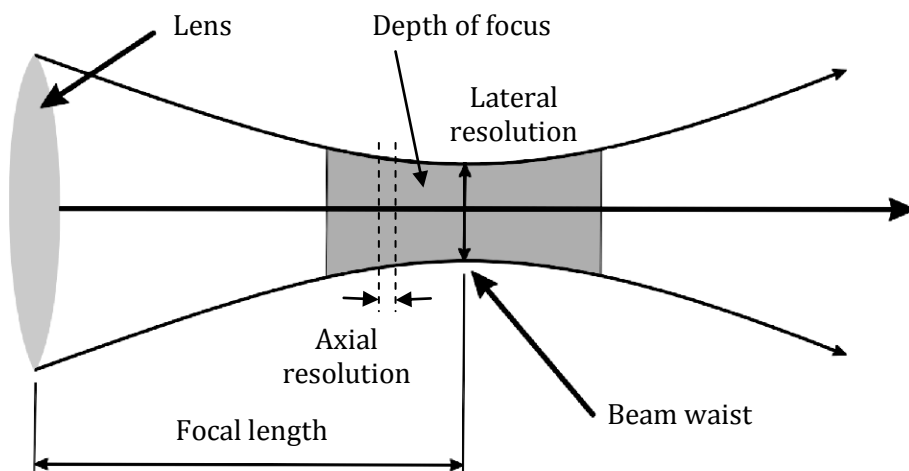


**Fig. 12** - Schematic of generic OCT sample arm optics

On the one hand, high **NA** focusing minimizes  $\Delta\mathbf{x}$ ; on the other hand, it restricts the usable depth range. Low **NA** focusing yields an emphasized degradation of lateral resolution with increasing distance to the focus (Fig. 13 and Fig. 14).

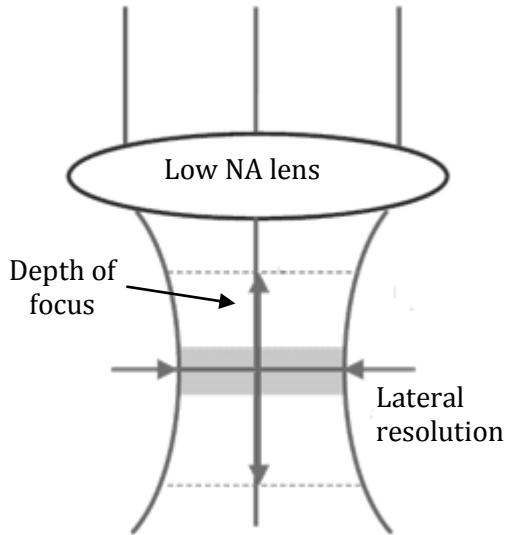


**Fig. 13** - Low NA focusing maximizes lateral resolution and increases depth range.

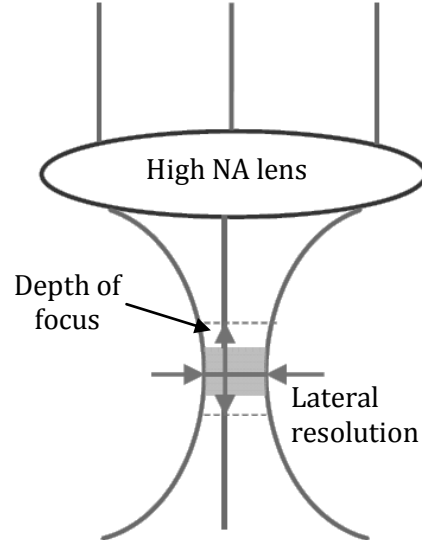


**Fig. 14** - High NA focusing minimizes lateral resolution and decreases depth range.

This can be expressed by the depth of focus  $\Delta z_f$ , which is the depth range where the focused spot diameter remains below an arbitrary limit [9].

$$\Delta z_f = \frac{\pi \Delta x^2}{2\lambda_0} = \frac{2\lambda_0}{NA^2} \quad (28)$$

Since the aim of OCT is to image over the maximum possible depth range, typically low **NA** focusing is used, tolerating a larger  $\Delta\mathbf{x}$  but ensuring an almost constant lateral resolution over the desired depth range. So, typically, the depth of focus considerably exceeds the axial resolution ( $\Delta z_f \gg \Delta z_{FWHM}$ ).

#### 2.4.4. Sensitivity

The sensitivity is a measure of the minimum detectable reflectivity  $R_{s,min}$  that enables detection of backscattered light. In the case of OCT system, it can also be defined as the ratio of incident power  $P_S$  on the sample to the minimum detectable power  $P_{min}$  that is backscattered from a certain depth, corresponding to a path length difference  $2\Delta z$ , or as the ratio of peak detector current signal in the Fourier transform  $i_D(\Delta z)$  to the corresponding value of the minimum detectable power  $i_{D,min}(\Delta z)$ .

Sensitivity  $S$  is given by a logarithmic representation:

$$S_{\text{dB}} = 10 \cdot \log\left(\frac{P_S}{P_{\text{min}}}\right) = 20 \cdot \log\left(\frac{i_D(\Delta z)}{i_{D,\text{min}}(\Delta z)}\right) = 10 \cdot \log\left(\frac{1}{R_{S,\text{min}}}\right) \quad (29)$$

Note that the additional factor of two stems from the fact that:  $i_D(\Delta z) \sim \sqrt{P_S} \sim \sqrt{R_S}$ .

One straightforward approach to measure sensitivity is to use a mirror in the sample arm ( $R_S = 1$ ), in order to determine the PSF and attenuate the light in the sample until the signal in the Fourier transform cannot be detected anymore. However, the transition between the condition that a signal can be detected and that it vanishes in the noise background is smooth. Therefore, a definition has been introduced, most commonly accepted in the OCT community, stating that this transition occurs when the signal to noise ratio  $\text{SNR} = 1$  [7]. The SNR is defined in terms of electrical power and reads as follows:

$$\text{SNR} = \frac{\langle i_D^2(\Delta z) \rangle}{\sigma^2(\Delta z)} \quad (30)$$

Here,  $\langle i_D^2(\Delta z) \rangle$  is the mean-square peak signal power and  $\sigma^2(\Delta z)$  is the variance of the noise background in a small window centered at  $\mathbf{z} = \Delta \mathbf{z}$ . With  $\text{SNR} = 1$ , the minimum peak detector current signal  $i_{D,\text{min}}(\Delta z)$  reads:

$$i_{D,\text{min}}(\Delta z) = \sqrt{\sigma^2(\Delta z)} = \sigma(\Delta z) \quad (31)$$

A typical measurement of sensitivity at  $\mathbf{z} = \Delta \mathbf{z}$  is performed as follows (applying equation 29): firstly, a mirror is placed in the sample arm yielding a path length difference  $2\Delta z$  and the peak value of the PSF,  $i_D(\Delta z)$  is determined; secondly, the sample arm is blocked and the standard deviation  $\sigma(\Delta z)$  of the noise floor in the Fourier transform in a window centered at  $\mathbf{z} = \Delta \mathbf{z}$  is calculated.

Blocking the sample arm and performing both measurements separately is essential, since an additional signal increases the noise floor over the whole  $z$ -domain.

Since power reflectivities  $R_S$  from interesting layers in biological tissue may be very small and due to the limitation of optical power on the sample, sensitivity is a very important parameter for OCT imaging. Depending on the OCT application, sensitivities of at least 90 dB or, in many cases, even higher than 100 dB are required to ensure high OCT image quality [14].

An intrinsic characteristic of FD-OCT is the depth dependent sensitivity roll-off, which, in SS-OCT, is due to the finite instantaneous linewidth  $\delta k$  of the wavelength swept light source. Typically, the experimental determination of this effect is simply carried out



by measuring the **PSF** corresponding to different imaging depths  $\Delta z$  (Fig. 15(a)). This is accomplished by recording the fringe signal for different reference mirror positions. The same numerical resampling is applied to all fringe signal traces and the resulting Fourier transformed signals  $i_D(\mathbf{z})$  are plotted representing a typical sensitivity roll-off measurement. The sensitivity drop over imaging depth can then directly be derived from the decay of the peaks of the PSFs.

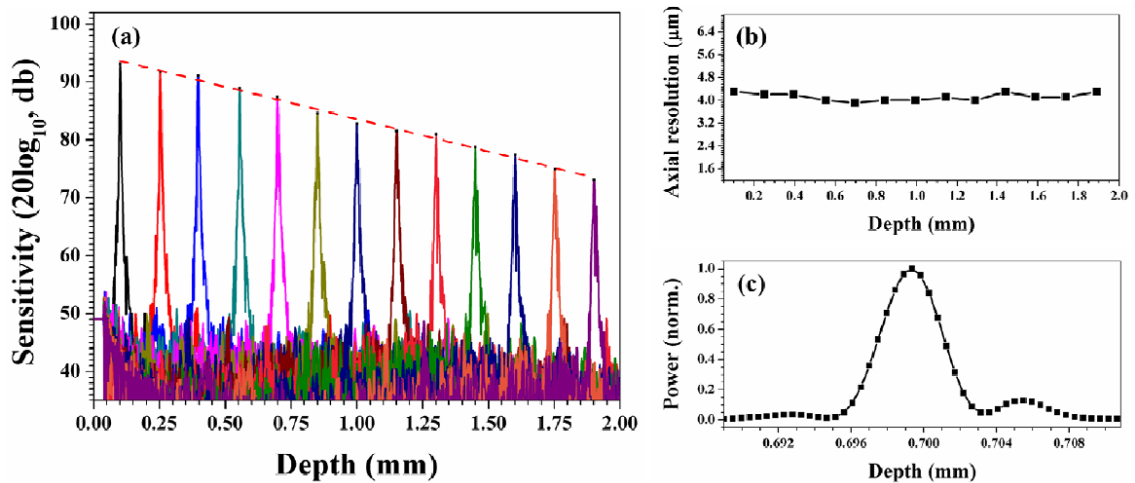


**Fig. 15** - Performance of FD/SS-OCT. (a) Sensitivity as a function of depth: R-number values of sensitivity roll-off were found to be 11.1 dB/mm; (b) axial resolution as a function of the depth; (c) point-spread function of the axial resolution near 0.7-mm depth [21].

The sensitivity roll-off is often specified in different ways in literature. A common way is to name the 6 dB roll-off point which corresponds to half the  $i_D(\mathbf{z})$  [19]. Other descriptions, considering a larger imaging range, define the R-number (a measure for coherence) which is given by the slope of a linear fit to the peak maxima of the PSFs (logarithmic representation). It was first defined by Benjamin *et al.* in 2009 [20] with the objective of deriving a single number to characterize the roll-off properties of wavelength swept lasers.

### 2.4.5. Dynamic range

The dynamic range in an OCT system is defined as the ratio of maximum to minimum reflected power that can be detected simultaneously. The measurement of dynamic range is performed similarly to a sensitivity measurement. A mirror is placed in the sample arm ( $R_S = 1$ ) and the **PSF** is determined corresponding to a certain path length difference ( $2\Delta z$ ) in the interferometer arms. The maximum detected signal then

corresponds to the peak value of the **PSF**,  $i_D(\Delta z)$ . The minimum detectable signal is equal to the standard deviation of the noise floor:  $i_{D,\min}(\Delta z) = \sigma(\Delta z)$ . However, the main difference to the determination of sensitivity is the fact that, here, both measurements have to be done simultaneously and not separately. The standard deviation of the noise floor is typically determined in a window close to the peak at  $z = \Delta z$ , where the coherence function  $\gamma(z)$  is negligibly small. Therefore, the dynamic range in logarithmic representation  $D_{dB}$  reads as follows:

$$D_{dB} = 10 \cdot \log\left(\frac{P_{\max}}{P_{\min}}\right) = 20 \cdot \log\left(\frac{i_D(\Delta z)}{\sigma(\Delta z)}\right) \quad (32)$$

In OCT, the dynamic range is typically several orders of magnitude smaller than the sensitivity. OCT imaging quality and imaging range can be affected if the dynamic range is not sufficiently high to enable simultaneous detection of the weakest and the strongest reflections from biological tissue.

#### 2.4.6. Noise contributions

An important noise contribution in optical detection is shot noise, which is exclusively due to the discreteness of the photons (quantum nature of light) and therefore it is a noise contribution that exists inherently. In other words, shot noise sets a lower limit to the total noise in a system. This is why calculating the shot noise allows the determination of the maximum possible sensitivity.

Assuming that the mean number of photons that hit the detector during a certain time interval equals  $\bar{N}_{ph}$ , the probability of incident photons on the detector during this same time interval can be determined following a Poisson distribution, where the variance in photon number is given by  $\sigma_{ph}^2 = \bar{N}_{ph}$ . Assuming a photodetector with quantum efficiency  $\eta$  and considering the uncertainty in the number of photo generated electrons, binomial distribution with a variance  $\eta(1 - \eta)\bar{N}_{ph}$ , the resulting variance of the generated electrons is determined to [29]:

$$\sigma_e^2 = \eta(1 - \eta)\bar{N}_{ph} + \eta^2\bar{N}_{ph} = \eta\bar{N}_{ph} \quad (33)$$

In order to specify the variance of the detector current  $\sigma^2$ , this result can be transformed using the mean detector current  $\bar{I}$  [29]:

$$\bar{I} = \rho\bar{P} = \frac{\rho\bar{N}_{ph}\hbar\omega}{T_i} = \frac{\eta e\bar{N}_{ph}}{T_i} \quad (34)$$

where the detector responsivity is  $\rho$  [29]:

$$\rho = \frac{\eta e}{\hbar\omega} \quad (35)$$

the detector integration time is  $T_i$ :

$$T_i = \frac{1}{2B_W} \quad (36)$$

the mean optical power is  $\bar{P}$ , the photon energy is  $\hbar\omega$ , the elementary charge is  $e$  and  $B_W$  is the electronic bandwidth of the detector. The shot noise detector current variance  $\sigma_{sh}^2$  then reads [22]:

$$\sigma_{sh}^2 = 2e\bar{I}B = 2\rho e\bar{P}B_W \quad (37)$$

In an OCT system, there are other noise contributions which can either impede or make shot noise limited operation impossible. Besides shot noise, there are two other main types of noise [22], which cause fluctuations of the detector current and will be defined in terms of detector current variances. On the one hand, there is receiver noise which is independent from the incident light. Receiver noise contains dark noise  $\sigma_{dk}^2$  (dark current in the photo receiver) and thermal noise  $\sigma_{th}^2$  (also referred to as Johnson noise or Nyquist noise) [22], which is due to thermal motion of charge carriers in the equivalent resistance  $R$  of the photo receiver circuit. The thermal noise can be specified to [23]:

$$\sigma_{th}^2 = \frac{4k_B T B_W}{R} \quad (38)$$

with temperature  $T$  (Kelvin), Boltzmann constant  $k_B$  and electronic bandwidth  $B_W$ .

On the other hand, there is photon excess noise  $\sigma_{ex}^2$ . The name already indicates that this is a noise contribution originated by light intensity fluctuations which occur in addition to shot noise. A light source with nonzero excess noise generates photons that do not obey Poissonian statistics. The arrival of photons at the detector is not uncorrelated [22]. The variance of the photon number of the underlying photon counting statistics exceeds the shot noise limited case  $\sigma_{ph}^2 = \bar{N}_{ph}$  and can be written as follows [29]:

$$\sigma_{ph}^2 = \bar{N}_{ph} + \alpha \bar{N}_{ph}^2 \quad (39)$$

( $\alpha > 0$ , super-Poissonian photon counting statistics). Note that the last term is referred to the photon excess noise, which is proportional to  $\bar{N}_{ph}^2$ . Assuming fully polarized broadband thermal light with a Gaussian intensity distribution (following Bose-Einstein statistics,  $\alpha =$

1), the variance of the detector current resulting from excess photon noise can be determined to [22]:

$$\sigma_{\text{ex}}^2 = \frac{\bar{I}^2 \cdot B_W}{\Delta\nu} = \frac{\rho^2 \bar{P}^2 B_W}{\Delta\nu} \quad (40)$$

where  $\bar{P}$  is the mean power,  $B_W$  is the electronic bandwidth of the detector and  $\Delta\nu$  is the spectral bandwidth of the source. Generally it can be assumed that the variance of the excess photon noise current is proportional to the square mean power  $\sigma_{\text{ex}}^2 \sim \bar{P}^2$ .

Furthermore, another noise contribution, that has been neglected so far but which can have a significant contribution in case of using dual balancing, is beat noise  $\sigma_{\text{be}}^2$  [22]. Beat noise arises if one takes into account parasitic light that is reflected from the sample arm, due to for example spurious reflections from the sample arm optics, with a power reflectivity  $R_X$ . Typically  $R_X > R_S$ , and the photon excess noise is proportional to  $\sigma_{\text{ex}}^2 \sim (R_X + R_S)^2$ , where the beat noise  $\sigma_{\text{be}}^2 \sim 2R_X R_S$  is the part of the result which does not cancel out due to a phase difference of  $\pi$  even if one assumes perfect dual balancing.

Quantization noise of analog to digital converter and noise at typical A-scan rates can normally be neglected in OCT [15].

#### 2.4.7. SNR - Signal-to-noise ratio

In the following paragraphs, an SS-OCT setup is considered exhibiting  $M$  spectral channels with wavenumber  $k_m$ , corresponding to  $M$  samples. Sensitivity roll-off with increasing depth is not considered here. Furthermore, for the sake of simplicity, a rectangular shaped spectrum is assumed, so that each spectral channel comprises the same optical power. If one rewrites equation 10, substituting  $P(k)$  by  $P(k_m)$ , which is defined as the incident power on the sample corresponding to each channel:

$$P(k_m) = \frac{P(k)}{2} \quad (41)$$

the interferometric term reads:

$$I_D(k_m) = \rho P(k_m) \sqrt{R_R R_S} \cos(2k_m \Delta z) \quad (42)$$

It can be shown in [8] that discrete Fourier transformation of this fringe signal, representing a single reflection, yields a peak signal of the **PSF** of:

$$i_D(\Delta z) = \frac{M}{2} \rho P(k_m) \sqrt{R_R R_S} \quad (43)$$

which is a factor  $M/2$  larger than the signal amplitude of  $I_D(\mathbf{k}_m)$ . The interpretation of this fact is that the cosinusoidal interference pattern corresponding to each spectral channel adds coherently in the discrete Fourier transformation resulting in an enhancement factor of  $M$  in the peak signal. The mean-square peak signal power at  $\mathbf{z} = \Delta\mathbf{z}$  therefore reads [8]:

$$\langle i_D^2(\mathbf{z}) \rangle = \frac{M^2}{4} \rho^2 P^2(k_m) R_R R_S \quad (44)$$

Assuming that the power of the light reflected from the sample arm is neglected  $R_S \ll R_R$ , the detector signal of each channel includes an additive uncorrelated white noise term with a mean value of zero and a variance  $\sigma^2$  where the shot noise is the only noise present. The variance of noise over the signal of each channel at  $\mathbf{z} = \Delta\mathbf{z}$  is equal to [22]:

$$\sigma_{sh}^2 = \rho e P(k_m) R_R \cdot B_W \quad (45)$$

Since noise in each spectral channel is uncorrelated, noise variances add incoherencies in Fourier transformation. So, the shot noise variance in z-domain can be determined to [8]:

$$\sigma_{sh}^2 = \sum_{m=1}^M \sigma_{sh}^2(k_m) = M \rho e P(k_m) R_R \cdot B_W \quad (46)$$

Therefore, the signal to noise ratio of the systems can be written [8][41]:

$$\text{SNR} = \frac{\langle i_D^2(\Delta\mathbf{z}) \rangle}{\sigma^2(\Delta\mathbf{z})} = \frac{\langle i_D^2(\Delta\mathbf{z}) \rangle}{\sigma_{ph}^2(\Delta\mathbf{z})} = M \frac{\rho P(k_m) R_S}{4eB} \quad (47)$$

Whereas the shot noise is the only noise present and  $\mathbf{z} = \Delta\mathbf{z}$ . Furthermore, this derivation is based on a rectangular spectrum, assuming the same optical power in each channel.

Next, the goal is to derive an expression to all previously mentioned noise contributions. Therefore, one needs to be aware of the fact that the mean square peak signal power in OCT is proportional to  $R_S \times R_R$ . Again, it is assumed that  $R_S \ll R_R$ . Thus, the sample arm light is neglected in terms of noise. Due to uncorrelated noise contributions, the previously derived detector current variances for the different types of noise can be added and, assuming proportionality factors  $\mathbf{a}$ ,  $\mathbf{b}$  and  $\mathbf{c}$ , the noise contributions can be written as follows:

$$\text{SNR} \approx \frac{R_S R_R}{\sigma_{dk}^2 + \sigma_{th}^2 + \sigma_{sh}^2 + \sigma_{ex}^2 + \sigma_{be}^2} = \frac{R_S R_R}{\sigma_{dk}^2 + \sigma_{te}^2 + aR_R + bR_R^2 + cR_R} \quad (48)$$

For a better understanding of OCT performance, it is instructive to show how the signal to noise ratio would look like, assuming that each noise contribution occurs individually (neglecting the other contributions). Moreover, it is interesting to see in how

much these different SNR values depend on the reflected optical on the reference arm power (optical power of light returning from the reference arm) or simply the power reflectivity  $R_R$ . This is a parameter that is freely adjustable.

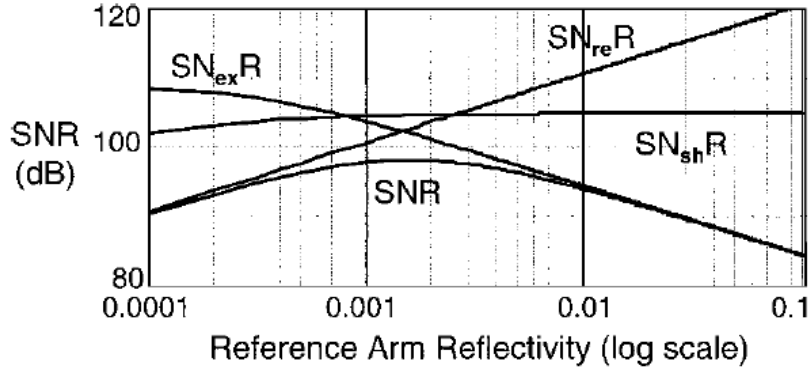


**Fig. 16** - SNR as a function of reference-arm reflectivity (SNR). Also shown are the signal-to-receiver-noise ratio  $SN_{reR}$ , the signal-to-shot-noise ratio  $SN_{shR}$  and the signal-to-excess-noise ratio  $SN_{exR}$ . The calculations assume that  $R_s = 1$ ,  $R_x = 0.0005$ ,  $\rho = 0.95$  A/W, the receiver noise current is  $2 \text{ pA}/\sqrt{\text{Hz}}$ , an unpolarized optical source provides 20 mW of power at 1300 nm with 50-nm linewidth, and  $B = 1$  MHz [22].

Through the analysis of Fig. 16 and taking into account that the receiver noise (dark current and thermal noise), exclusively, is independent of the light incident on the detector, the corresponding signal to noise ratio is proportional to  $R_R$ . Regarding solely shot noise (proportional to  $R_R$ ), the corresponding signal to noise ratio becomes independent of  $R_R$ . If one takes into account only photon excess noise (proportional to  $R_R^2$ ), the according signal to noise ratio is inversely proportional to  $R_R$ .

The previous findings clearly indicate that the choice of  $R_R$  determines the best possible sensitivity for OCT imaging. Typically, the light in the reference arm has to be considerably attenuated. If the reflected optical on the reference arm power is too high, excess noise usually dominates, which reduces the overall SNR. On the other hand, if the reflected optical reference arm power is too low, the dark noise and thermal noise typically dominate, also worsening the overall SNR.

Note that the application of high-speed photo receivers (high electronic bandwidth) with sufficiently high amplification, which are required for high speed SS-OCT, often results in a poorer receiver noise performance. Hence, in this case, raising the reflected optical reference arm power (larger  $R_R$ ) may become necessary.

It is also important to say that dual balanced operation can considerably reduce photon excess noise, simplifying the achievement of shot noise limited operation and allowing higher values of  $R_R$ , if necessary [24]. However, dual balancing is not perfect,

particularly due to imperfect power balancing over the whole spectral range [41]. Therefore, residual excess noise remains.

## 2.5. - OCT Progress and Applications in Medicine

OCT is fundamentally a new type of biomedical imaging technology which enables high-resolution, non-invasive, cross-sectional imaging of the internal micro-structures in biological tissue by measuring the intensity and the echo time of their optical reflections. It is a powerful image modality because it enables real-time and *in situ* imaging of tissue structure or pathologies with the possibility to generate three-dimensional data sets containing comprehensive, volumetric information. OCT is a comparably young imaging technique and was first demonstrated in 1991 [6].

OCT is used for various different applications in medicine and, in this case, it gives a major contribution to the development of ophthalmology, where this technology enables the imaging of the retina and the anterior eye at a resolution that was previously impossible to achieve with any other noninvasive imaging methods [9][25]. OCT plays a very important role in the diagnosis of diseases likes glaucoma, age-related macular degeneration or diabetic retinopathy [25].

For retinal imaging, OCT is the technique of choice since it provides high axial resolution which is of particular importance due to the stratified organization of the retina. This cannot be achieved using ultrasonography, which can be used for intraocular examinations but requires physical contact to the eye providing a rather poor axial resolution.

Scanning laser opthalmoscopy (SLO), first demonstrated in 1980 [30], where a focused laser spot is scanned on the retina measuring the integrated backscattered light, yields *en-face fundus* images providing high transversal resolution and good contrast. However, the axial resolution is restricted to typically 300  $\mu\text{m}$  due to pupil aperture and ocular aberrations [8]. Two years after the first demonstration of OCT, the first *in vivo* retinal imaging was realized in 1993 [31]. It was only two years later that the first commercial OCT device was launched by Carl Zeiss Meditec enabling retinal OCT imaging for clinical use.

Besides retinal imaging, OCT also provides another medical application in the human eye, namely imaging of the anterior segment including the cornea [32], where the

applied wavelength range is usually centered at 1300 nm. This allows higher optical powers on the sample and deeper penetration. Typical diagnostic applications are measurements of corneal thickness and corneal refractive power or identification of causes for corneal opacity.

In cardiology, OCT is able to traverse many of the limitations of angiography and intravascular ultrasound when imaging coronary stents *in vivo* and will continue to be a unique imaging modality that is able to help improve our understanding of the atherosclerotic process and shed light on all important interaction between coronary stents and the vessel wall [26]. The first demonstration of intravascular OCT *ex vivo*, was achieved in 1996 [33], already showing the potential of this technique: *OCT achieves high resolution, can image through highly calcified tissue, has high dynamic range, and can be adapted for catheter-based imaging. OCT is a promising new technology for intravascular imaging and the diagnosis of high-risk coronary lesions.* [33].

We can also mention its use in dermatology and dentistry. In the first case, OCT provides a quick and useful diagnostic imaging technique for a number of clinical questions (evaluation of skin lesions, especially non-melanoma skin cancers and inflammatory diseases, quantification of skin changes, visualization of parasitic infestations, and examination of other indications such as the investigation of nails) and it is a valuable addition or complement to other noninvasive imaging tools such as dermoscopy, high-frequency ultrasound, and confocal laser scan microscopy [9][27]. In the second case, dental OCT directly addresses the image quality issue with its intrinsic high resolution and contrast mechanism, which is useful to indentify tiny pre-caries and fissure lesions before their potential progression to serious dental decay. Furthermore, a flexible handheld fiber-guided probe allows aiming directly at regions of interest of patients' teeth with the advantage of high-speed dental imaging acquisition *in vivo*. It also removes the need to use radioactive source for clinical diagnostic [9][28].

Application in gastrointestinal, laryngology, and surgical guidance and intervention, are other areas in medicine where OCT is already in use [9].

A development in OCT technology is functional OCT. This technique provides additional information about the biological sample that is being investigated, which usually leads to a contrast enhancement. Three important types of functional OCT are Doppler-OCT, polarization sensitive OCT and spectroscopic OCT.

Due to the Doppler effect, the flow velocity component of moving material in the sample (such as blood in vessels) that is parallel to the incident light (axial velocity) can be determined (Fig. 17).



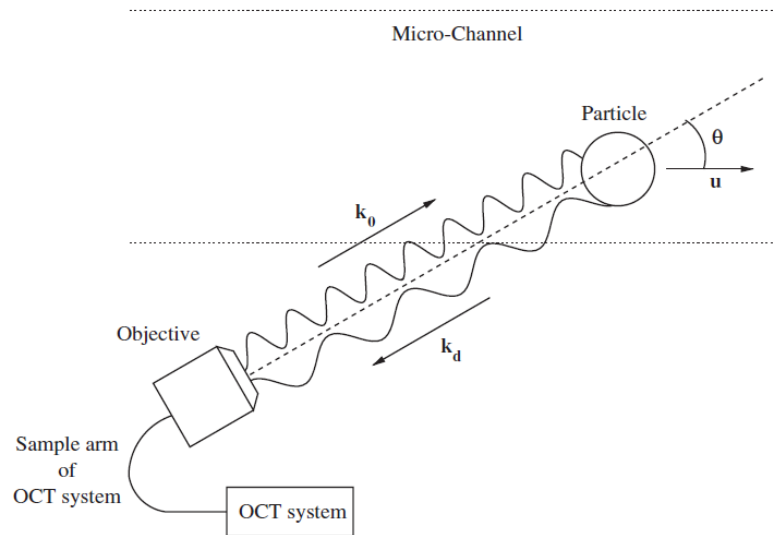


**Fig. 17** - Schematic for the operation of optical Doppler tomography. The basic OCT system is as described in the previous sections. The sample arm is held at some angle  $\theta$  to the direction of flow. Therefore, an optical signal with wave-vector  $k_0$  falls on a particle moving with velocity  $u$ . The light scattered back into the sample objective is Doppler shifted and has wave-vector  $k_d$  [42].

The first *in vivo* Doppler OCT images have been demonstrated in 1997 [34]. These first time domain Doppler OCT systems were based on the spectrogram method, where the fringe signal of each A-scan is analyzed via for example a short time Fourier transformation in order to determine the z-dependent fringe frequency and thus the depth dependent velocity. However, for faster imaging the velocity sensitivity is not sufficient. Therefore, another method, called phase-resolved Doppler OCT [18], has been investigated, which relies on measuring the phase change between adjacent A-scans [9]. This approach was first applied in [35]. Doppler OCT is mainly used to determine the blood flow as, for example, for drug screening or within the choroid or the retinal capillaries.

Polarization sensitive OCT enables to learn about polarization dependent properties of the examined sample tissue, such as birefringence, optical axis orientation or dichroism [42]. In 1992, the first OCT system capable of measuring changes in the polarization state of light was presented [36]. In a completely bulk-optic interferometer, the polarization states of light in the sample arm and the reference arm have to be prepared (typically circularly polarized on the sample) and after the interferometer both polarization components are separated and measured independently with two detectors (Fig. 18).

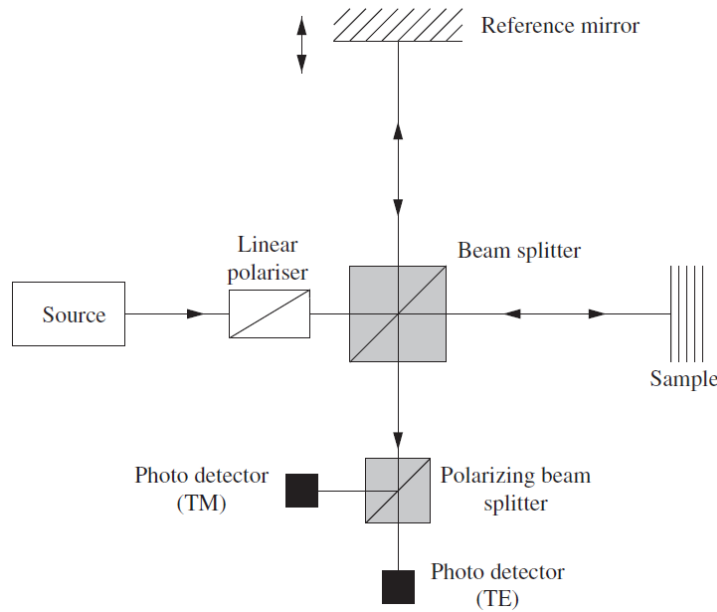


**Fig. 18** - Experimental arrangement for polarization sensitive OCT. The polarizing beam-splitter (PBS) splits the optical output signal into its transverse electric (TE) and transverse magnetic (TM) parts [42].

In this way, the entire set of Stokes parameters, fully describing the polarization state, can be derived [37]. Polarization sensitive OCT can be used, for example, to determine polarization properties in the retinal nerve fiber layer.

In spectroscopic OCT [38], spectroscopic analysis is combined with standard OCT which enables to identify depth resolved tissue absorption spectra. This is often used for contrast enhancement in OCT by spectral information. Another application is the measurement of localized oxygen saturation.

Besides the usual OCT implementations described so far, there have been various other approaches, two of which shall be mentioned next in a summarized way.

One implementation is the linear OCT [39], which principle is similar to TD-OCT but with no moving parts in the reference arm. Two expanded optical beams originated from the sample and the reference arm are tilted and superposed on a linear line array detector so that each pixel corresponds to a certain path length difference resulting in an interference pattern.

Another implementation is full field OCT [40], which does not require galvanometer mirrors for transversal scanning of the beam on the sample and it is based on homogeneous illumination of the whole field using microscope objectives and a typically, spatially and temporally incoherent light source, such as a halogen lamp . After the interferometer, light is detected using a CCD array (Fig. 19).

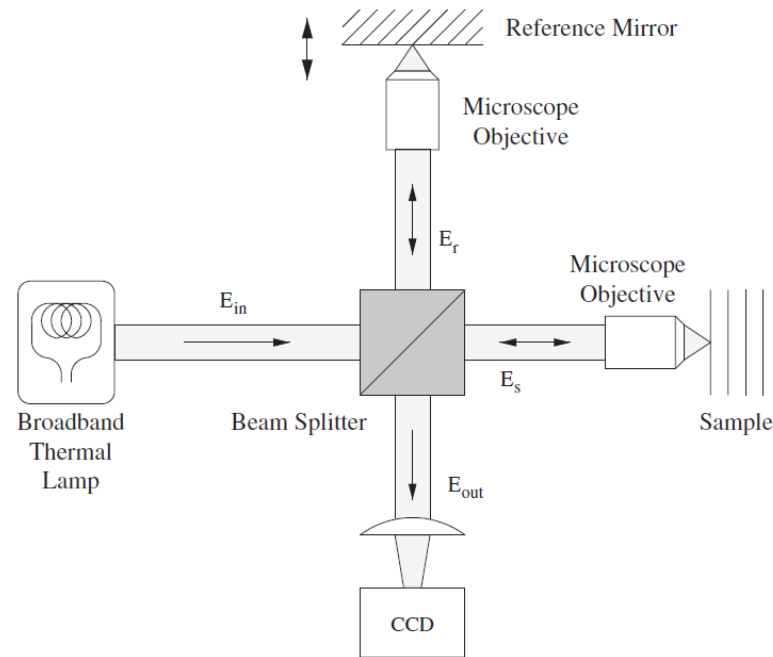


**Fig. 19** - Experimental set-up for thermal-light full field OCT. Instead of scanning the sample laterally, two-dimensional data are obtained simultaneously from each layer by the CCD. Time-domain reference mirror scanning acts as an axial probe [42].

Therefore, during one A-scan, the depth profile at all transversal points on the sample is detected simultaneously. Advantages are that there are no speed limitations due to the beam scanner and this technique can provide very good axial and transversal resolutions [40][42]. Disadvantages are a rather poor sensitivity, small field of view and considerable fringe washout and pixel cross-talk effects [40][42].

## 2.6. Comparing Other Biomedical Imaging Techniques

Today, there are several different imaging techniques used in medicine such as computer tomography (CT), magnetic resonance imaging (MRI) or positron emission tomography (PET). These techniques enable imaging of large volumes in the human body, but they are comparably expensive and require technically appropriate spaces, not allowing the realization of low-cost portable scanners.

In the following figure, the typical performance of the most common imaging technologies is presented with respect to the achievable resolution and the penetration depth into tissue.

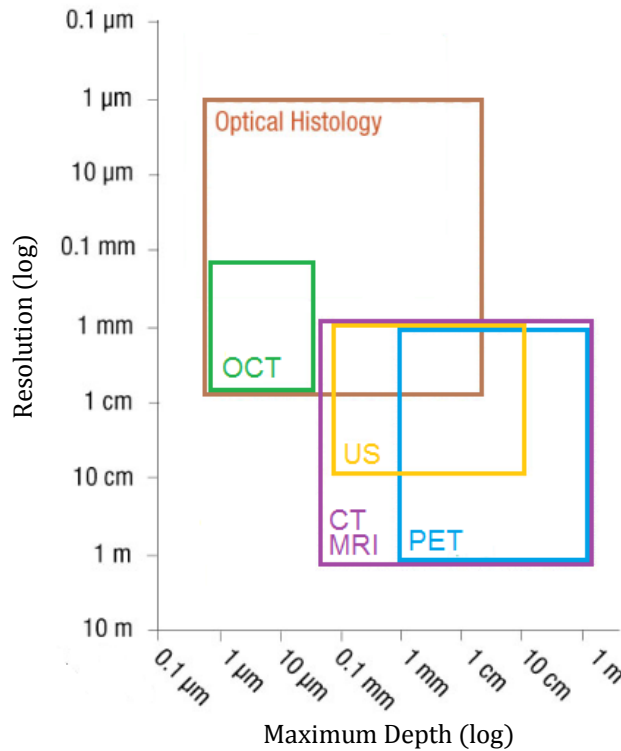


**Fig. 20** - Performance of most common medical imaging technologies with respect to image depth and achievable resolution. Adapted from [57].

CT and PET are both based on the use of ionizing radiation, which constrains the applicability for human imaging. Conventional clinical systems provide spatial resolutions from 0.5 mm to 1 mm (CT and MRI) and several mm (PET), which is insufficient for many medical applications. Alternatively, less complex approaches, which are based on non-ionizing radiation allowing longer exposure times and providing a better resolution, are medical ultrasonography (US) and optical techniques (such as confocal microscopy or OCT). Like ultrasound, the acquisition time of OCT is short enough to support tomographic imaging at video rates, making it much more tolerant to subject motion than either CT or MRI. OCT does not require physical contact with the sample, and it may be used in air-filled hollow organs (unlike ultrasonography).

In ultrasonography, there is a relationship between resolution and image penetration depending on the ultrasound frequency. High frequency approaches provide resolutions of  $\approx 15 \mu\text{m}$ , but image penetration is restricted to a few millimeters. The typical resolution of a standard clinical system is of a few  $\approx 100 \mu\text{m}$ , whereas penetration depth can achieve several centimeters [9].

In confocal microscopy, where transversal and axial resolutions are linked by beam diffraction, a resolution approaching  $\approx 1 \mu\text{m}$  has already been realized. However, the

disadvantage is the small penetration depth of a few  $\approx 100 \mu\text{m}$  caused by strong scattering of light in typical, biological tissue [7].

In OCT, transversal and axial resolutions are decoupled enabling low numerical aperture focusing which increases the depth of field. Here, the penetration depth is limited to  $\approx 2\text{-}3 \text{ mm}$  with typical resolutions of  $\approx 10 \mu\text{m}$  [26]. However, ultra-high resolution OCT has been demonstrated providing axial resolutions of  $\approx 2\text{-}3 \mu\text{m}$  [26]. In spite of the small penetration depth and the comparably small imaging volumes, OCT is preferred to ultrasound or CT in several medical applications due to its high resolution and fast image acquisition. By means of, for example, endoscopes or catheters, internal body imaging can be realized [9].



# Chapter 3

## Experimental Setup and Analysis

In this chapter, the focus is on the presentation and explanation of the SS-OCT setup that is applied for OCT imaging presented in this project.

The description of the main characteristics and the choices made in the selection of individual components are also worked here.

Furthermore, some important optical and electronic parameters related to the assembly used are also determined.

### 3.1 - Swept Source OCT Setup

The setup used in this project is sketched on the following figure (Fig. 21) and is based on a Michelson interferometer using fiber optic components.

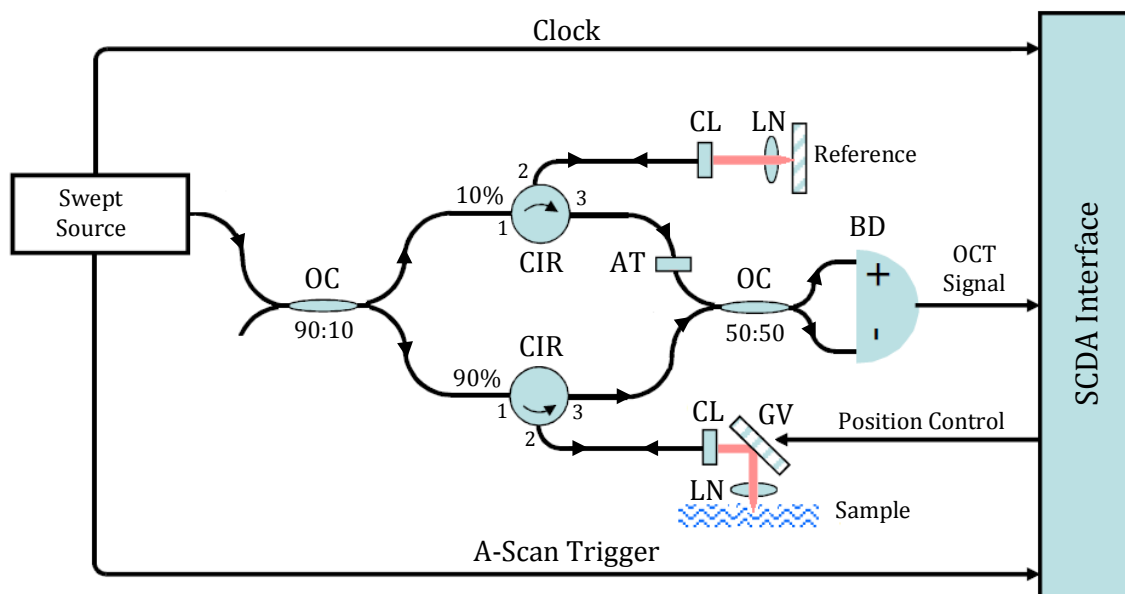


**Fig. 21** - Schematic of the swept-source OCT imaging system used. BD: Fixed gain balance detector; CIR: Single mode fiber optic circulator; CL: Fixed focus collimator; LN: Scan lens; SCDA – System control and data acquisition; GV: 2D Galvo system; AT: Variable fiber optical attenuator; OC: 2x2 Single mode fused fiber optic couplers. Adapted from [43].

Light from the swept source first passes on a 90:10 single mode fused fiber coupler to split the output power (90% of the output power into the sample arm and the remaining 10% into the reference arm). Thus the output power of the light source that comes from the reference arm (gold mirror), conversely to the one that comes from the sample, is attenuated by a variable fiber optical attenuator. This is done in order to ensure, as much as possible, power matching at both photodiodes of the balance detector and therefore to enable optimum dual balancing. Note that, in this point of the project it is not taken into account that the power going to the sample is limited on medical application.

The two single mode fiber optic circulators are used both in the reference and sample arms to redirect the back reflected light into a single mode fused 50:50 fiber couplers for interference.



In the reference arm, light is collimated (fixed focus collimation) and directed by the lens, reflected at a mirror with adjustable position (to enable fine-tuning on the optical path lengths and incidence angle), and coupled back into the circulator. Moving the mirror shifts the point of zero delay in the sample (Fig. 22).

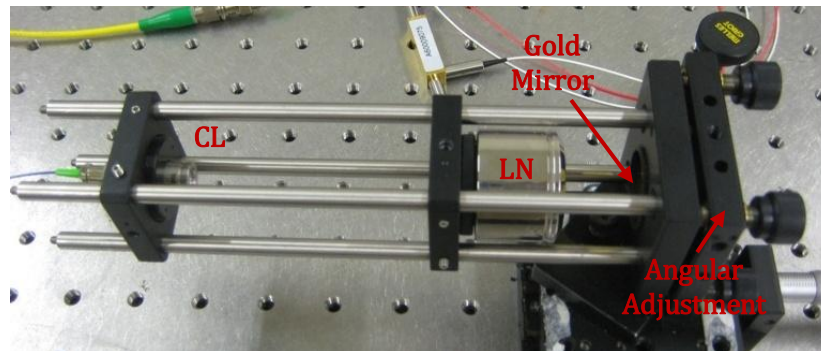


**Fig. 22** – Reference arm setup. CL: Fixed focus collimator; LN: Scan lens.

In the sample arm, light exiting the fiber core of the single mode fiber is collimated, passing two galvanometer silver mirror scanners (2D Galvo system), and it is focused by the lens and so a Rayleigh image of the sample is obtained (Fig. 23). The first fast scanner mirror moves the beam transversally on the sample (X-direction). For three-dimensional imaging, not yet implemented, another slow scanner is scanned in addition to the fast scanner, resulting in a perpendicular, independent movement of the beam on the sample (Y-direction). The slow scanner steps to its next position when the fast scanner completes a B-scan, enabling line-by-line scanning of the surface. Note that the 2D Galvo system was assembled both prior to the lens (pre-objective-scanning) and after the collimator (Fig. 23).

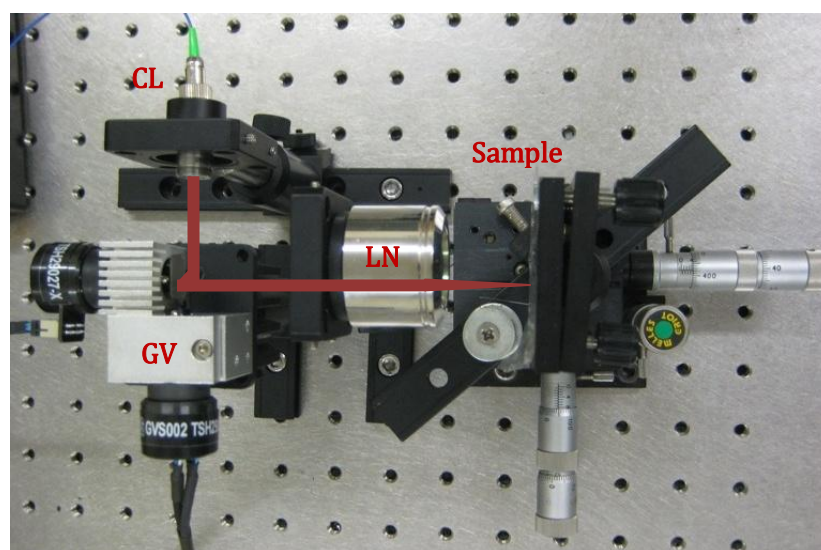


**Fig. 23** – Pre-objective scanning setup (CL: Fixed focus collimator; LN: Scan lens; GV: 2D Galvo system).

Fixed gain balance detector is achieved by detecting light from both outputs of the interferometer (single mode fused 50:50 fiber couplers) with a dual balanced photodetector, which consists of two photodiodes and a differential amplifier (where light from both interferometer arms superpose).

After the balanced receiver, the signal is digitized with a high speed digitizer board with an external clock rate coming from the swept source. The typically sawtooth-like shaped control signals for the 2D Galvo system drivers are software generated with a digital to analog output board. The numerical processing of the data and the generation of control signals for the galvos are synchronized using an A-scan trigger signal from the swept light source. In order to generate two-dimensional images in real-time, all the control is made on a personal computer with the software developed in this project.

The following figure (Fig. 24) is a photograph of the final bench system in the laboratory:

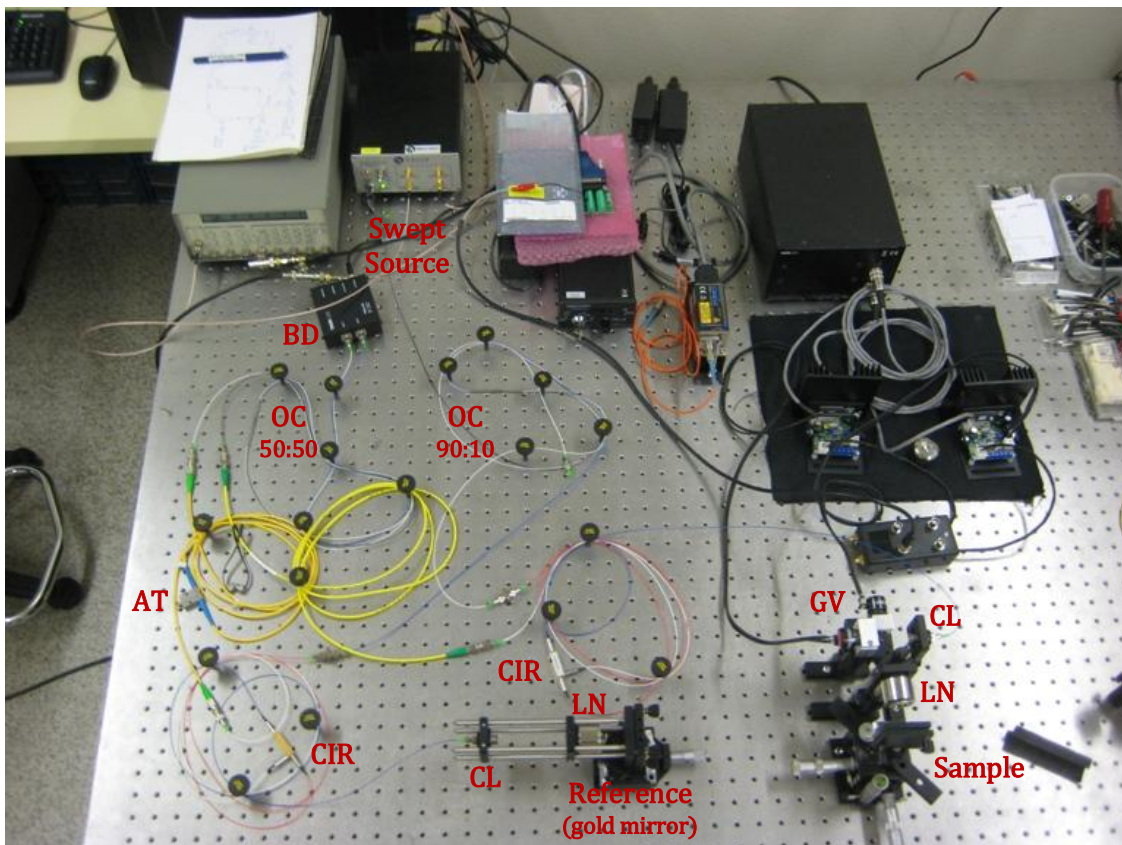


**Fig. 24** – Picture of the swept-source OCT imaging system used. BD: Fixed gain balance detector; CIR: Single mode fiber optic circulator; CL: Fixed focus collimator; LN: Scan lens; GV: 2D Galvo system; AT: Variable fiber optical attenuator; OC: 2x2 Single mode fused fiber optic couplers.

Note that with this setup, the optical path lengths in the reference and sample arms are matched and light passes components of the same type with almost identical spectral

characteristics, so it can ensure optimally matched power at both photodiodes over the whole sweep spectrum allowing better excess noise suppression.

## 3.2 - Swept Source

When choosing a certain wavelength range for OCT imaging, one important prerequisite is, of course, the availability of appropriate light sources and detection systems in that wavelength range. Moreover, the wavelength can have a considerable impact on image quality, contrast and on the achievable penetration depth in the biological tissue depending on the medical application.

### 3.2.1. Light wavelength ranges for OCT

Primarily, there are two main processes which are wavelength dependent and that influence OCT imaging: scattering and absorption of photons in the tissue. The eye behind the pupil is highly transparent for visible light, as well as near-infrared light [9]. If we model the eye as a volume of water, it absorbs near-infrared radiation starting at wavelengths of approximately 920 nm and continuing all along the infrared [9].

So, in the case of retinal OCT imaging, which is the most prominent application in OCT, the absorption in water plays an important role, since light traverses the eye twice, which corresponds approximately to  $2 \times 2.5$  cm of water [4]. If light passes 5 cm of water, absorption results in an attenuation of optical power of  $\approx 99.86\%$  at 1300 nm,  $\approx 52.30\%$  at 1060 nm and only  $\approx 10.64\%$  at  $\approx 800$  nm (Fig. 25). Therefore, in retinal measurements, a center wavelength of  $\approx 800$  nm is seen as ideal, since it transmits well through the vitreous and allows a much higher intensity than for non-visible wavelengths.

Due to these factors and to the simple accessibility of light sources and detectors, the first OCT imaging has been carried out exclusively in a wavelength range centered at  $\approx 800$  nm, which is still the dominant wavelength regime used for clinical systems in the case of retinal OCT [9]. However, besides absorption, the scattering of photons, which is inherently important for OCT imaging, influences image quality. In the spectral range of  $\approx 600$ -1500 nm, the reduced scattering coefficient  $\mu_s$  and wavelength dependence of the

reduced scattering coefficient in many biological tissues can usually be described according to the power law  $\mu_s(\lambda) = a\lambda^{-w}$ , where typical values of  $w$  range from 1-2 [45].

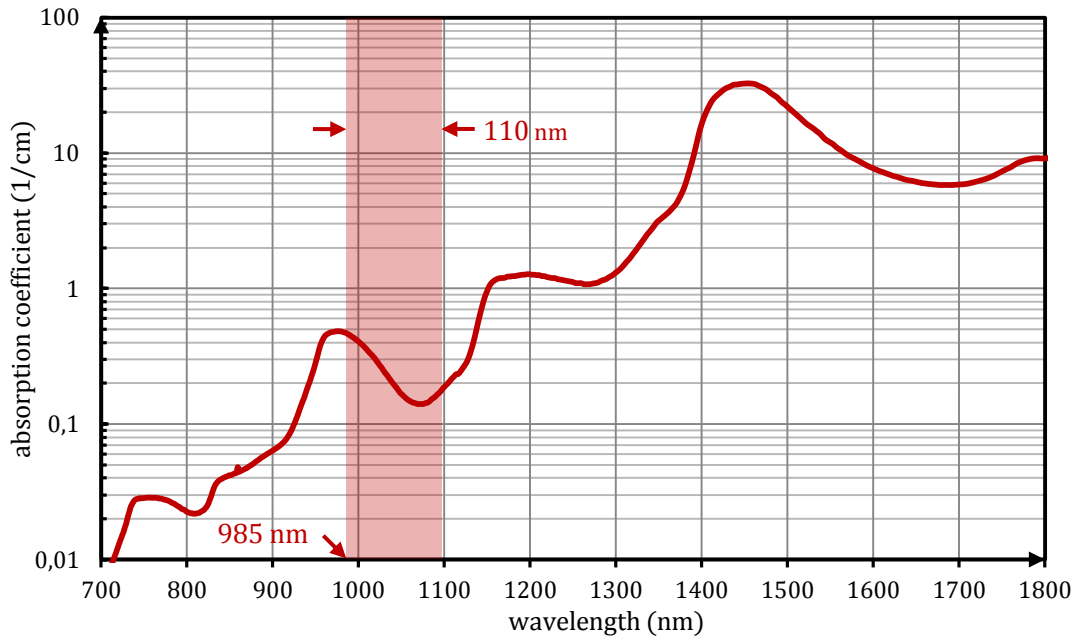


**Fig. 25** - Absorption coefficient for freshly distilled water at 22 °C dependent on wavelength, in a logarithmic representation, adapted from [44]. The local minimum of the absorption coefficient close to 1060 nm allows retinal imaging at higher wavelengths, which can facilitate high-quality imaging of structures beneath the retinal pigment epithelium.

Therefore, OCT imaging of highly scattering tissue can benefit from longer wavelengths, since the scattering probability of photons is reduced and, as a result, larger penetration depths can be realized at the same OCT sensitivity. With the exception of retinal imaging, almost all OCT applications require imaging in highly scattering, optical dense tissues where absorption plays a considerably small role, due to water or other contents at near-infrared wavelengths. Consequently, the preferred wavelength region for OCT imaging of tissues other than the posterior eye became 1300 nm, where suitable light sources were available. This wavelength is particularly suitable for corneal measurements, but it does not transmit well enough through the vitreous to create images of the human retina. For instance, only 5% of the power incident on the cornea reaches the retina after transmission through 20 mm of vitreous. Upon double-pass and assuming a perfectly reflecting retina, only less than 0.5% returns at 1300 nm [45].

Increased penetration depths at 1300 nm compared to 800 nm were first demonstrated in different investigations in the mid-1990s [33]. If even longer wavelengths are used, water absorption increases strongly which difficults OCT imaging of biological tissues. It has been proved that, at 1550 nm, OCT imaging of biological tissue can

produce similar image quality compared to 1300 nm if the proportion of water is not too high [46]. Since the retina consists of rather transparent and low scattering tissue, retinal OCT at 800 nm can result in a very good image quality and the major intra retinal layers can be distinguished. For OCT imaging of optically more dense tissue located beneath the retinal pigment epithelium, such as the choroid, longer wavelengths may become attractive in an effort to penetrate deeper into the tissue. However, due to high losses on the way through the eye and back, OCT is not possible for wavelengths exceeding 1150 nm. Nevertheless, as shown on Fig. 25, the absorption in water has a distinctive, local minimum at 1060 nm which makes retinal OCT imaging highly attractive in this wavelength range. Other advantages of retinal imaging at 1060 nm are the lower dispersion of light in water (deeper penetration) or the fact that the patient is not disturbed by 1060 nm light (infrared).

### 3.2.2. Swept sources for OCT

Swept sources, or more specific wavelength swept light sources, are characterized by a continuous change of the output wavelength within a certain wavelength sweep range  $\Delta\lambda$  as a function of time  $\Delta T$ . This time period is referred to as a forward sweep (ascending wavelength) or a backward sweep (descending wavelength). On the one hand, the sweep range needs to be sufficiently large so it can guarantee an adequate axial resolution (see chapter 2.4.2.). On the other hand, the instantaneous linewidth  $\delta\lambda$  of the swept source must be small enough to enable a sufficient imaging range.

Besides these two conditions and a sufficiently high sweep speed in the order of a few kHz [46], there is one more fundamental requirement for SS-OCT imaging which must ensure that the swept light source provides enough optical output power.

### 3.2.3 - Axsun Swept Source

The swept source used in this project is the Axsun OCT Swept Source Engine, Model SSOCT-1060 (Fig. 26) from AXSUN Technologies Inc., Billerica, Massachusetts, USA.

The basic system specifications of the engine are [47]:

- minimum laser average output power of 15 mW;
- wavelength range from 985-1095 nm (-10 dB), Near-Infrared (NIR) region;
- center wavelength between 1040-1060 nm;

- maximum sweep rate of 100 kHz;
- sweep trigger (0 to 1.2 V, 50  $\Omega$ );
- K-clock output: 0.2 - 0.8 V, 50  $\Omega$ , (< 350MHz).

According to the manufacturer's specifications, this swept source engine (center wavelength 1060 nm and a power >14.7 mW) is a class 3B laser product and *...is hazardous if the eye is exposed directly, but diffuse reflections such as from paper or other matte surfaces are not harmful.*

To minimize the possibility of personal injury and/or damage of the equipment the manufacturer specifies a series of precautions to be followed when using this equipment which can be found in its Operator Manual [47].



**Fig. 26** - Axsun OCT Swept Source Engine – Benchtop Version.

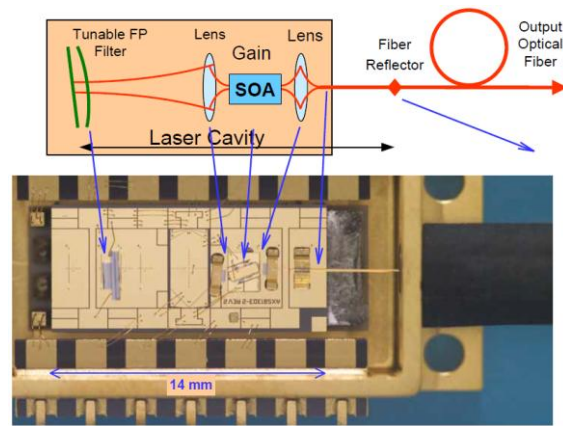


**Fig. 27** - Axsun Micro-Electro-Mechanical System (MEMS) Tunable Filter technology [48].

The Axsun OCT Swept Source Engine, Model SSOCT-1060 is based on Axsun Technologies' optical integration platform and a proprietary Micro-Electro-Mechanical Systems (MEMS) (Fig. 27). The laser consists of a semiconductor gain element and high finesse tunable filter (broad tuning bandwidth > 100 nm in micro seconds) with a short cavity length to enable rapid tuning. It has a coherence length typical of 10 mm minimum and 12 mm maximum (round trip) [47].

The time averaged spectral power output of a typical SSOCT-1060 engine is presented in Fig. 28. The selected wavelength range is  $\Delta\lambda = 110 \text{ nm}$  (985.0-1095.0 nm), that corresponds to 1376 samples in a maximum of 1510 for all range [47]. Thus the proportion of the bandwidth used is  $\approx 91\%$  and the instantaneous linewidth  $\delta\lambda$  is:

$$\delta\lambda = \frac{\Delta\lambda}{\text{N.}^\circ \text{ points}} = \frac{1095.0 - 985.0}{1376} \cong 80 \text{ pm} \quad (49)$$

Based on the assumption that the refractive index  $n = 1$ , the spectral power exhibits a Gaussian shape and considering for the center wavelength  $\lambda_0 = 1040 \text{ nm}$ , the axial resolution  $\delta z$  in air provided by this swept source is (from eq. 25):

$$\delta z = \frac{2 \ln(2)}{\pi} \cdot \frac{\lambda_0^2}{\Delta \lambda} = \frac{2 \ln 2}{\pi} \cdot \frac{1040^2}{110} \approx 4.34 \text{ } \mu\text{m} \quad (50)$$

and selecting the useful wavelength range ( $N = 1376$  samples), the depth range  $\Delta z_{\max}$  is:

$$\Delta z_{\max} = N \times \delta z = 1376 \times 4.34 \approx 5.97 \text{ mm} \quad (51)$$

So, based on the same assumptions made for axial resolution, the coherence length  $l_c$  (round trip) is:

$$l_c = 2 \times \Delta z_{\max} = 2 \times 5.97 \approx 11.9 \text{ mm} \quad (52)$$

The calculated value meets with the manufacturer's specifications: coherence length of 10 mm minimum and 12 mm typical (round trip).

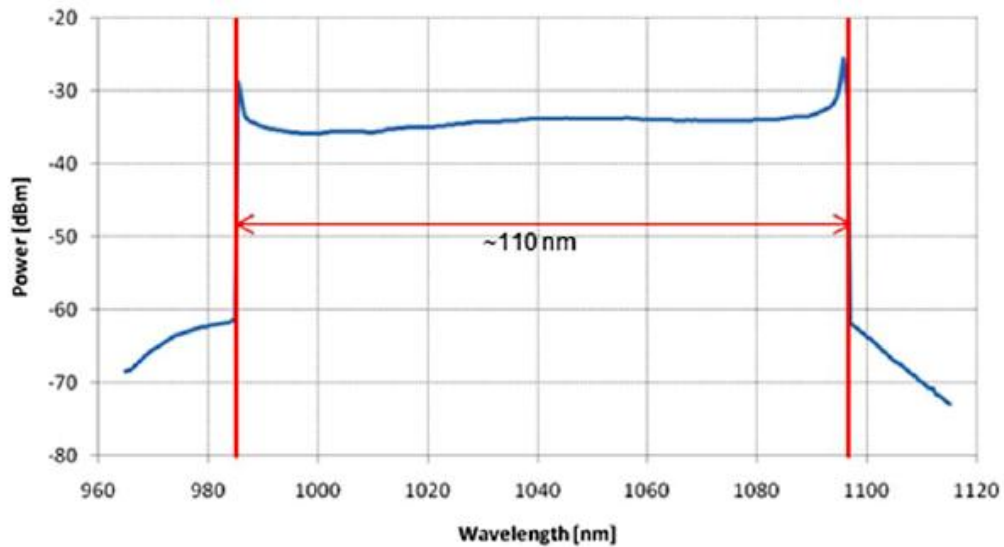
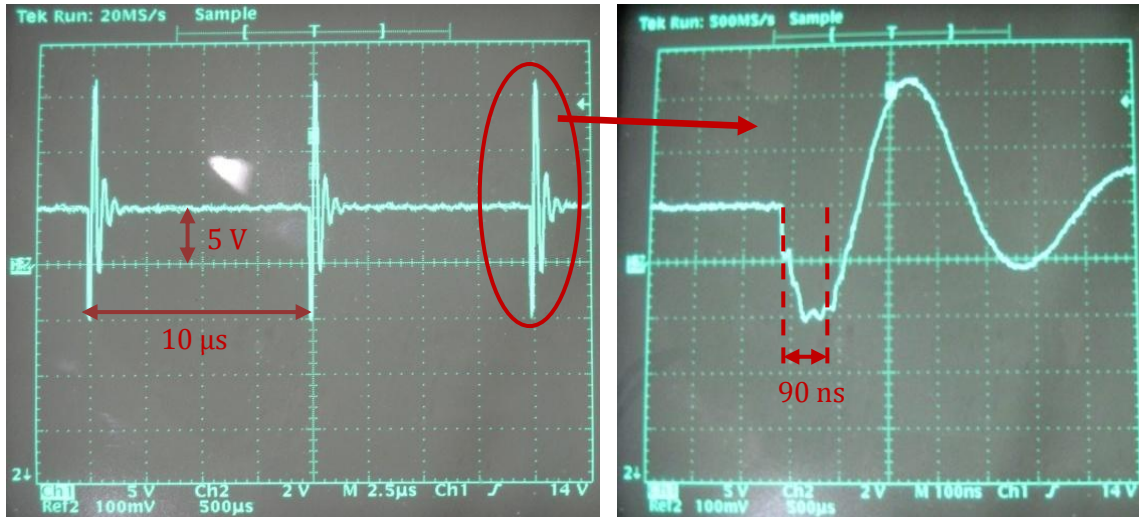


Fig. 28 - Time averaged power output of a typical SSOCT-1060 Engine [47].

The swept source generated a start TTL trigger signal every  $10 \text{ } \mu\text{s}$  that was used to initiate and synchronize the data acquisition process for each A-scan (Fig. 33). This trigger signal, when observed in the oscilloscope, confirms the repetition rate of  $10 \text{ } \mu\text{s}$  (Fig. 29 left). Note that the amplitude of the trigger signal that comes from the swept source is modified by a digital delay/pulse generator to TTL 5 V level for DAC board recognition and a delay incremented of  $90 \text{ ns}$  is also generated (Fig. 29 right). This delay allows adjusting the difference in time between clock and signal (fiber length plus balance detector).

The laser duty cycle, which is the interval of time where the laser is on (red line in the Fig. 33), is about  $\approx 4.45 \mu\text{s}$  ( $\approx 44.5\%$ ). During the backward sweep, the laser is turned off.



**Fig. 29** - Trigger signal generated from the SSOCT-1060 engine after passing a digital delay/pulse generator

In this swept source engine, a Mach-Zehnder interferometer (MZI) is embedded and conditioned with electronics for providing a frequency clock signal (Fig. 30). The MZI generates a periodical signal for every sweep-to-sweep variation and it shows maxima and minima which are equally spaced in optical frequency domain (k-space).

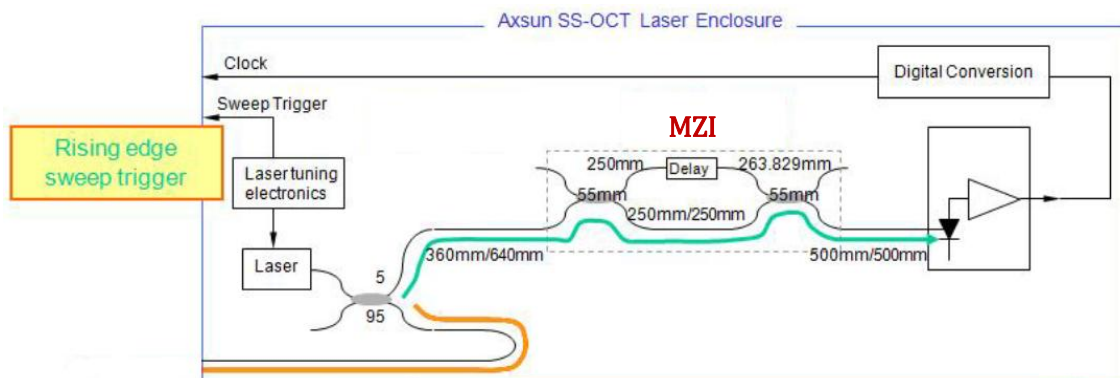


**Fig. 30** - Axsun SS-OCT laser enclosure [47].

The difference between two maxima is defined by the free spectral range of the MZI. The manufacturer does not specify in detail how the signal is electronically generated, but to realize its operation and support on the paper *Generic real-time uniform K-space sampling method for high-speed swept-Source optical coherence tomography* [43] its operation seems to be the following (Fig. 31 and Fig. 32).



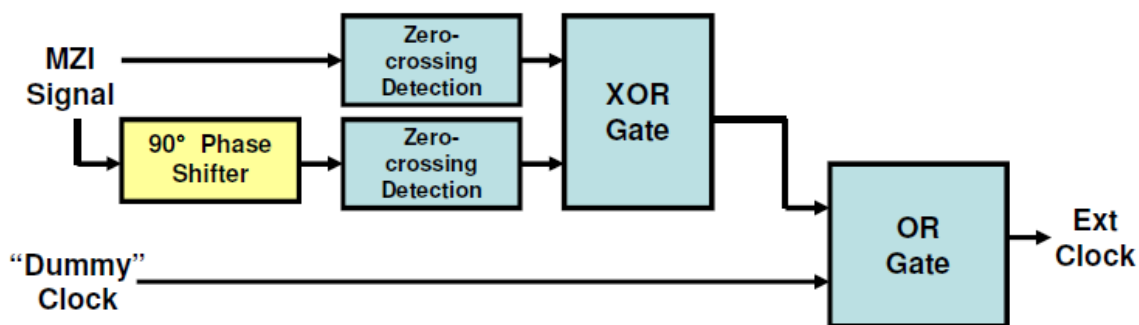


Fig. 31 - Schematic of external clock generator [43].

A broadband  $90^\circ$  phase is employed for producing a quadrant signal from the MZI signal.

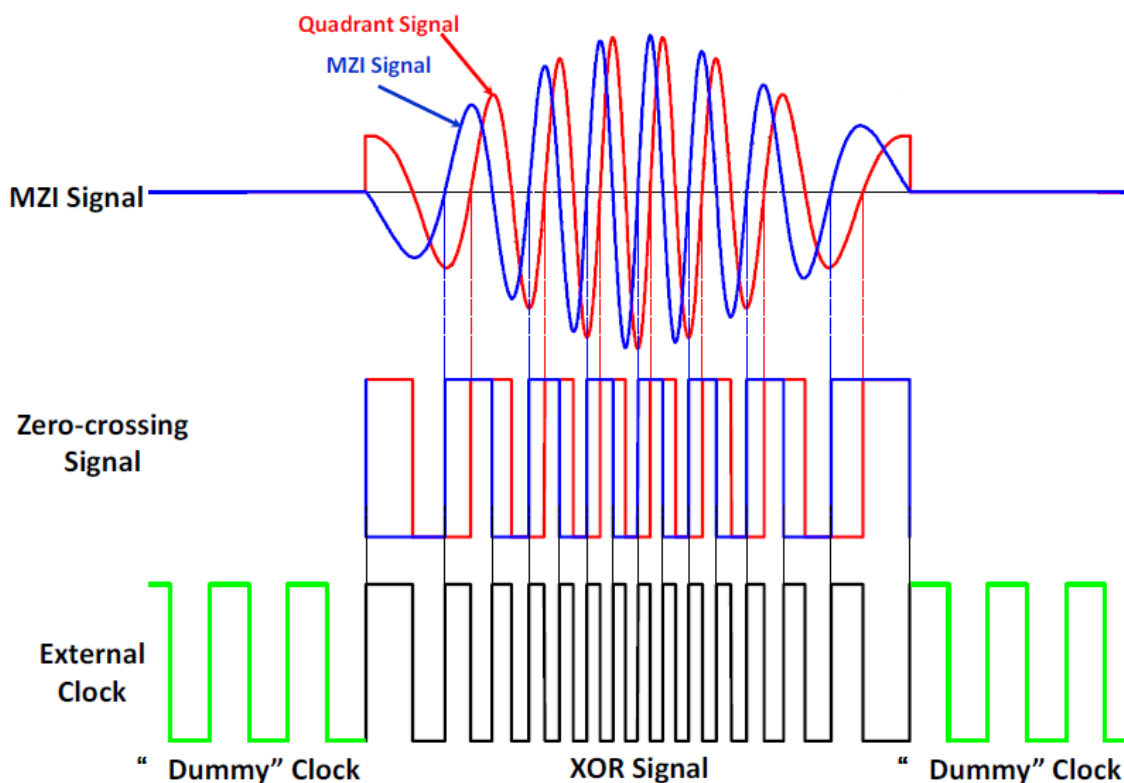
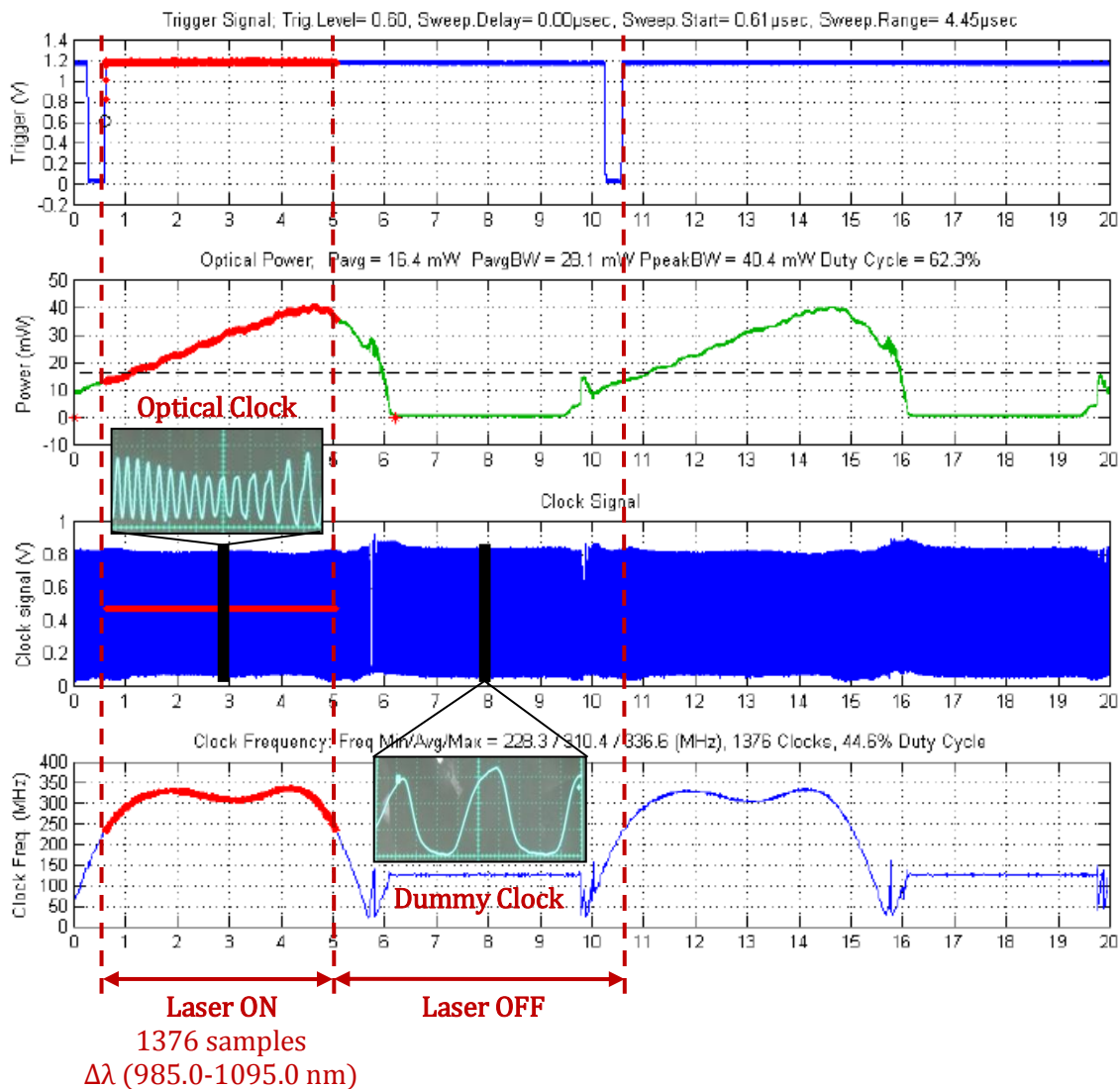


Fig. 32 – Clock signal obtained from an MZI signal [43].

The two square waves are then combined through an exclusive OR (XOR) gate which generates an external clock pulse when the two square waves overlap (laser on). The combination of a quadrant phase shifter and an XOR gate ensures the external clocks have an  $\approx 50\%$  duty cycle. To fill the empty gap on the external clock between adjacent A-scans (laser off), a dummy clock signal is generated within the time duration

complementary to the time gate for the zero-crossing detection and then combined with the zero-crossing clock signal by an OR gate to form a final external clock [43].



**Fig. 33** - The trigger, optical power, clock signal and clock frequency for a typical OCT-1060 engine. Adapted from [47].

So, by directly clocking the DAC with this signal clock (the optical clock works well for the specific A/D used in this work), the fringe can be automatically sampled at different intervals in time but with equal  $k$  spacing to produce a linearized fringe signal. This allows a direct Fourier transform of the fringe data to generate OCT intensity images and eliminates the need for the Mach-Zehnder calibration and fringe linearization procedure. Also, the data acquisition is only made when the laser is on thereby reducing the data transfer and storage requirements for the raw fringe data.

### 3.3. Balanced Detector

Through the observation of the experimental setup, the back reflected light from the reference and sample arms is redirected to a single mode fused 2x2 (50:50) fiber couplers for interference. Next, both outputs of the interferometer are injected in the two inputs of a balance detector and the signals are subtracted electronically (Fig. 35).

The balance detector used is the Thorlabs PDB145C (Fig. 35), a proved fixed gain balanced amplified photodetectors for OCT with a bandwidth  $B_w$  (3dB) of 15 MHz [50]. It consists of two well matched InGaAs photodiodes (wavelength range between 800 nm - 1700 nm and maximum input power of 20 mW) and an ultra-low noise, high-speed transimpedance amplifier (Fig. 34) that generates an output voltage proportional to the difference between the photocurrents in the two photodiodes INPUT+ and INPUT- (conversion gain of the RF - radiofrequency OUTPUT is  $51 \times 10^3$  V/W) [50]. The maximum RF OUTPUT voltage swing of the fixed gain is  $\pm 3.6$  V for high impedance loads and  $\pm 1.8$  V into  $50 \Omega$  loads [50]. The RF OUTPUT signal should not exceed the maximum output voltage to avoid saturation.

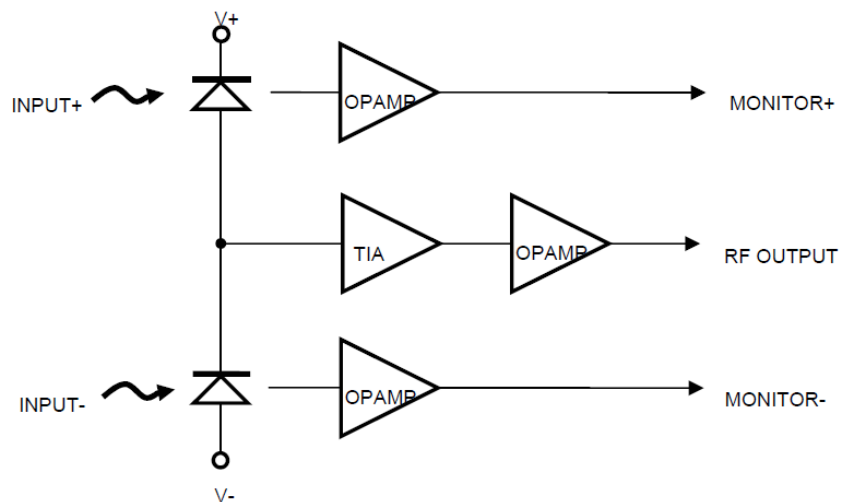


**Fig. 34** - Functional block diagram for the Thorlabs PDB145C balance detector [50].

Therefore the optical input power (or the difference between the optical input powers) should not exceed the continuous wave (CW) saturation power, the point at which the output of the photodetector becomes nonlinear (the difference between the two optical input signals is greater than  $70 \mu\text{W}$  at 1550 nm) [50].

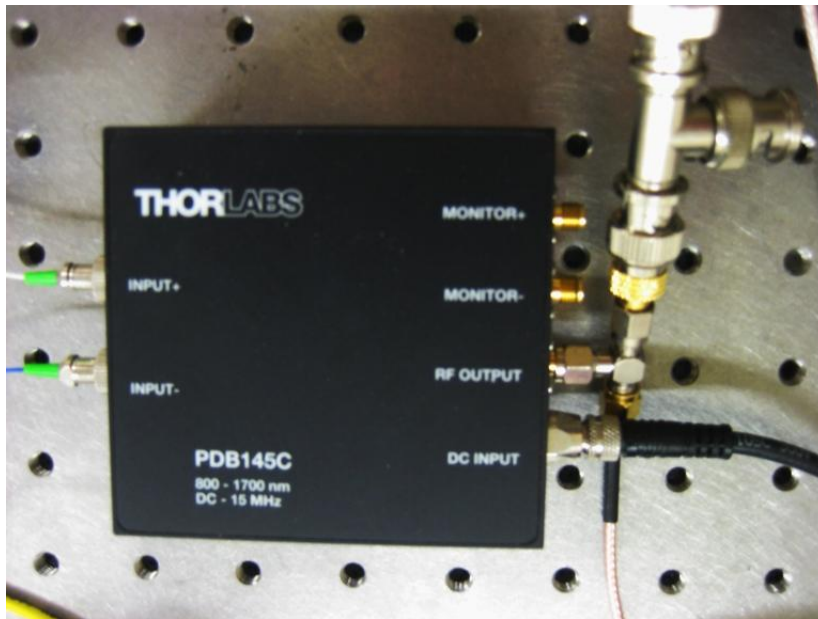


Fig. 35 - Thorlabs PDB145C balance detector.

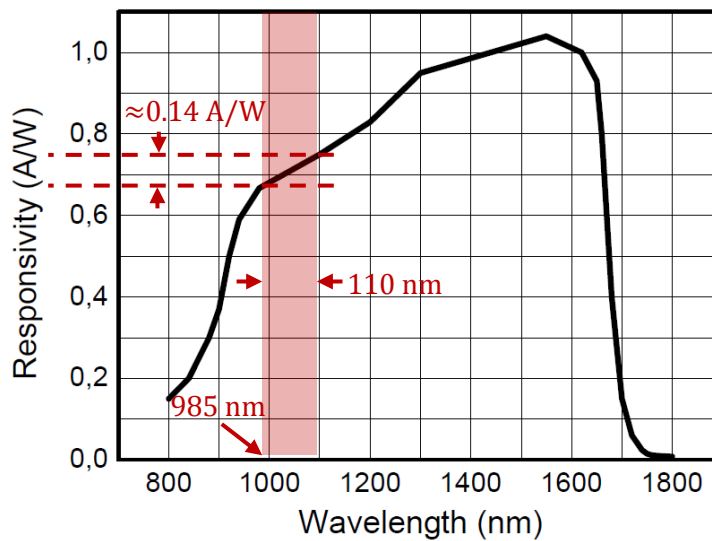


Fig. 36 - Typical responsivity curve for the Thorlabs PDB145C balance detector. Adapted from [50].

The signal monitor outputs (+ and -) allow the observation of the input power (+ and -) levels and are used as independent power meters for each channel. These outputs are low frequency outputs and cannot be used to measure RF modulation on the signal [50]. The maximum output voltage swing of the MONITOR output is +10 V and saturation will occur at optical input power greater than  $100\mu\text{W}$  [50]. The monitor outputs are designed to drive high-impedance loads.

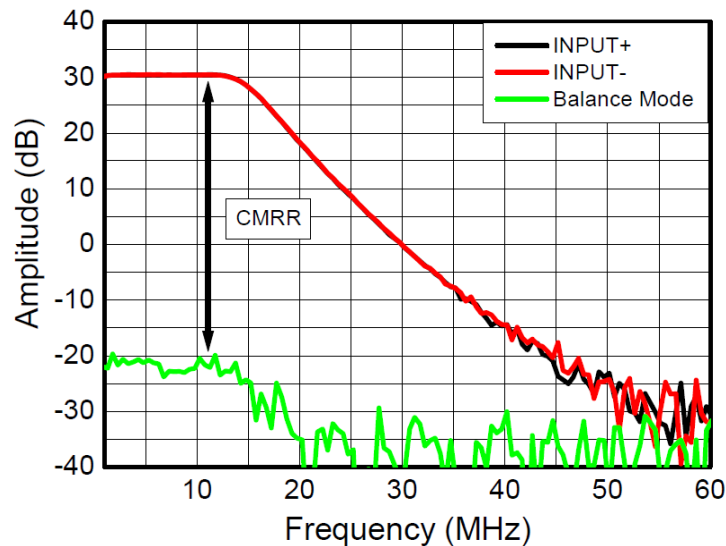


Fig. 37 - Typical frequency response curves of PDB145C [50].

This model uses a well-matched pair of InGaAs PIN photodiodes with a detector diameter of 0.3 mm [50]. The responsivity difference for the range of wavelength used is  $\approx 0.14$  A/W [50], being higher for longer wavelengths (Fig. 36).

Fig. 37 shows typical frequency response curves of PDB145C. The 3 dB bandwidth of the RF OUTPUT is  $\approx 15$  MHz and for this range the device has a high common-mode rejection ratio (CMRR).

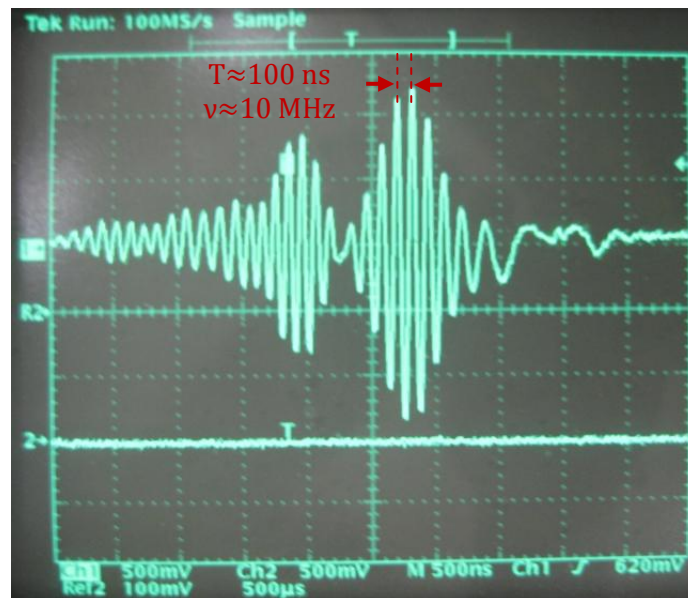


Fig. 38 - Interferometric signal observed in an oscilloscope with a time scale of 500 ns/div.

This is important because the signal of interest (relevant information contained in the voltage difference between two input signals) is represented by a small voltage fluctuation superimposed.

Furthermore, the frequency response is constant for the frequency range of interest. As it can be seen in the previous example (Fig. 38), the interferometric term oscillates with a frequency of  $\approx 10$  MHz [50].

The following graphic (Fig. 39) shows typical noise spectra on RF OUTPUT with the INPUTs blocked. The lower curve is measured with the same setup but switched off, i.e., it represents the measurement system's noise floor.

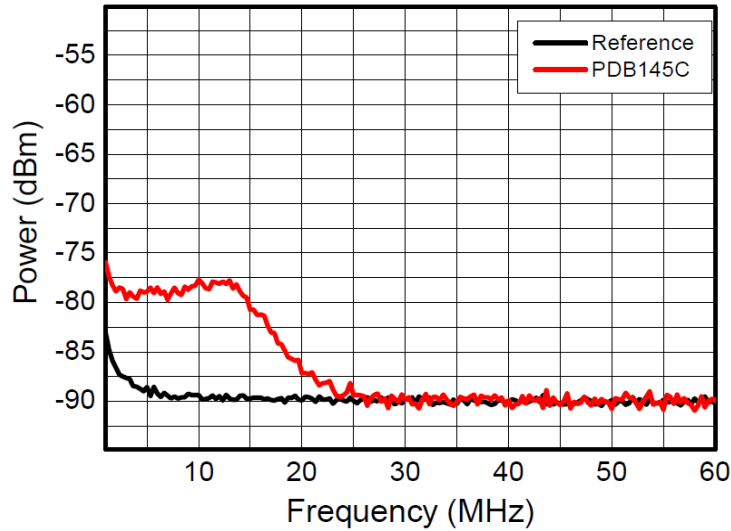


Fig. 39 - Typical spectral noise curves of PDB145C [50].

This model has a minimum noise-equivalent power (NEP)  $3.2 \text{ pW}/\sqrt{\text{Hz}}$  from DC-10 MHz [50]. The integrated noise from DC-15 MHz is  $12 \text{ nW}_{\text{RMS}}$  ( $\approx -80 \text{ dB}$ ) [50]. This input optical noise level is the approximate minimum optical signal ( $P_{\text{min}}$ ) that can be detected with this model. The overall output voltage noise ( $U_{\text{RMS}}$ ) across 50 Ohm load is  $0.37 \text{ mV}_{\text{RMS}}$  [50].

The conversion gain of the radiofrequency (RF) OUTPUT is  $51 \times 10^3 \text{ V/W}$  and the maximum RF OUTPUT voltage swing of the fixed gain is  $\pm 3.6 \text{ V}$ . So the maximum optical power ( $P_{\text{max}}$ ) detected with this equipment is  $\approx 70 \text{ }\mu\text{W}$  (difference between the two optical input signals). So, the theoretical dynamic range ( $D_{\text{dB}}$ ) of this OCT system is:

$$D_{\text{dB}} = 10 \cdot \log\left(\frac{P_{\text{max}}}{P_{\text{min}}}\right) = 10 \cdot \log\left(\frac{70 \times 10^{-6}}{12 \times 10^{-9}}\right) \approx 38 \text{ dB} \quad (53)$$

Whereas the signal obtained from the output of the detector shown in Fig. 38 has a root mean square:

$$U_{\text{RMS}} = \frac{U_{\text{max}}}{\sqrt{2}} = \frac{1,2}{\sqrt{2}} \approx 0.85 \text{ V} \quad (54)$$

The SNR at the output of the optical balance receiver is:

$$\text{SNR} = 20 \cdot \log \left( \frac{U_{\text{RMS}}(\text{Signal})}{U_{\text{RMS}}(\text{noise})} \right) = 20 \cdot \log \left( \frac{0.85}{0.37 \times 10^{-3}} \right) \approx 67 \text{ dB} \quad (55)$$

At first, we could think that the electrical signal resultant from RF OUTPUT would be zero because both signals come from the same interferometer, but based on the conservation of energy, the interferometric terms that result from the Michelson interferometer based on 2×2 fiber couplers exhibit a phase difference of  $\pi$  (Choma *et al.* on their paper *Instantaneous quadrature low-coherence interferometry with 3×3 fiber-optic couplers* [49]), describe a simpler formalism that predicts phase shifts for interferometers based on 2×2 and 3×3 fiber optic couplers. However, the DC terms which do not depend on  $\Delta z$  and carry no relevant information for OCT have no phase difference. Therefore, OCT's relevant fringe signal is doubled, whereas the DC terms are cancelled out. Besides, removing the unwanted DC signal enables us to use the available dynamic range of the analog to digital conversion more effectively. Another main advantage of this approach is that excess intensity noise originated from the light source can be suppressed yielding improved sensitivity. Nevertheless, this term must be replaced in the calculations by the beat noise term, which corresponds to the component of excess noise not removed by the balanced detector [24].

### 3.4. Data Acquisition and Function Generator

The sweep-source optical coherence tomography (SS-OCT) implemented involve a theoretical raw data acquisition rate (A-scan rate) of 100 000 points/s (limited by the spectral sweeping period of 10  $\mu\text{s}$  of the swept source). Moreover the laser beam is steering by two high-speed scanning galvanometer mirrors position system (maximum 250 Hz). To deal with these requirements the data acquisition is carried out by a PCI (Peripheral Component Interconnect) Express XMC (Switch Mezzanine Card) Module X5-400 (Innovative Integration Incorporated). The wave functions that will position the galvanometers are generated with the aid of PCI-6010 board (National Instruments Corporation).

The X5-400M (Fig. 40 left) is an XMC IO (input/output) module featuring two 14-bit, 400 MSPS (samples/second) A/D (analog/digital) and two 16-bit, 500 MSPS D/A (digital to analog converter) channels with a Virtex5 FPGA (field programmable gate

array) computing core and PCI Express host interface on a standard XMC module [51]. This module includes a high performance DSP (digital signal processing) Xilinx Virtex5 SX95T with 512 GB DDR2 DRAM (double-data-rate dynamic random access memory) and 4 MB QDR-II SRAM (quad data rate static random access memory) [51].

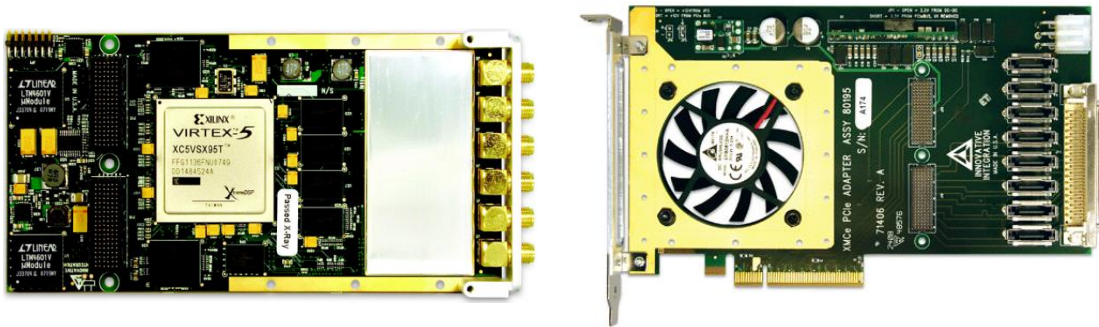


Fig. 40 - XMC module X5-400M (left) and PCI express x8 module interface (right) [51].

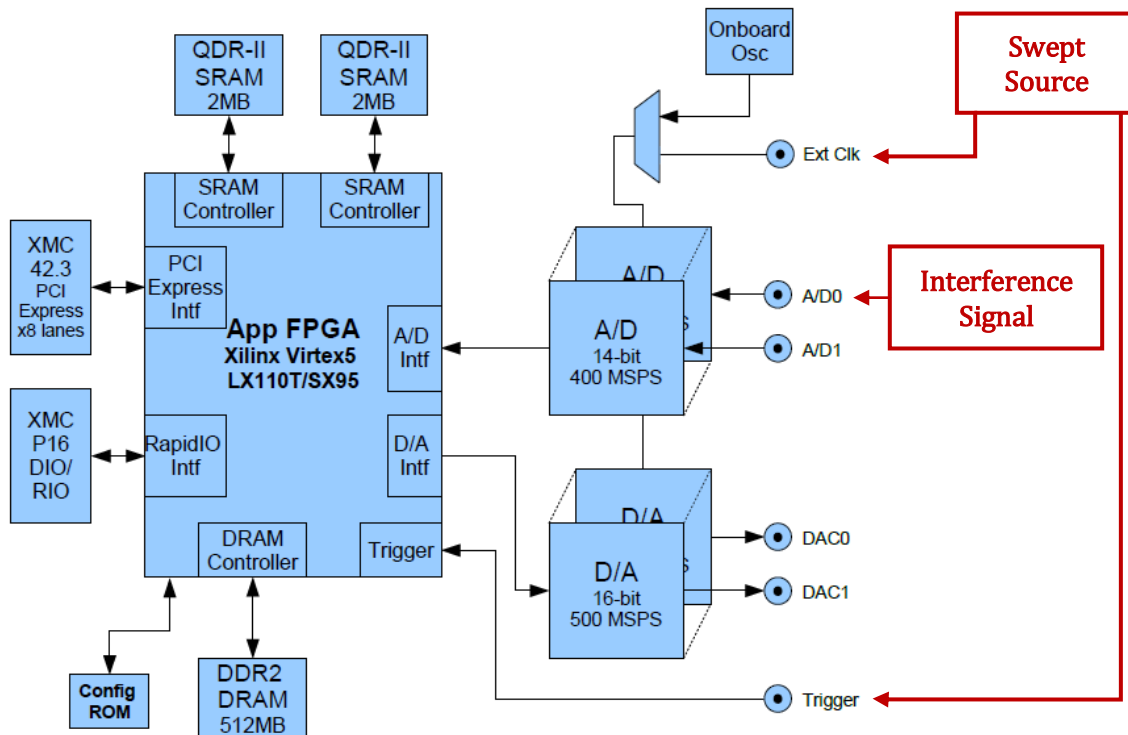


Fig. 41 – XMC module X5-400M block diagram. Adapted from [51].

The XMC module is coupled with a high performance 8-lane PCI Express interface (Fig. 40 right) that provides over 1 GB/s sustained transfer rates (in each direction simultaneously) into the PC (personal computer) host [51].

The A/D and D/C channels operate synchronously and share a common clock for simultaneously sampling systems using the external clock input (clock output from the swept source). This situation is not compatible with the assembly used, since the period of



the clock from the swept source is not constant in time. This is one of the reasons why another board is used to generate the wave functions that will position the galvanometers. Another reason is that the rate restrictions of the D/A converters limit the usable sample rates of the A/D converters. According to the specifications of swept source, its maximum sample rate is 336.6 MSPS, so this board, used only the A/D channels, is perfectly capable of handling this sample rate.

The trigger input signal is external and comes from the TTL trigger signal of the swept source every 10  $\mu$ s. The acquisition mode used is NPT (no pre-triggering) which means that only the signal after the trigger was acquired and processed [50].

The analog inputs have a range in DC (direct current) mode of 2  $V_{p-p}$  and an offset of 700  $\mu$ V. The ground noise (input grounded and acquisition rate as 400 MSPS) is about 350  $\mu$ V<sub>p-p</sub> (-95 dB) [50].

The wave functions are generated by software through the analog output (AO) channels of the National Instruments PCI-6010 board (Fig. 42 left).

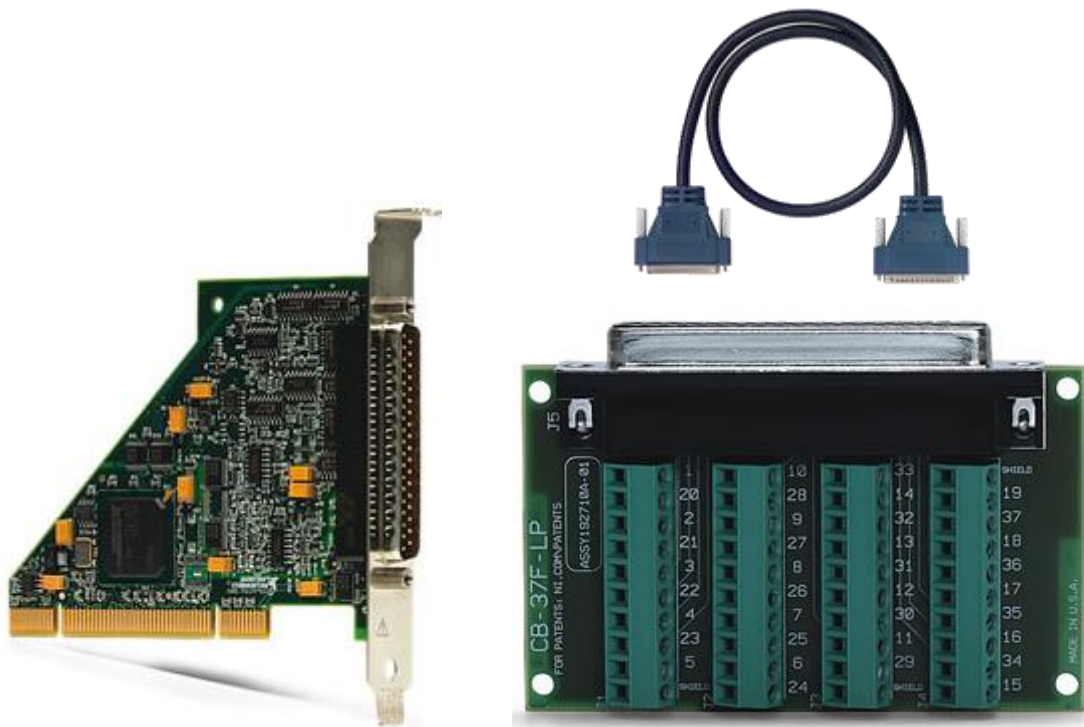


**Fig. 42** - National Instruments PCI-6010 board (left); National Instruments CB-37F-LP terminal block (right below) and National Instruments SH37F-37M cable (right above) [51].

This board supports two static analog output channels with a range of  $\pm 5$  V DC, resolution of 16 bits, differential nonlinearity (DNL) of  $\pm 1$  LSB, settling time (full scale step to 100 ppm) of 1.2 ms and the noise (50 kHz bandwidth) is 135  $\mu$ V [51].

In order to provide easy access to the 37 pins on the board, a National Instruments CB-37F-LP terminal block is used (Fig. 42 right below). This block and the board are connected through a cable National Instruments SH37F-37M (Fig. 42 above). This is a 37-pin D-SUB cable shielded for electrically noisy environments [51]. It provides a female 37-pin D-SUB end for device connectivity and a male 37-pin D-SUB end for connecting to connector blocks.

### 3.5. Fixed Focus Collimator

The two collimators used in this project are both of type Thorlabs F260APC-C (Fig. 43) and have the purpose of collimating the light that comes from the fiber optics. Some of the main collimator properties are: effective focal length  $f = 15.52$  mm for  $\lambda = 1310$  nm (due to chromatic aberration, the effective focal length of the aspheric lens is wavelength-dependent), numerical aperture  $NA = 0.16$ ; collimated beam diameter  $D = 2.8$  mm (theoretical  $1/e^2$  diameter at 1 focal length from lens); theoretical full-angle beam divergence  $\theta = 0.034^\circ$  and wavelength range of 1050-1620 nm [54].

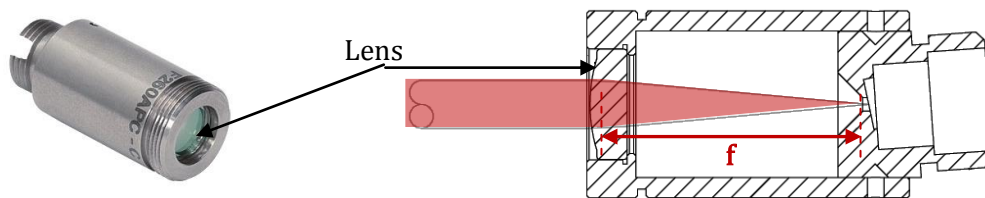


**Fig. 43** - Thorlabs F260APC-C collimator photo (left) and schematic (right). Adapted from [54].

The aspheric lens is factory-aligned so that it is one wavelength-adjusted focal length away from the fiber tip when inserted into the collimator. In addition, the aspheric lens has an anti-reflective AR coating that minimizes surface reflections. The value of the reflectance decreases with the wavelength (Fig. 44) and inside the region of interest (985-1095 nm) the smaller wavelengths have a value of reflection which can cause some noise fringes. Furthermore, the biggest wavelengths that achieve greater depth and, therefore undergo more scattering, are more attenuated with this collimator.

Nevertheless the connector exploits a ferrule that has an  $8^\circ$  end face with an ultra PC polish, typically leading to a return loss greater than 60 dB.

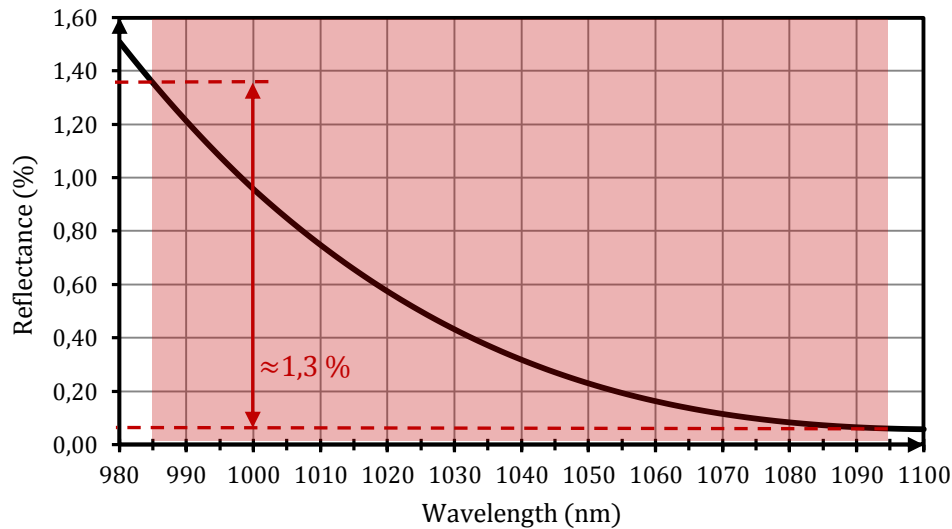


**Fig. 44** – AR coating of the collimator Thorlabs F260APC-C as a function of the wavelength. Adapted from [54].

The collimated beam, spreading due to diffraction, is not considered here because the propagation distance through space is very small.

### 3.6. Scan Lens

The two scan lenses used are of type Thorlabs LSM03-BB (Fig. 45). They are made with telecentric objective and benefit from the flat imaging plate as a laser beam is scanned across the sample by making them ideal for optical imaging. A telecentric scan lens also maximizes the coupling of the light scattered or emitted from the sample (the signal) into the detection system. In addition, the spot size in the image plane is nearly constant over the entire field of view (**FOV**), resulting in constant image resolution and minimizing image distortion. The important optical features are [54]:

- anti-reflective (**AR**) coating designed to minimize back reflections on a range of 800 to 1100 nm;
- magnification (**M**) of 5 times;
- the effective focal length (**f**) is wavelength dependent and varies between 35.78 mm ( $\lambda = 850$  nm) and 35.88 mm ( $\lambda = 1050$  nm);
- working distance (**WD**), which is the distance between the tip of the scan lens housing and the front focal plane of the scan lens, is also wavelength dependent and varies between 25.1 mm ( $\lambda = 850$  nm) and 25.0 mm ( $\lambda = 1050$  nm);

- scanning distance (**SD** = 18.9 mm) is the distance between the galvo mirror pivot point and the back mounting plate of the objective;
- depth of view (**DOV** = 0.58 mm), corresponds to the distance between the parallel planes on either side of the front focal plane where the beam spot diameter is  $\sqrt{2}$  greater than at the front focal plane;
- field of view (**FOV** = 9.4 mm × 9.4 mm), is the maximum size of the area on the sample that can be imaged ( $FOV = 2 \times f \times \tan(SA)$ );
- parfocal distance (**PD** = 50.5 mm), is the distance from the scan lens mounting plane to the front focal plane;
- mean spot size (**SZ**), which is the  $1/e^2$  beam diameter in the field of focus, is wavelength dependent and varies between 15  $\mu\text{m}$  ( $\lambda = 850 \text{ nm}$ ) and 21  $\mu\text{m}$  ( $\lambda = 1050 \text{ nm}$ );
- scan angle (**SA** = 7.5°) is the maximum allowed angle (in the X or Y direction) between the beam and the optical axis of the scan lens after being reflected off of the galvo mirror.

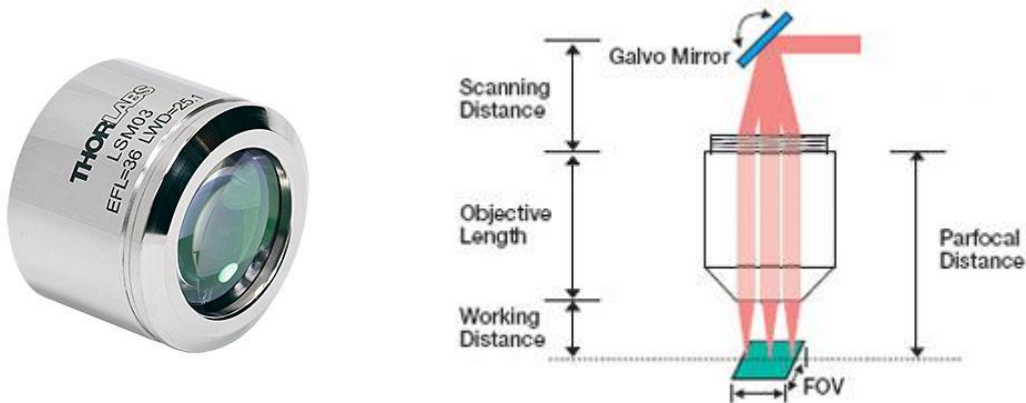


Fig. 45 - Thorlabs LMS03-BB lens photo (left) and typical OCT application (right) [54].

Note that, since the lens is telecentric, the galvo mirror pivot point must be located at the back focal plane of the objective in order to maximize image resolution. It is also necessary to take the following into consideration: the incident beam is centered in the field of view of the scan lens, the resulting spot will be circular, however, as the beam is scanned along the **x** or **y** axis of the lens, the spot will take on an elliptical shape. This new spot has a width in the sagittal and tangential directions that in general increases with the beam scan angle and decreases with the wavelength [54].

The back reflections in this lens for the 985-1095 nm (working wavelength range) are < 0.4%, having its minimum value  $\approx 1.5\%$  at the wavelength  $\lambda = 1060 \text{ nm}$  [54].

Assuming a depth of focus  $\Delta z_f$ , which is the depth range in which the focused spot diameter remains below an arbitrary limit (in this case  $\sqrt{2}$ ), it is equal to the depth of view  $\mathbf{DOV} = 0.58$  mm. The maximum and minimum values of the lateral resolution  $\Delta x$ , in the focus, can be determined for the wavelength range of interest by the expression based on equation 28:

$$\Delta x = \sqrt{\frac{2\lambda\Delta z_f}{\pi}}$$

$$\Delta x(\lambda = 985 \text{ nm}) = \sqrt{\frac{2 \times 985.0 \times 10^{-9} \times 0.58 \times 10^{-3}}{\pi}} \approx 19.1 \text{ } \mu\text{m} \quad (56)$$

$$\Delta x(\lambda = 1095 \text{ nm}) = \sqrt{\frac{2 \times 1095.0 \times 10^{-9} \times 0.58 \times 10^{-3}}{\pi}} \approx 20.1 \text{ } \mu\text{m}$$

These values (minimum and maximum) are very consistent to the mean spot size  $\mathbf{SZ}$  specifications.

### 3.7. 2D Scanning Galvo System

Dual-axis galvanometer based scanners are one of the most used types of scanning devices for transverse scanning on the sample, given their high precision positioning and good scanning resolution.

The system used is a small beam diameter (<5 mm) scanning galvo systems G SVM002 from Thorlabs Inc. with a linearity of 99.9 % (range  $\pm 20^\circ$ ) and a repeatability of 15  $\mu\text{rad}$  [54]. The system includes a dual-axis galvo motors with mirrors assembly (with silver coatings for a wavelength range: 500 nm to 2.0  $\mu\text{m}$  [54]), associated driver cards and a low noise linear power supply unit (Fig. 46).

The dual-axis galvo consists of a two galvanometer-based scanning motors. Each of them has an optical mirror mounted on the shaft and a correspondent detector that provides positional feedback to the individual control board. The angular orientation (position) of each mirror is optically encoded, using an array of photocells and a light source, both of which are integrated into the interior of the galvanometer housing. Each mirror orientation corresponds to a unique ratio of signals from the photodiodes, which allows the closed-loop operation of the galvo mirror system. Each proportional derivative (PD) servo driver circuit interprets the signals from the optical position detecting system

inside the corresponding motor and then produces the drive voltage required to rotate the mirror to the desired position (Fig. 47).

The systems can be driven to scan their full angle range of  $\pm 12.5^\circ$  with an analog position signal input range with a maximum voltage of  $\pm 10$  V [54].

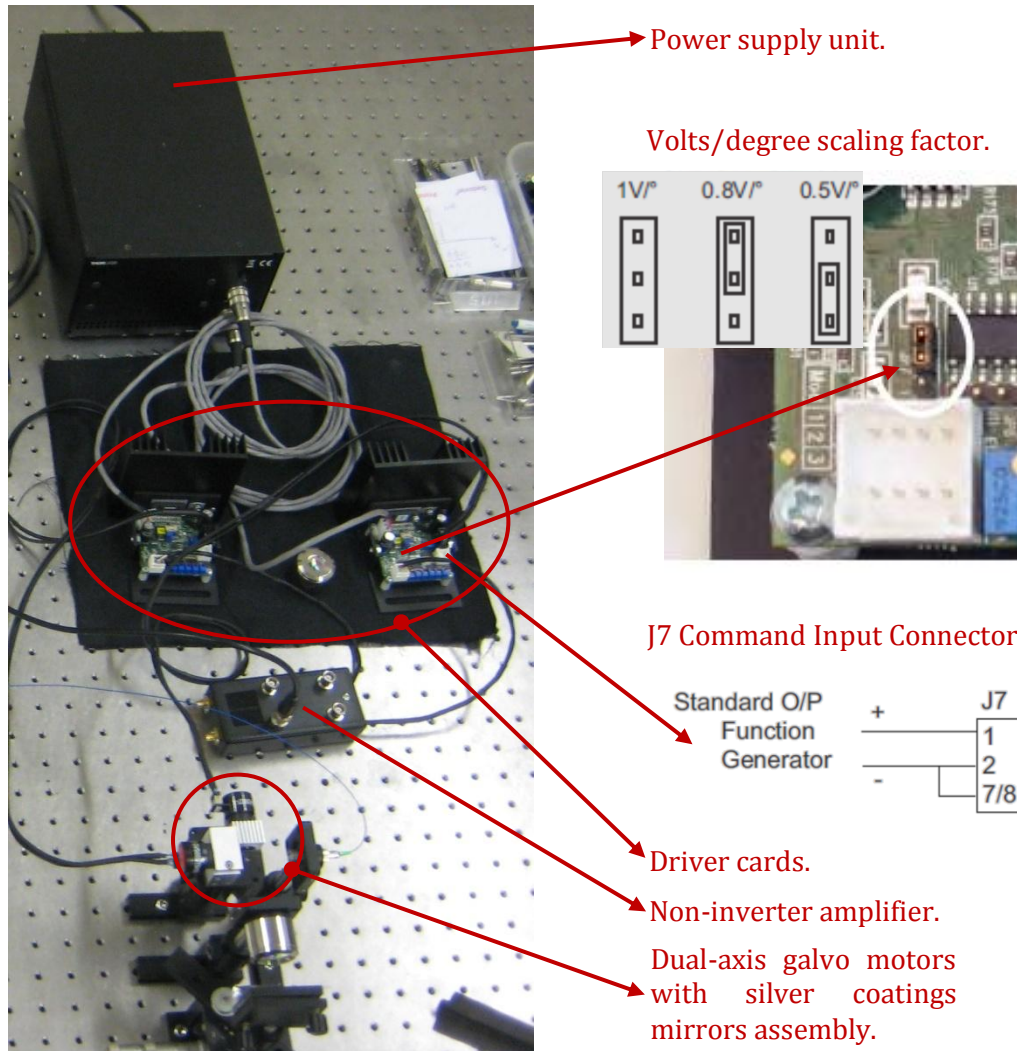


**Fig. 46** - Scanning galvo systems G SVM002 from Thorlabs Inc. assembled on the experimental setup. Adapted from [54].

The servo driver cards include an optional jumper which is used to set the Volts per degree scaling factor: 1.0, 0.8 or 0.5 (Fig. 46) [54]. When the scaling is set to 1.0 V/°, the maximum scan angle is  $\pm 10^\circ$ ; when its value is of 0.8 V/°, the maximum scan angle is  $\pm 12.5^\circ$ . The 0.5V/° scaling factor is provided to allow the full scan angle to be achieved using small input signals. In this case, the input voltage should be limited to  $\pm 6.25$  V maximum. The full scan bandwidth is 100 Hz when using a square wave control input voltage or 250 Hz when using a sine wave. For a single small-angle step of  $0.2^\circ$ , the

bandwidth is 1 kHz and, in this case, the mirror takes 300  $\mu\text{s}$  to come to rest at the command position and the angular resolution is  $0.00086^\circ$  (15  $\mu\text{rad}$ ) [54].

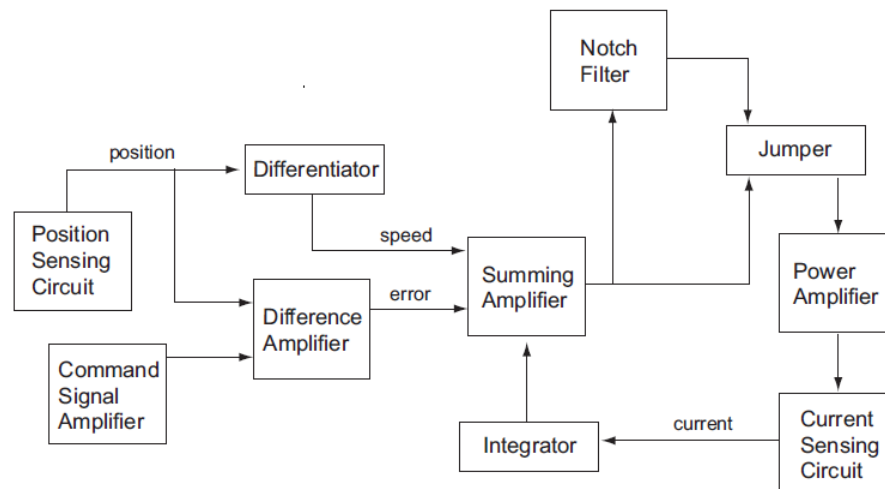


**Fig. 47** - Scanning galvo systems GSVM002 from Thorlabs Inc.: Servo Driver Board Schematic Diagram [54].

Fig. 48 shows that the reflection data for the coated mirrors is  $>96\%$ . Furthermore, the difference of the reflectance for the wavelength range of the sweep source is negligible ( $\approx 0.28\%$ ).

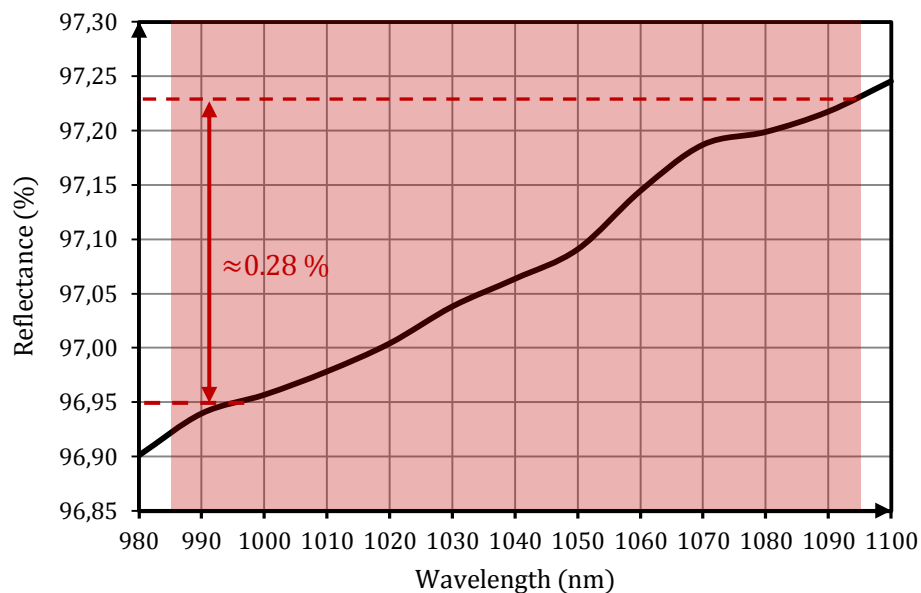


**Fig. 48** - Reflectance of the silver mirror scanning galvo systems GSVM002 as a function of the wavelength. Adapted from [54].

To control the scanning range and velocity, by changing wave amplitude, frequency and/or type, we used a signal generator. For this purpose, we needed to wire

the J7-command input connector pin from servo board to the data acquisition and control (SDAC) interface. Because the maximum voltage output of the SDAC is limited to  $\pm 5$  V and the analog position signal input range of the galvo drivers is  $\pm 10$  V, it was necessary to build a converter for each engine.

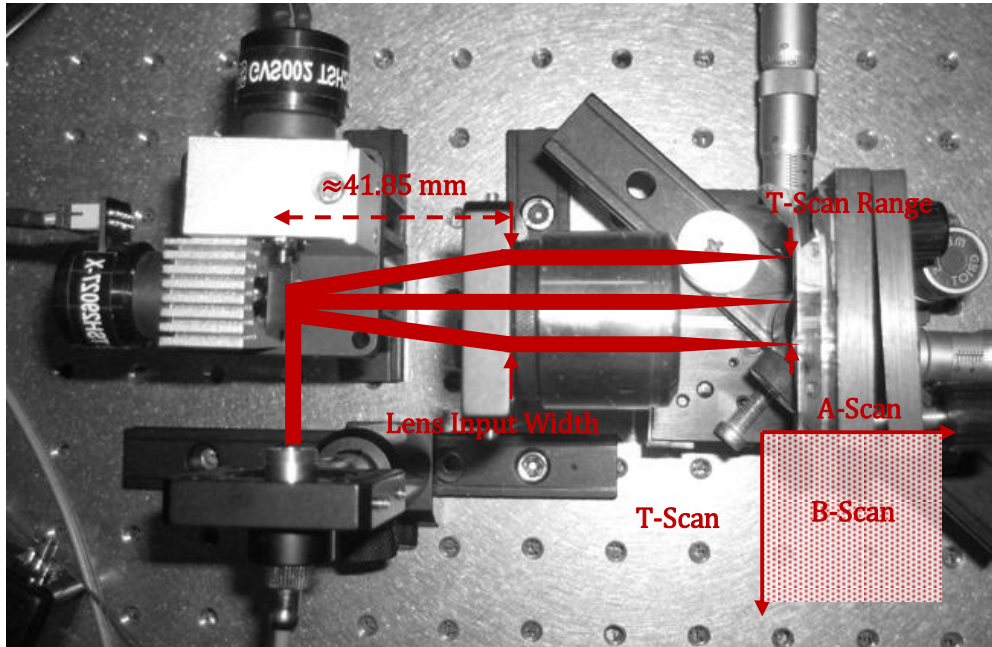


Fig. 49 – Schematic of an A-scan together with transverse scans (T-scan) to build up B-scan images.

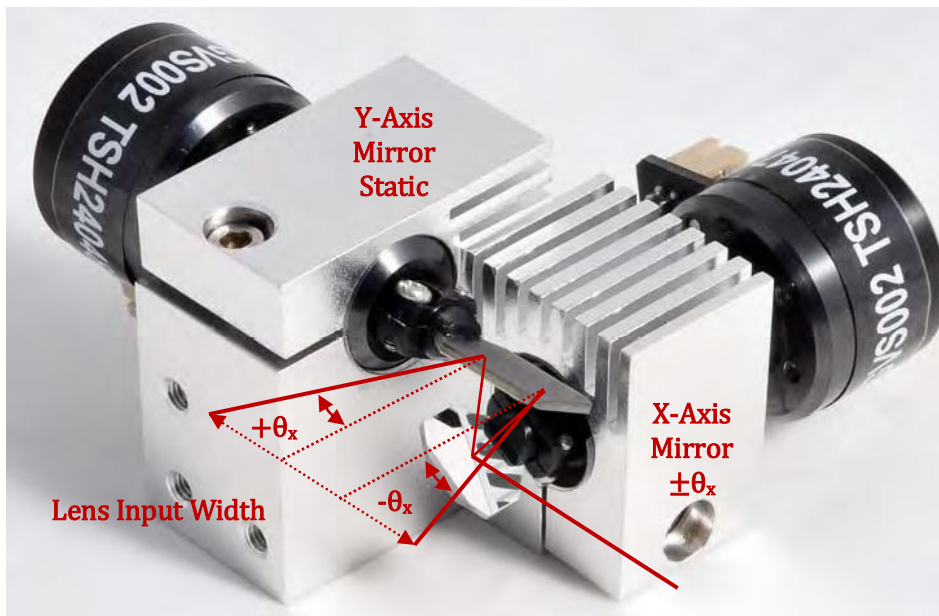


Fig. 50 – Trajectory of light by rotation of the X-axis mirror keeping the Y-axis mirror stationary.

This electronic converter is a simple non-inverter amplifier with adjustable gain up to 10 times (maximum  $\pm 12$  V) and an input impedance of  $\approx 50 \Omega$ .



At this point of the project, the OCT system is already capable of accomplishing A-scan together with transverse scans (T-scan) to build up B-scan images (Fig. 49). The T-scans are achieved via rotation of the X-axis mirror of the galvanometer (Fig. 50) keeping the Y-axis mirror stationary.

Having the concrete implemented setup, the theoretical input beam width ( $W$ ) on the lens is about  $\approx 1.88$  mm ( $W = \text{FOV}/M$  where the field of view  $\text{FOV} = 9.4$  mm and the magnification  $M = 5$ ). So, the mechanical scan angle of the X-axis mirror ( $\theta_x$ ) which gives rise to the theoretical input beam with ( $W \approx 1.88$  mm) on the lens (Fig. 49 and Fig. 50) is:

$$W = 2(D + d) \tan(\theta_x) \Leftrightarrow 1.88 = 2 \times (41.85 + 10) \times \tan(\theta_x) \Leftrightarrow \theta_x \approx 1.04^\circ \quad (57)$$

This value was determined by trigonometric calculus [58] and taking into consideration that the shortest distance between mirrors at their respective rotation axes ( $d$ ) is 10 mm, that the distance of the center perpendicular to the lens to the pivotal axis of the Y-axis mirror ( $D$ ) is  $\approx 41.85$  mm (Fig. 49) and that the Y-axis mirror is static. Angles larger than this are out of the FOV of the lens and contain no image information.

Another essential aspect is the signal generator that will control the scanning range and velocity of the dual-axis galvo. At this moment, as already mentioned, only the movement of the X-axis mirror of the galvanometer is performed. This is made by a sawtooth wave function (Fig. 51).

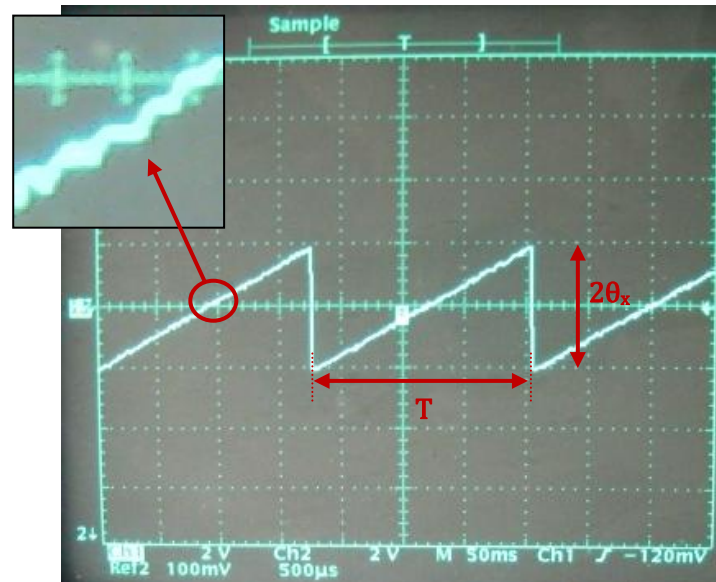


**Fig. 51** - Signal currently used to control the X-axis mirror in 256 steps/points. The optical scan angle is  $\theta_x \pm 2^\circ$  (the scaling factor of control board is  $1 \text{ V}/^\circ$ ) and the oscillatory period of the galvo mirror is  $T \approx 175$  ms.

The transverse position of the beam is made from  $-\theta_x \rightarrow \theta_x$  in a specified number of steps/points ( $N$ ) by incrementing the wave signal  $2\theta_x/N$  Volts (taking into account the

Volts per degree scaling factor of control board). Fig. 51 represents the signal currently used in the project for an optical scan angle (X-axis mirror) of  $\pm 2^\circ$  in 256 steps.

The duty cycle  $\eta$ , defined as the ratio between the active time  $t$  used effectively for the scanning process and the total time  $T$  for the oscillatory period of the galvo mirror, is  $\eta = t/T$ . As it can be seen in Fig. 51, the active time  $t$  (A-scan + T-scan) is about  $\approx 175$  ms, so the duty cycle is very good because  $t \approx T$ . We can also gauge that the active portion  $t$  can be considered linear with a good approximation.

### 3.8. Fiber Optic Circulator

The two single mode fiber optic circulators are of type Thorlabs CIR1064-APC. An optical circulator is a three-port device that allows light to travel in only one direction.

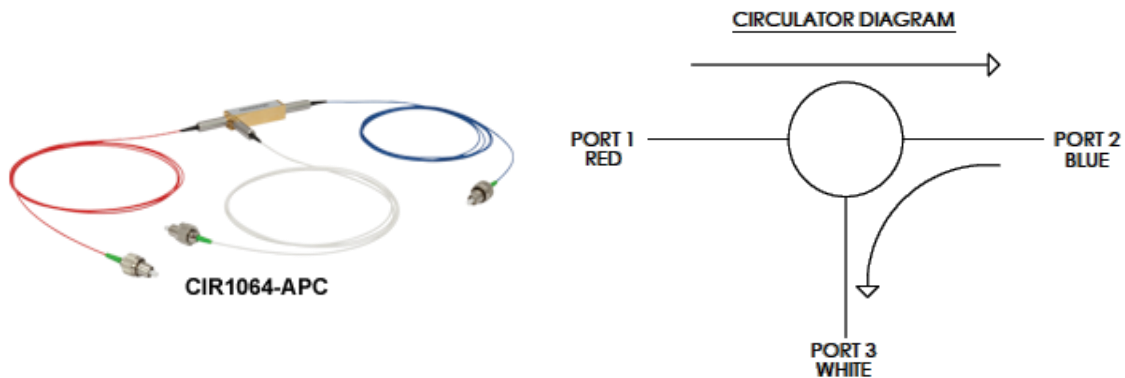


**Fig. 52** - Thorlabs CIR1064-APC fiber optic circulator photo (left) and schematic (right) [54].

A signal entering Port 1 will exit Port 2 with minimal loss, while a signal entering Port 2 will exit Port 3 with minimal loss. Light entering Port 2 experiences a large amount of loss at Port 1, and light entering Port 3 experiences a large amount of loss at Ports 2 and 1 (Fig. 52). Its main optical characteristics are: maximum optical power of 300 mW; wavelength range 1050-1070 nm; insertion loss as a maximum of 2.1 dB ( $\approx 0.8$  %); directivity linking port  $\geq 45$  dB and return loss between ports of  $\geq 50$  dB [54].

Note that this optical circulator is a non-reciprocal device (any changes in the properties of the light caused by passing through the device are not reversed by traveling in the opposite direction) and has very small changes in the polarization of light [54].

### 3.9. Fiber Optical Coupler

The experimental setup used two 2×2 single mode fused fiber couplers (Fig. 53) with center wavelengths  $1064 \pm 15$  nm. One with 50:50 split ratio (Thorlabs FC1064-50B-APC) and the other one with 90:10 split ratio (Thorlabs FC1064-90B-APC). Both have a directivity >55 dB [54].

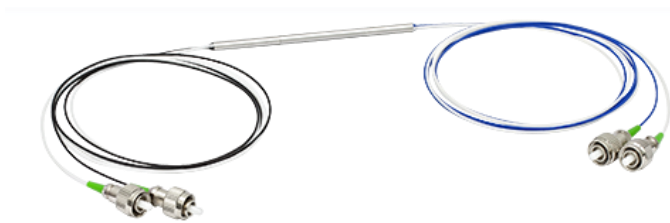


**Fig. 53** - Photo of a bidirectional 2x2 single mode fused fiber coupler [54].

These couplers are bidirectional, allowing any one of the ports to be used as an input port. To understand its operating process, a 90:10 2×2 fiber coupler is shown schematically in Fig. 54. Since the coupler is bidirectional, either end of the coupler may be used as the input (i.e., either end A or end B). Any of the four fibers may be used as a single input. On the other end of the coupler, one fiber will have 10% of the input signal, while the other fiber will have 90% of the signal. The same analysis can be made for the fiber coupler with 50:50 split ratio.

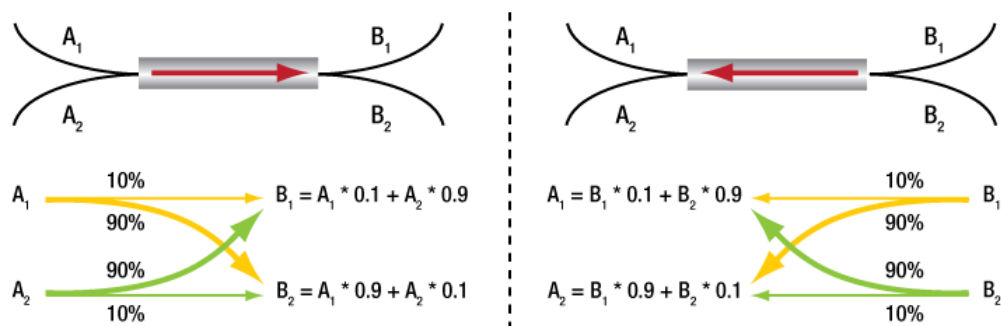


**Fig. 54** - Schematic of a bidirectional 90:10 2x2 single mode fused fiber coupler [54].

The insertion loss (Coupling Ratio + Excess Loss) is 3.1-3.5/3.1-3.5 dB (50:50) and 9.5-10.5/0.4-0.7 dB (90:10) [54].

### 3.10. Variable Fiber Optical Attenuator

For balancing the optical signal in the inputs of the balance detector, it is used, in the reference path, a single mode variable fiber optical attenuator Thorlabs VOA1064-APC (Fig. 55).

The attenuator has a lens for collimating the light from the input fiber. A blocking device can be manually adjusted by a screw. Then, a second lens is used to couple light into the output fiber. Thus, the coupling efficiency is changed until the desired attenuation is obtained. The maximum specified attenuation is achieved within 10 turns counter clockwise. In the first six and a half turns, the attenuation increases almost linearly. Then the attenuation increases abruptly to its maximum value [54].

The relevant attenuator specifications are: maximum optical power of 300 mW; wavelength range 1044-1084 nm; attenuation range 1.3-50 dB and attenuation resolution about 0.15 dB [54].

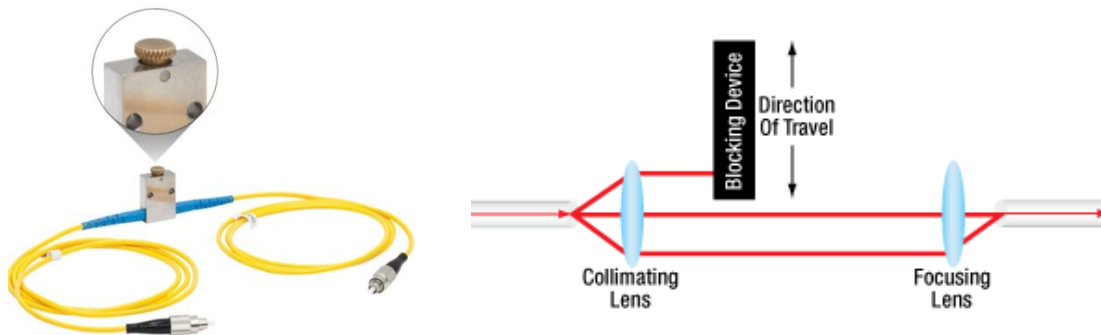
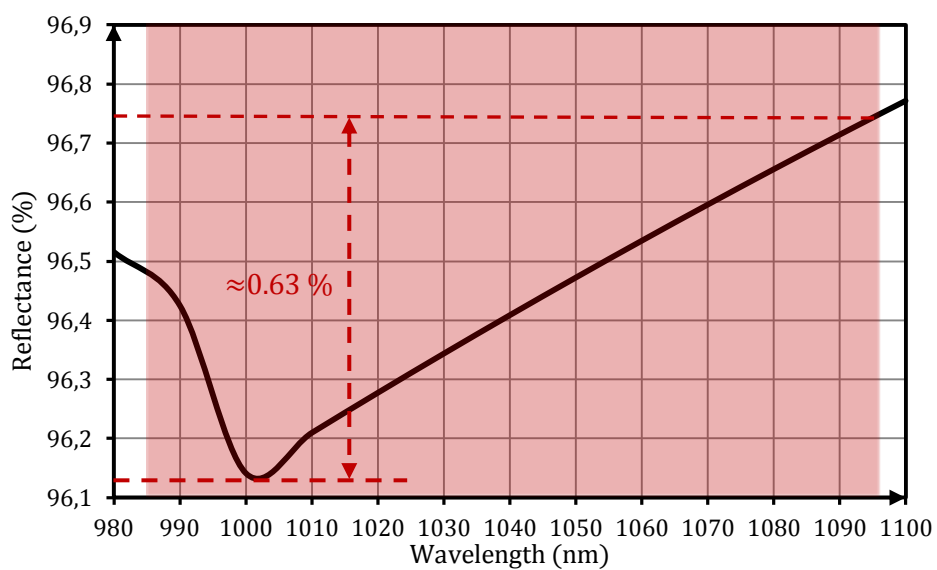


Fig. 55 - Thorlabs VOA1064-APC variable fiber optical attenuator photo (left) and schematic (right) [54].

### 3.11. Gold Mirror

One of the main points to yield a good SNR value and in turn the best possible sensitivity for OCT imaging is the optical power of light that returns from the reference arm. Therefore, it is important to choose an efficient reflective coating over the entire wavelength range used. The selected reference arm is a Thorlabs PF10-03-M01 round

mirror with a protected gold coating because it provides  $>96\%$  average reflection from 985 nm to 1095 nm (Fig. 56) [54].



**Fig. 56** – Reflectance of the gold mirror Thorlabs PF10-03-M01 as a function of the wavelength. Adapted from [54].

Note that a proprietary protective overcoat is layered over the gold to help protect it from damage and make cleaning easier.



# Chapter 4

## System Control and Data Acquisition Software

The main purpose of this chapter is to explain the developed software. The program developed is user-customizable and contains the basic components for system control, data acquisition, processing, file management, and 2D image reconstruction. The software provides flexible control of the data acquisition, A-scan range and 2D image size.

The OCT data may be displayed in real-time raw data, FFT (fast Fourier transform) or 2D image. The software allows recording the data and image into disk files (image data file can be saved into standard image files or into data).

## 4.1. Software Development Tools

The program was developed in Microsoft Visual Studio 2008 Edition (Visual C++/CLI) for 64-bits over a Microsoft Windows 7 operation system 64-bit. One of the main reasons for this choice is due to the fact that the manufacturer of the data acquisition (Innovative Integration) and the digital to analog boards (National Instruments) already provides a software pack for host development in C++ that includes all the necessary libraries to manage the boards. Another reason is because C++ is the high-level programming language that takes best advantage of the hardware, making the program more efficient.

The software development tool available from the Innovative Integration requires an Intel-brand processor CPU (central processing unit) for proper operation because the computer processor must be compatible with the Intel MMX (Matrix Math eXtension) and SIMD (Single Instruction, Multiple Data) instruction-set extensions which the host data acquisition board libraries utilizes extensively to improve processing performance within a number of its components. So the personal computer used is based in an Intel Core i7 CPU.

The code that interacts with the Innovative Integration library (referred to as Malibu) is separated out into a class named **ApplicationIO** in the files ApplicationIO.cpp and ApplicationIO.h. Therefore, to allow access to this class, it was created an **ApplicationIO** object in the main form of the application. In this way, the user interface (UI) can call the methods of the **ApplicationIO**. Sometimes, however, the **ApplicationIO** object needs to call back into the UI.

```
Main.h
private:
    IUserInterface *UI; // For access de Main functions from the classe
                        ApplicationIO
    ApplicationIO *Io; // For access de ApplicationIO function from
                       the classe Main
```

But since this code is common to different programming environments, it cannot use a pointer to the main form. The solution to decouple the **ApplicationIO** from the main form was to use an **IUserInterface** class to hide the implementation. This class is an



abstract class that defines a set of methods that can be called by a client class (here, **ApplicationIO**). The **ApplicationIO** class produces an implementation of the **IUserInterface** by multiple inheriting from the interface and this way the implementing class forwards the call to the UI form class to perform the action. **ApplicationIO** only has to know how to deal with a pointer to a class that implements the interface, and all UI dependencies are hidden.

The predefined **IUserInterface** class is defined in **ApplicationIO.h**. The constructor of **ApplicationIO** requires a pointer to the interface, which is saved and used to perform the actual updates to the UI inside of **ApplicationIO**'s methods.

```
ApplicationIO.h

class IUserInterface {
public:
    // Ctor & Dtor
    virtual ~IUserInterface() { }

    ...
};

class ApplicationIO {
public:
    // Ctor & Dtor
    ApplicationIO(IUserInterface *ui);
    ~ApplicationIO();

    ...
};
```

In the Malibu, objects are defined to represent units of hardware as well as software units. For example, the **X5\_400M** object represents the board, the **PacketStream** object encapsulates supported board-specific operations related to I/O streaming and the **Buffer** class object is used to access buffer contents.

Note that the personal computer is provided with a graphics processing unit (GPU) from NVIDIA with Compute Unified Device Architecture (CUDA) technology. This equipment can be used in future works to improve the program's performance.

## 4.2. Main Window

The following figure (Fig. 57) shows the main window of the OCTSystem program that was developed. It shows the layout of the controls of the UI. This application has four flow control buttons on the left bottom (**Open**, **Close**, **Start** and **Stop**), two setup tabs for the configuration of the OCT parameters, three display data buttons on the left top (**Signal**, **FFT** and **Image**), a common area, which displays messages and feedback throughout the operation of the program, and a status strip to display the flow data rate and temperature of the acquisition board.

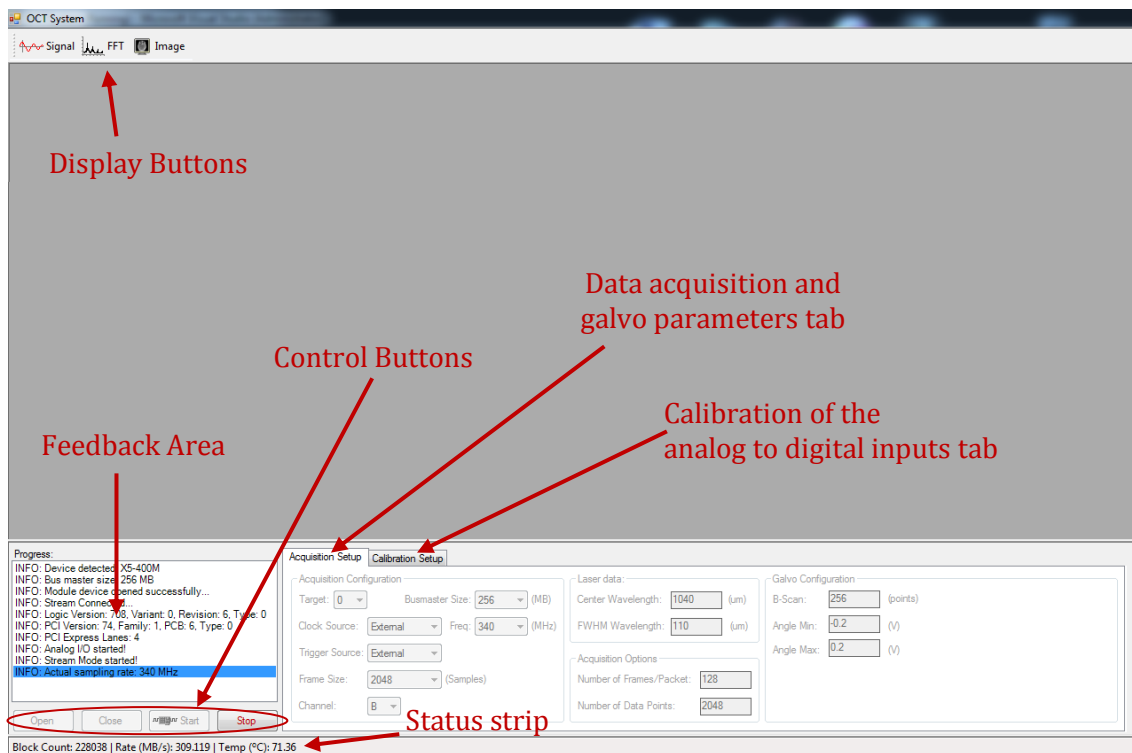


Fig. 57 – Main window of the OCTSystem program.

The common area has three types of messages: **INFO** (reports, to the user, relevant information – color font black); **ALERT** (prompts the user that there is a situation that could compromise the proper functioning of the system – color font orange) and **ERROR** (situation that does not allow the program to work – color font red).

Each tab has its own significance and usage. The acquisition setup tab has several sections that allow the user to customize the main parameters of the data acquisition,

laser properties and galvo control. The calibration setup tab enables, if needed, to read or write the data acquisition on-board EEPROM information associated with calibration of the analog to digital inputs.

### 4.3. Opening and Initializing the Boards

As soon as the application is launched, it checks if the boards are installed correctly. If not, a message of error is displayed in the common area and the program disables all the controls in the user interface.

```
Main.h

// Verify if the data aquisition board is present
if (!BoardDetected) {
    LogProgress("ERROR: No devices detected!");
}
else {
    LogProgress("INFO: Device detected: " + Io->ModuleNameStr());
    SetSettings(); // Load options (file INI -> controls)
}
```

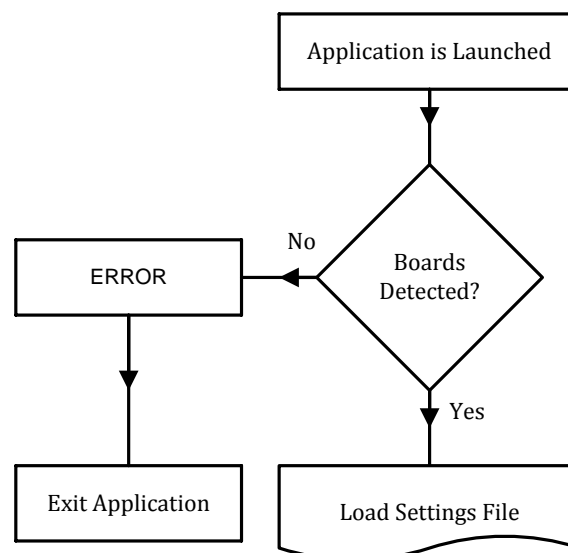


**Fig. 58** - Flowchart of detection the boards.

In this case, the user should solve the problem and restart the program. If the hardware is properly installed, the user is informed in the common area, the settings file is

loaded, and the data is passed to the controls in the data acquisition and galvo parameters tab (Fig. 58). Some of these settings in the tab are then delivered to the boards, for configuring accordingly, when the **Open** button is chosen. The others are only used when the **Start** button is pressed. In the first case, the parameters are **Target**, **Busmaster Size** and the galvo **Angle Min**.

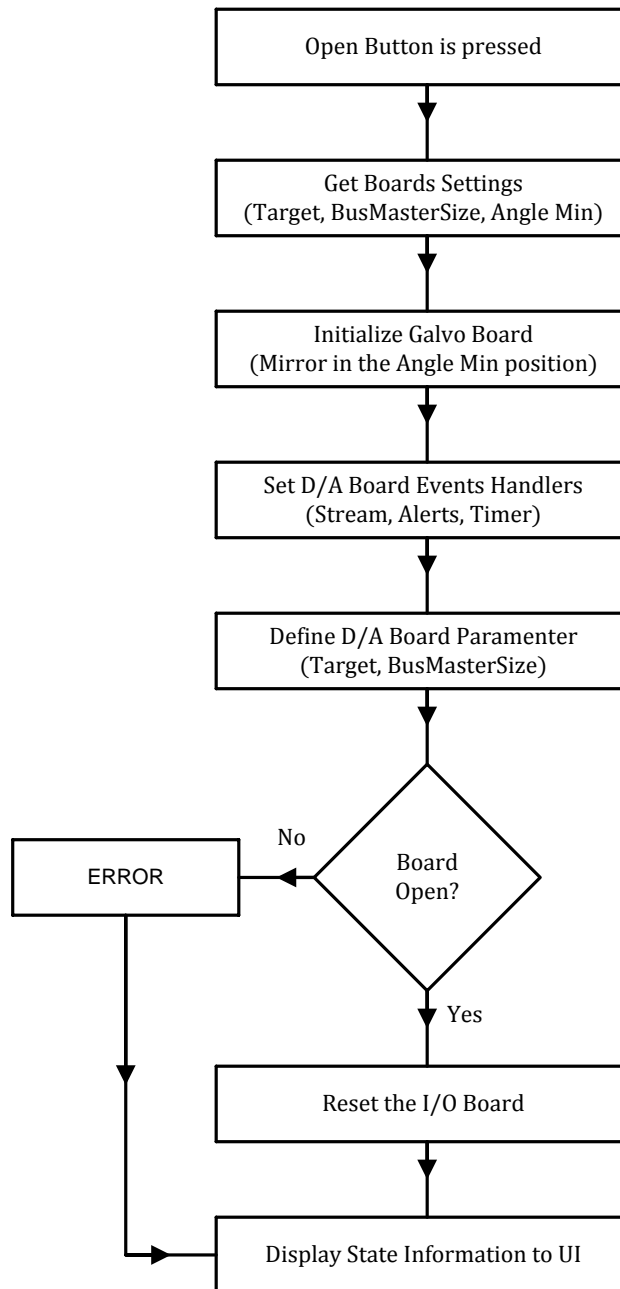


Fig. 59 - Flowchart of opening and initializing the boards.

The **Target** combo box allows the selection of the device from those present in the system. All Innovative Integration devices of any type share a sequence of target number identifiers. The first board found is target 0, the second target 1, and so on. The order of

the targets is determined by the location in the PCI bus, so they will remain unchanged from run to run unless the board is moved to a different slot or another target is installed.

```
ApplicationIO.cpp

// Define the board selected
Module().Target(Settings.Target);
```

The Innovative PCI-based DSP baseboard requires, for optimum performance, at least, 64 MB of reserve memory for each Innovative board used [51]. This value depends on the rates of bus-master transfer traffic which the baseboard will generate. Therefore, for this OCT setup, when operating at full speed, the transfer rates slightly exceed 256 MB/sec. Consequently, and for this case, to ensure gap-free data acquisition, additional memory should be reserved to a maximum of 256 MB on the **Busmaster Size** combo box. So, this parameter will allow the user to set the memory size needed for the busmastering to occur properly and it should always be taken before opening the board.

Note that this value must always be multiple of 4 MB (the possible values are displayed automatically by the program) and larger values allow more overlap between the board and application, at the cost of slower allocation at startup time.

```
ApplicationIO.cpp

// Insure BusMasterSize is a multiple of 4 MB
const int Mega = 1024 * 1024;
const int BMSize = max(Settings.BusMasterSize/4, 1) * 4;

// Define the Incoming BMSize in bytes
Module().IncomingBusMasterSize(BMSize * Mega);
```

The **Angle Min** text box defines the initial position of the X-Axis mirror from the 2D galvo system.

Once these values are defined, the **Open** button can then be selected to open and initialize the data acquisition board and the galvo position. Thus, the first thing it will do is to link Malibu software events to callback functions in the applications by setting the handler functions. Malibu has a method where functions can be plugged into the library to be called at certain times or in response to certain events detected. These events are informational messages issued by the logic loader feature of the module and can be divided into different types.

One is Stream events: `HandleBeforeStreamStart`, `HandleAfterStreamStart` and `HandleAfterStreamStop` handle events issued on before stream start, after stream start

and after stream stop, respectively. These handlers are designed to perform multiple tasks as events occur. These events are tagged as synchronized, so Malibu will marshal the execution of the handlers for these events into the main thread context, allowing the handlers to perform user-interface operations.

```
ApplicationIO.cpp

// Configure module before and after stream event handlers
Module().OnBeforeStreamStart.SetEvent(this,
    &ApplicationIO::HandleBeforeStreamStart);
Module().OnBeforeStreamStart.Synchronize();
```

Other types of events are the Alerts processing handlers, which are packets that the module generates and sends to the host as packets containing out-of-band information concerning the state of the module. For instance, if the analog inputs were subjected to an input over-range, an alert packet would be sent to the host and interspersed into the data stream, indicating the condition. This information can be acted upon immediately, or simply logged along with analog data for subsequent post-analysis.

```
ApplicationIO.cpp

// Configure module alerts event handlers
Module().Alerts().OnTimeStampRolloverAlert.SetEvent(this,
    &ApplicationIO::HandleTimeStampRolloverAlert);
```

The **Stream** object manages communication between the application and a piece of hardware. Separating the I/O into a separate class, it clarifies the distinction between an I/O protocol and the implementing hardware.

In Malibu, one of the events of the **PacketStream** class is used to alert us when a packet arrives from the target. When a data packet is delivered by the data streaming system, OnDataAvailable event will be issued to process the incoming data. This event is set to be handled by HandleDataAvailable. After processing, the data will be discarded unless saved in the handler.

```
ApplicationIO.cpp

// Configure alert when a packet arrives from the target
Stream.OnDataAvailable.SetEvent(this,
    &ApplicationIO::HandleDataAvailable);
```

In this program, a Malibu **Timer** object from a **SoftwareTimer** class has been added to the **ApplicationIO** class to provide periodic status updates to the user interface.

```
ApplicationIO.cpp
// Configure timer event handlers
Timer.OnElapsed.SetEvent(this, &ApplicationIO::HandleTimer);
Timer.OnElapsed.Thunk(); // Synchronize
```

Next, the parameters **Target** and **Busmaster Size** are defined and the `Open()` method of the baseboard tries to activate the board and allocates internal resources for use. If everything is correct, then the `Reset()` method is called, performing a board reset to put the board into a known good state. Note that reset will stop all data streaming through the busmaster interface and it should be called only when data taking has been halted.

Once the object is attached to the current physical device, the streaming controller associates it with a baseboard by the `ConnectTo()` method. Once connected, the object is able to call into the baseboard for board-specific operations.

```
ApplicationIO.cpp
// Connect Stream to a Packet Based Streaming device
Stream.ConnectTo(&(Module.Ref()));
```

Similarly, the `Close()` method, that is called from the **Close** button, closes the communications to the hardware. Inside this method, first we logically detach the streaming subsystem from its associated baseboard using `Disconnect()` method. Malibu method `Close()` is then used to detach the module from the hardware and release its resources.

```
ApplicationIO.cpp
void ApplicationIO::Close() {
    Stream.Disconnect();
    Module().Close();
    UI->LogProgress("INFO: Stream Disconnected...");
}
```

Note that, to change targets, one must click the **Close** button first to close the driver, then select the number of the desired target using the **Target #** combo box, and then click **Open** to open communications with the new target module.

During all these procedures (**Open** and **Close** the boards), the program captures and displays state information to the feedback area.

## 4.4. Configuration of the Data Streaming

After a successful recognition of the boards, all necessary settings related to data acquisition should be configured. This can be made on the data acquisition and galvo parameters tab that holds a set of controls for this purpose.

At this point of the process, the fields that the user has set for a proper data acquisition are: **Clock Source**, data acquisition **Frequency**, **Trigger Source**, **Frame Size**, **Channel**, **Number of Frames/Packet** and **Zero Padding after** (Fig. 60).

Fig. 60 - Data acquisition setup tab.

The clock for the data acquisition board can come from an External (0) clock or from an Internal (1) crystal. The selection can be made at the **Clock Source** control. If the clock source selected is Internal, the clock rate is specified in the **Frequency** field in MHz (minimum 20 MHz and maximum 400 MHz). In our case, since the signal clock is set by the laser, the best choice is External. In this case, the **Frequency** control is meaningless and therefore is automatically put in disabled state.

```
ApplicationIO.cpp
// Route clock to active analog devices
X5ClockIntf::IIClockSource src[] = { X5ClockIntf::csExternal,
    X5ClockIntf::csInternal };
Module().Clock().Source(src[Settings.ClockSource]);
```



The **Trigger Source** selection box controls the way that data streaming is started (samples will not be acquired until the input channel is triggered). It can be started by an External (value 1) input signal (for the same reasons of the clock source) or by the software (Internal (value 0)). This data acquisition board supports both framed and continuous triggering. In framed mode, each trigger event, whether external or software initiated, results in the acquisition of a fixed number of samples. In continuous mode, data flow continues whenever the trigger is active, and it pauses while the trigger is inactive [51].

```
ApplicationIO.cpp

// Active External Trigger if selected
Module().Input().ExternalTrigger( (Settings.TriggerSource == 1) );
```

In this OCT setup, the selection mode used is the framed trigger mode (a single trigger enables many data samples to be taken before rechecking the trigger). In this mode, the trigger goes false once the programmed number of **Frame Size** points (16 bits each) have been collected. Start triggers that occur during this time are ignored. The **Frame Size** must be a power of two and a value between a maximum of 16777216 and a minimum of 256. Due to these characteristics and the laser used (1376 points in the k-space), the power of two value of 2048 points is the most appropriate to the **Frame Size**. The data is stored in the data acquisition board memory until reaching a number of points equal to **Frame Size** × **Number Frame/Packet**. When this value is reached, the data is transferred to the host program. Note that the samples are captured when the sample clock and the trigger are true. The trigger is true after a rising edge on the trigger input, until a falling edge is found. The trigger is timed against the sample clock and may have a 0 to +1 A/D conversion clock uncertainty for an asynchronous trigger input [51].

```
ApplicationIO.cpp

// Granularity of 256 is firmware limitation
int framesize = Module().Input().Info().SamplesPerFrame();

if (Settings.AnalogInFrameSize % framesize) {
    std::stringstream msg;
    msg << "ERROR: Frame count must be a multiple of " << framesize;
    UI->LogProgress(msg.str());
    return false;
}
...
// Frame count in units of packet elements
Module().Input().Framed(Settings.AnalogInFrameSize);
```

Data flow from the A/D device into the A/D interface component in the FPGA is controlled by the triggering (Fig. 61). The data is then error corrected and the enabled channel flows to the data buffer, which implements a data queue in the SRAM. The packetizer pulls data from the queue, creates data packet of the programmed size, sends those to the PCIe interface logic, and then into host memory for consumption by the host program [51].

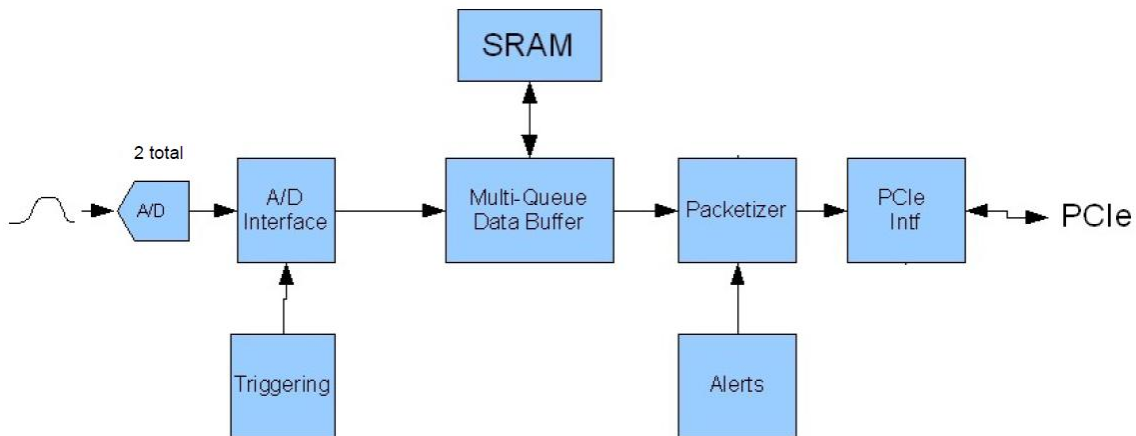


Fig. 61 - X5-400M Framework Logic Data Flow [51].

The selected packet size (**Number Frame/Packet**) must be integer and sub-multiples of the frame size, to allow the entire data set to flow to the host. That way, the entire data frame can be moved immediately to the host without waiting for the next trigger frame.

Because the value of the SRAM of the board is 512 MB, the **Frame Size × Number Frame/Packet** should be less than or equal to 16777216.

The field **Zero Padding after** puts to zero data points received after this value and should always be less than or equal to **Frame Size**.

All these conditions are verified by the program before the start of data acquisition, alerting the user if they are not compliant.

Note that, since only one input channel is used, the packet size sent to the program host is half the one that was defined. This happens because each packet value has a dimension of 32 bits (including two data values of 16 bits each).

```

ApplicationIO.cpp

Settings.AnalogInPacketSize = Settings.FramesByPacket *
                             Settings.AnalogInFrameSize;

// Avoid residual data in pipeline between frames
int s1 = max(Settings.AnalogInFrameSize,
             Settings.AnalogInPacketSize);
int s2 = min(Settings.AnalogInFrameSize,
             Settings.AnalogInPacketSize);
if (s1 % s2) {
    UI->LogProgress("ERROR: Packet & frame sizes should be integer
                  multiples!");
    return false;
}
...
// Packets scaled in units of events (samples per each enabled
channel)
int ActiveChannels =
    Module().Input().Info().Channels().ActiveChannels();
int SamplesPerWord = 4 /
    Module().Input().Info().Channels().BytesPerSample();
Module().Input().PacketSize(Settings.AnalogInPacketSize *
                             ActiveChannels / SamplesPerWord + 2);

```

In the **Channel** control, we can specify the input channel where the data will flow (Channel A – input 1 or B – input 2).

```

ApplicationIO.cpp

// Channel Enables
Module().Input().Info().Channels().DisableAll();
Module().Input().Info().Channels().Enabled(Settings.AnalogInChannel,
                                           true);

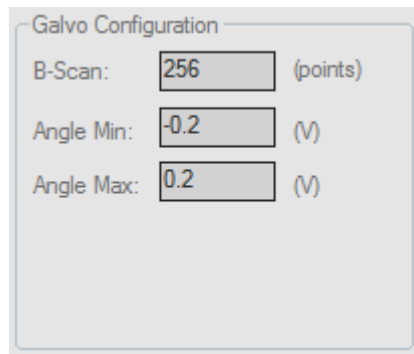
```

## 4.5. Controlling the Galvanometer

At this point of the project, the program only controls the transversal motion of the laser beam. So, accomplishing A-scan together with transverse scans (T-scan), the program is already capable of building B-scan images. The T-scans are achieved via rotation of the X-axis mirror of the galvanometer, keeping the Y-axis mirror stationary.

The sawtooth wave functions that will position the galvanometer are generated with the aid of PCI-6010 board (National Instruments Corporation).

The configuration of all necessary settings related to the T-scan movement can be made on the section galvo configuration of the data acquisition setup tab. The fields that the user has set for a proper T-scan are: **B-scan**, **Angle Min** and **Angle Max** (Fig. 62).



The image shows a dialog box titled "Galvo Configuration". It contains three input fields with their respective units:

- B-Scan: 256 (points)
- Angle Min: -0.2 (V)
- Angle Max: 0.2 (V)

**Fig. 62** – Settings of the X-axis mirror of the galvanometer to execute a T-scan.

The transverse position of the beam is made from **Angle Min** (-U Volts) to **Angle Max** (U volts) Volts in a specified number of equally steps/points (**B-scan**). This is accomplished by incrementing (**B-scan - 1** times) the wave signal amplitude in  $2U/B\text{-scan}$  Volts.

The user should take into account the Volts per degree scaling factor of control board (1.0, 0.8 or 0.5) and the gain of the non-inverter amplifier adapter (between the output D/A of the PCI-6010 board and the input of the galvo driver).

```
Main.cpp

void Main::MoveGalvoHoriz() {
    GalvoPosition = GalvoPosition + (Io->Settings.DACMax - Io->
        Settings.DACMin) / Io->Settings.BScanPoints;
    GalvoX ^MoveGalvoX = gcnew GalvoX();
    MoveGalvoX->PositionGalvoX(GalvoPosition);

    if ( GalvoPosition >= Io->Settings.DACMax) {
        GalvoPosition = Io->Settings.DACMin;
        GalvoStart = true;
    }
    else {
        GalvoStart = false;
    }

    delete MoveGalvoX;
}
```

As an example, using the parameters of Fig. 62 and assuming Volts/degree scaling factor of 1.0 and a gain of 10, the minimum and the maximum angles of the X-axis mirror are, respectively,  $-2^\circ$  and  $2^\circ$ . Even in this case, the increment angle step is  $0.015625^\circ$ . Considering the assembly of Fig. 49, equation 57 and the magnification of the lens  $M = 5$ , the transversal input beam range on the sample is  $\approx 18$  mm and the 256 with steps/points are regularly spaced by  $\approx 70$   $\mu\text{m}$ .

## 4.6. Start Data Acquisition and Control

The two buttons **Start** and **Stop** in the flow control on the main window start and stop data streaming.

Once the **Start** button is pressed (Fig. 63), the application checks if all parameters are within the possible values. If not, a message of error is displayed in the feedback area and the data streaming does not start. If the parameters are validated, the program attempts to configure the data acquisition board. Once again, if the board does not accept the defined parameters, the data streaming does not start and a message of error is displayed. Finally, if the input parameters pass in all these validations, the Stream Start command applies all the above configuration settings to the module and then enables PCI data flow and galvo control. The software timer is then started as well.

```
ApplicationIO.cpp

// Start Streaming
Stream.Start();
Clock.Start();

UI->LogProgress("INFO: Stream Mode started!");

...

std::stringstream msg;
msg.precision(6);
msg << "INFO: Actual sampling rate: " << ActualSampleRate /1.e6 <<
    " MHz";
UI->LogProgress(msg.str());

Timer.Enabled(true);
```

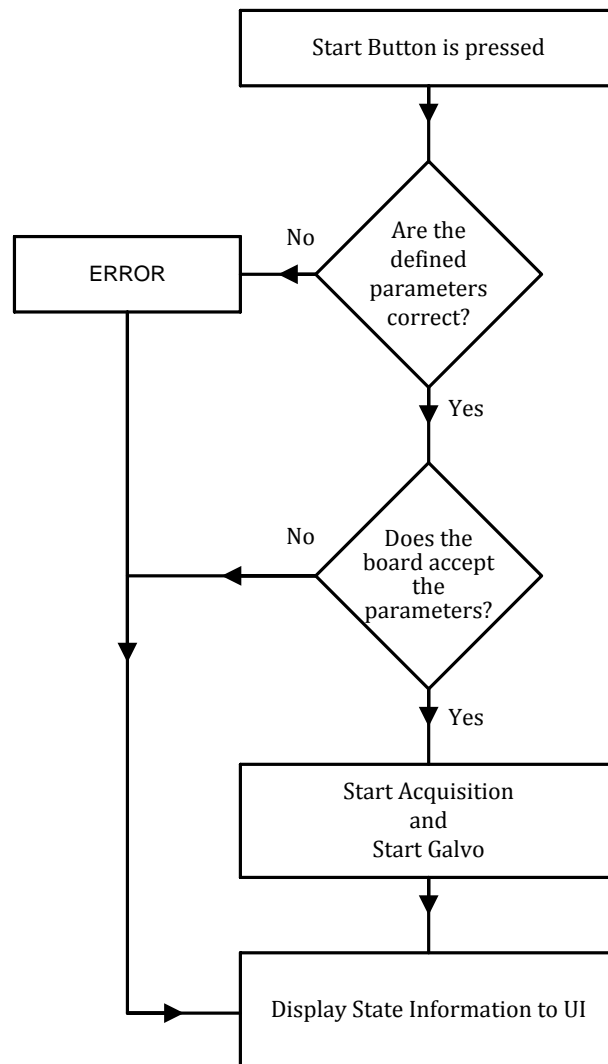


**Fig. 63** - Flowchart of start streaming.

Once streaming is enabled and the module is triggered, data flow will commence. The samples (data packets) will be accumulated into the onboard FIFO and then they are bus-mastered to the Host PC into page-locked driver-allocated memory following a two word header [51]. Upon receipt of a data packet, Malibu signals the `Stream.OnDataAvailable` event. By hooking this event, the application processes each acquired packet and the data buffer is copied from the system bus-master pool into an application buffer.

```

ApplicationIO.cpp

void ApplicationIO::HandleDataAvailable(PacketStreamDataEvent &
                                       Event) {
    Buffer Packet;
    // Extract the packet from the Incoming Queue...
    Event.Sender->Recv(Packet);
    IntegerDG Packet_DG(Packet);
  }

```

The preceding code copies the packet into the local Buffer called Packet. Since data sent from the hardware can be of arbitrary type (integers, floats, or even a mix, depending on the board and the source)[51], Buffer objects have no assumed data type and have no functions to access the data in them. Instead, a second class called a datagram wraps the buffer, providing typed or specialized access to the data in the buffer. IntegerDG provides access to the data in the packet as if it were an array of 32-bit integers. The PacketBufferHeader datagram class provides access to the header of the packet and defines access methods to the fields in the header of a Packet Stream buffer.

The motion of the galvo is much slower than the speed at which the data is acquired. For this reason, the acquisition data rate and the positioning of the galvanometer are controlled by the latter. This control flows in a continuous thread process (Fig. 64) and is implemented with the following code:

```

Main.h

while(1) {
  if (Io->Settings.GalvoX_On == true) {
    if (Io->Settings.Data_Logging == false) {
      if (Io->Settings.Data_AScan == Io->Settings.GalvoX_AScan) {
        Io->Settings.GalvoX_Moving = true;
        Io->Settings.GalvoX_AScan = Io->Settings.GalvoX_AScan + 1;
        if ( Io->Settings.GalvoX_AScan < Io->Settings.BScanPoints ) {
          GalvoPosX = GalvoPosX + (Io->Settings.DACMaxX - Io->
            Settings.DACMinX) / (Io->Settings.BScanPoints - 1);
        }
      }
      else {
        if (_NewImage == false) {
          int DimBuffer = Io->Settings.AnalogInFrameSize / 2 * Io->
            Settings.BScanPoints;
          IppCopyInt32Buffer(&Io->DataPacket[0], &_DataRaw[0],
            DimBuffer);
          _NewImage = true;
        }

        Io->Settings.GalvoX_AScan = 0;
        Io->Settings.Data_AScan = -1;
        GalvoPosX = Io->Settings.DACMinX;
      }

      MoveGalvoX->PositionGalvoX(GalvoPosX);
      Io->Settings.GalvoX_Moving = false;
    }
  }
  threadGalvoX->Sleep(0);
}

```

Shortly after the **Start button** is pressed, the galvo is in its initial position, the data acquisition is started and the galvo is enabled.

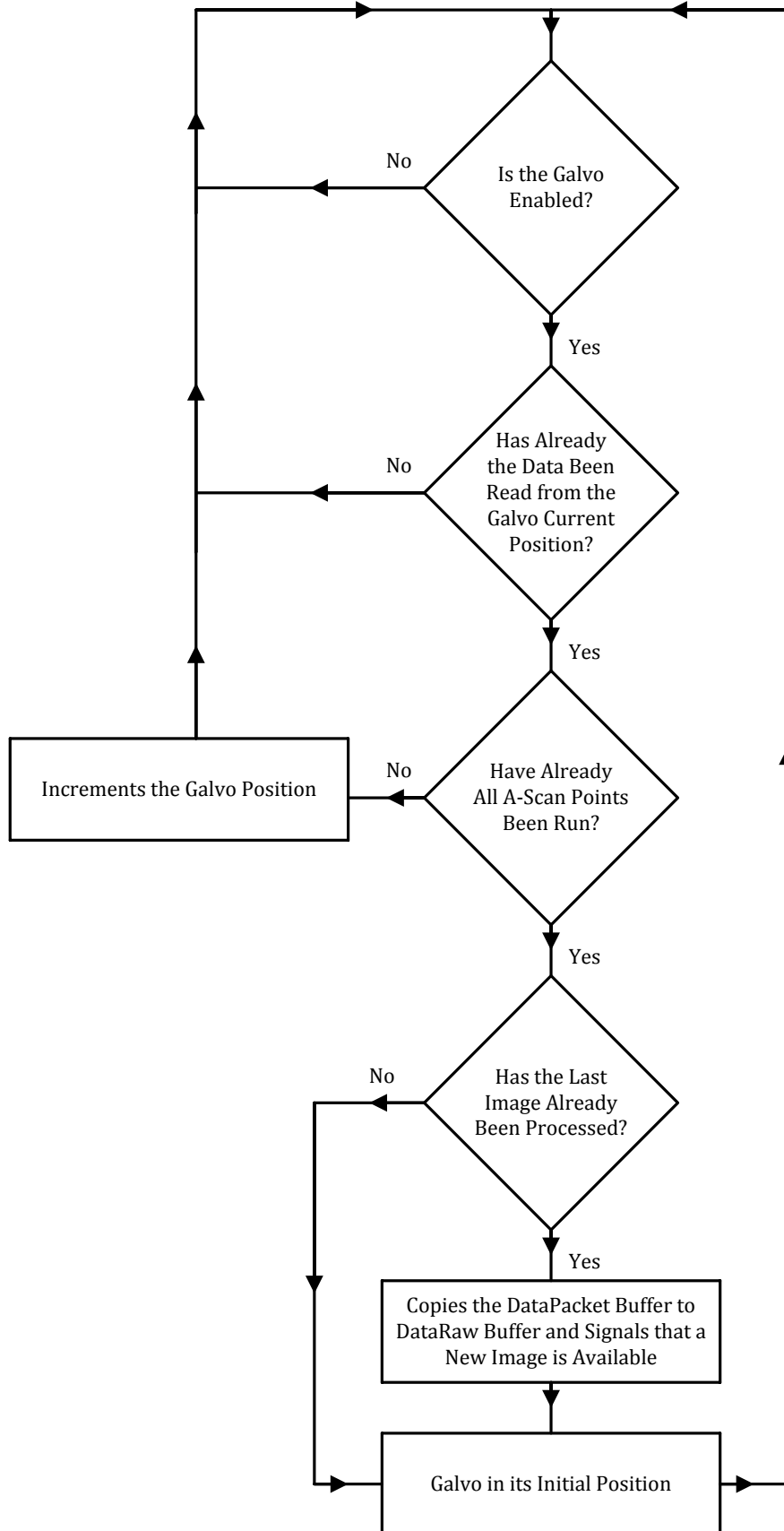


Fig. 64 - Flowchart of data acquisition control and positioning of the galvo.



The galvo thread continuously checks if the reading of the current A-scan position has already been made. If so, then it is incremented to the next position. This procedure is kept until all transversal positions are covered. After that, the B-scan data buffer (DataPacket) is copied to a raw image buffer (DataRow), it is signaled that a new raw image is available to be treated and displayed and a new transversal scan is initialized.

The transferring data between the mentioned buffers avoids overlapping, because it allows the DataPacket buffer to receive the data from the next B-scan while the new image is being processed.

The receipt of a new data packet is continuously triggered by the Stream.OnDataAvailable event. By hooking this event (Fig. 65), the application verifies if the galvo is already on a new position. If not, the first frame of the packet is transferred to the LastDataPacket buffer to be used in the Signal and FFT graphs.

On the other hand, if the galvo is on a new position and the A-scan data of that position has not been read, the frame on the middle of the data packet is copied from the system bus-master pool and added to the application DataPacket buffer.

This event is processed with the following code:

```
ApplicationIO.cpp

if (Settings.GalvoX_On == true) {
    if (Settings.GalvoX_Moving == false) {
        if (Settings.Data_AScan < Settings.GalvoX_AScan) {
            Settings.Data_Logging = true;
            int DimBuffer = Settings.AnalogInFrameSize/2;
            int SrcBufferStart = DimBuffer * Settings.FramesByPacket / 2;
            int DstBufferStart = DimBuffer * Settings.GalvoX_AScan;
            IppCopyInt32Buffer(&Packet_DG[SrcBufferStart],
                              &DataPacket[DstBufferStart], DimBuffer);
            Settings.Data_AScan = Settings.GalvoX_AScan;
            Settings.Data_Logging = false;
        }
    }
    else {
        IppCopyInt32Buffer(&Packet_DG[0], &DataLastPacket[0],
                          Settings.AnalogInFrameSize / 2);
    }
}
```

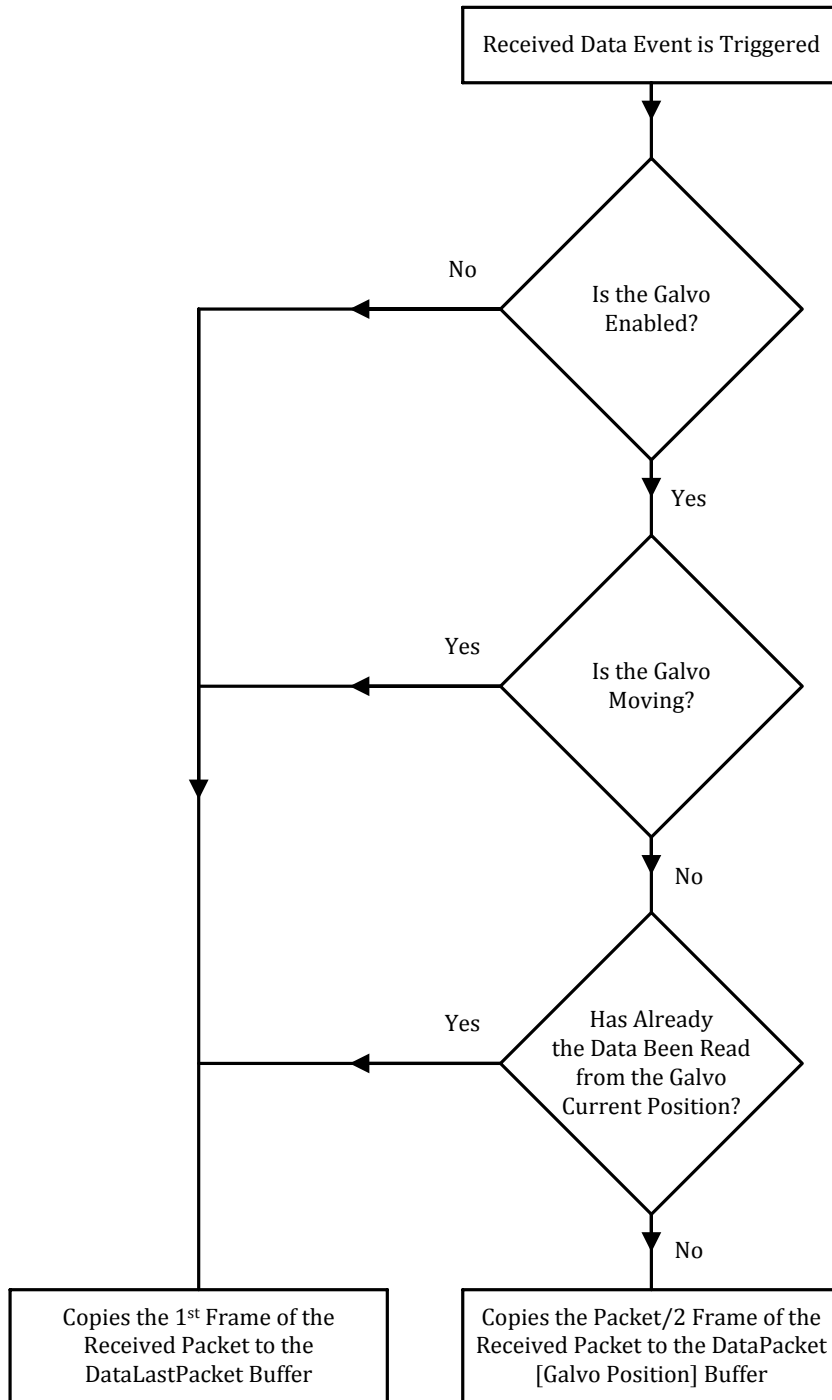


**Fig. 65** - Flowchart of a new data packet receipt.

## 4.7. Signal Processing and Data Display

The acquired data, temporarily stored in memory, can be displayed after processing, separately or simultaneously, in three different ways: **Signal**, **FFT** and **Image** (B-scan). The desired selection can be done through the three buttons on the left top of the main window (Fig. 66).

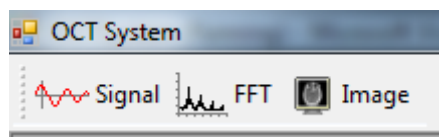


**Fig. 66** - Display Buttons: Signal, FFT and Image.

The **Signal** button opens a new window form (Fig. 67). This form is a thread that processes, every 100 ms (Fig. 68), the acquired data stored in the last DataLastPack buffer and plots the results (amplitude of the interference fringes for an A-scan).

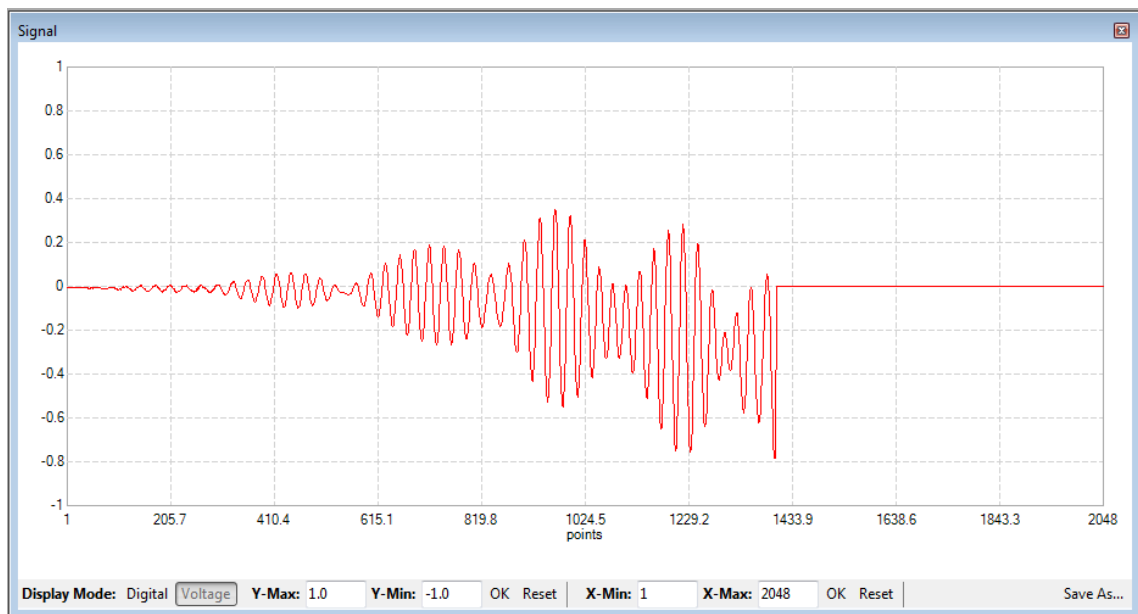


**Fig. 67** - Signal plot window.

This window allows the user to customize the graph and save the data to a text file. The amplitude can be displayed in Voltage (-1 to 1 Volt) or Digital mode (0 to 16383). The minimum and maximum values on both axes can also be modified.

The data packet that is generated from the data acquisition board used has a specific format that depends on the number of channels used. Each sample unit in this packet stream consists of 32-bit words. If the two A/D channels are used, the 16 least significant bits and the 16 most significant bits contain the data from channels 0 and 1, respectively. Since, in this assembly, only one channel is enabled, each sample unit in the packet stream can hold two 16-bit of data (the first in the 16 least significant bits and the second in the 16 most significant bits). Thus, one frame size of N data points consists of N/2 sample units in the packet stream.

Word 0 (32 bits)		Word 0 (32 bits)		...		Word N/2-1 (32 bits)	
D (1)	D (0)	D (3)	D (2)	...	...	D (N/2-1)	D (N/2-2)

Note that, for the data acquisition board used, samples are 14-bits signed extended into a 16-bit field (2 bytes/sample).

The processing of the acquired data, taking into account the above considerations, is made with the following code:

```
frmGraphs.h

// Number of packets acquired NPacket = Frame Size / 2
// 1 Packet = Data1 (16 bits) + Data0 (16 bits)
for (int i = 0; i < NPacket; i++) {
    if ( i < (ZeroPadding / 2) ) {
        // The firsts data value is negative
        if ((DataLastPacket[i] & 0x00002000) != 0) {
            DataInput[2 * i] = DataLastPacket[i] & 0x00001FFF;
        }
        // The first data value is positive
        else {
            DataInput[2 * i] = (DataLastPacket[i] & 0x00001FFF) +
                0x00001FFF;
        }
        // The second data value is negative
        if ((DataLastPacket[i] & 0x20000000) != 0) {
            DataInput[2 * i + 1] = (DataLastPacket[i] & 0x1FFF0000) >> 16;
        }
        // The value data is positive
        else {
            DataInput[2 * i + 1] = ( (DataLastPacket[i] & 0x1FFF0000) >>
                16 ) + 0x00001FFF;
        }
    }
    // Point from which have value = 0 (Zero Padding);
    else {
        DataInput[2 * i] = 0x00001FFF;
        DataInput[2 * i + 1] = 0x00001FFF;
    }
}
}
```

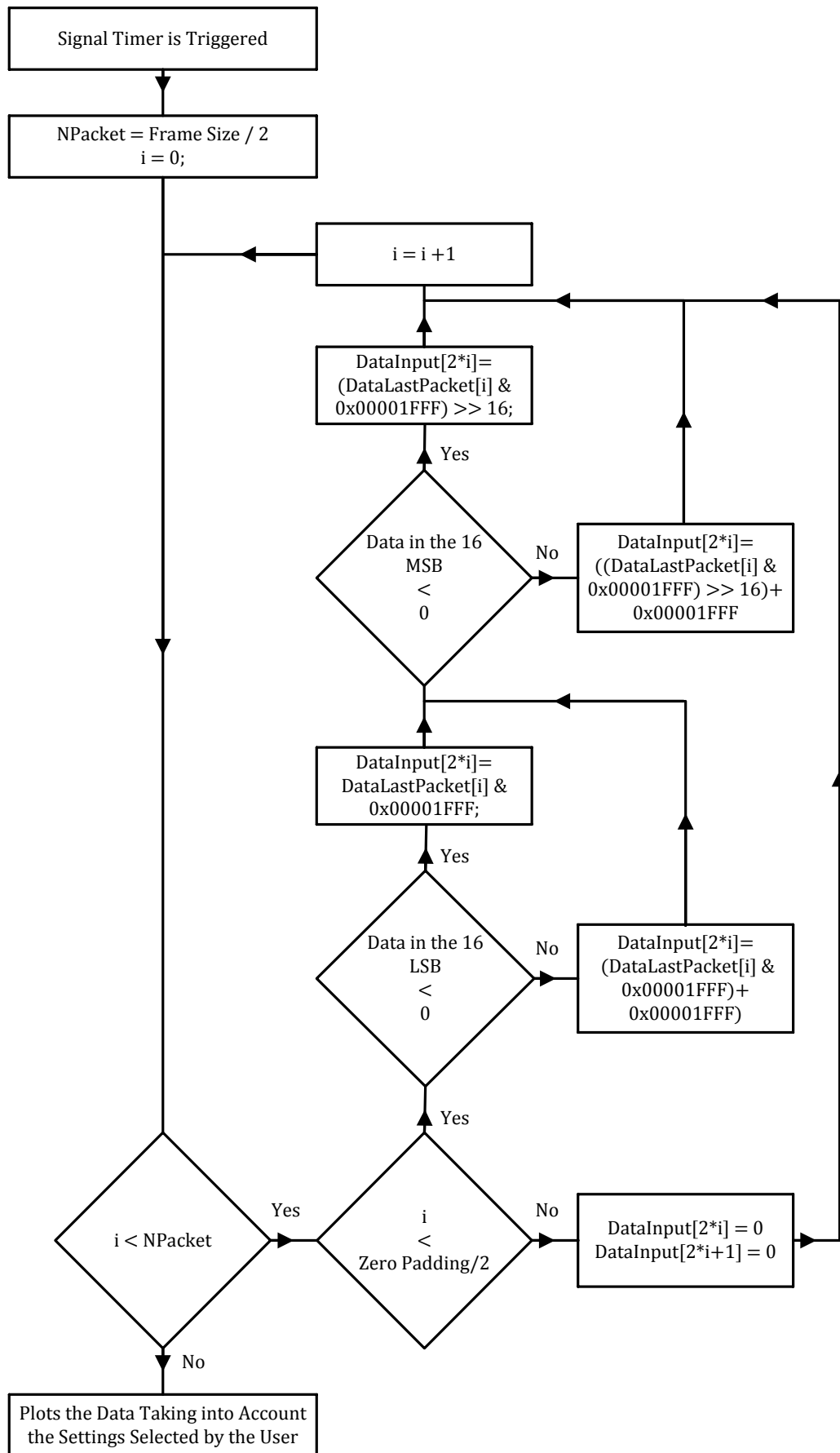


Fig. 68 - Flowchart of processing and plotting a data frame.

The **FFT** button opens a new window form (Fig. 69). This form, such as the **Signal**, is a thread that processes, every 100 ms (Fig. 70), the acquired data stored in the last DataLastPack buffer and plots the results (the fast Fourier transform of the interference fringes for an A-scan data frame).

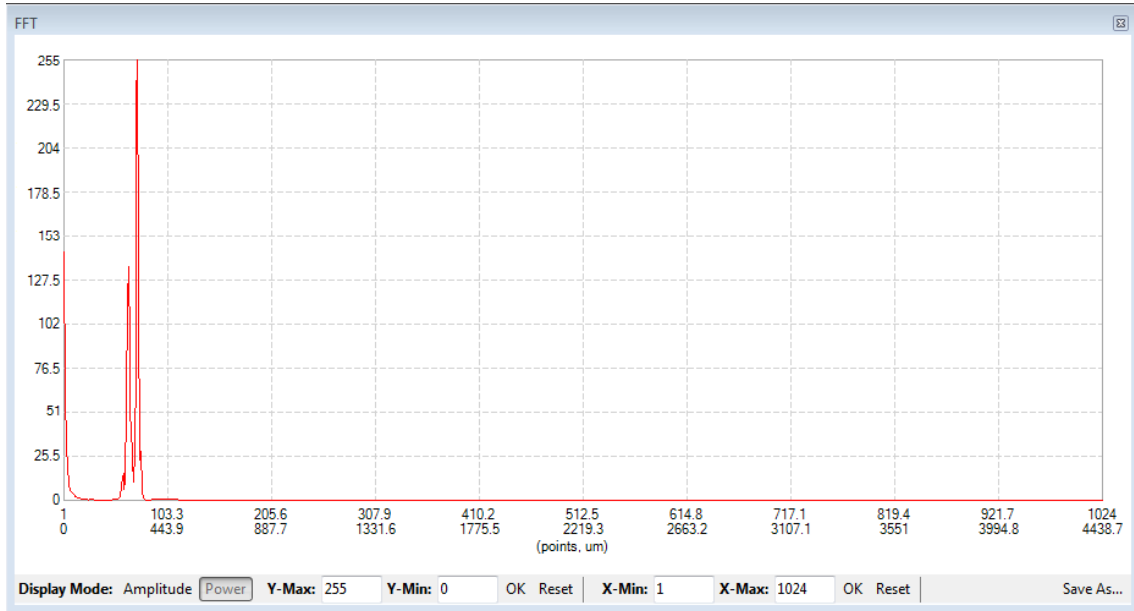


Fig. 69 - FFT plot window.

This window allows the user to customize the FFT and save the data to a text file. The FFT can be display in **Amplitude** or **Power** spectrum. The values in the **Power** spectrum are proportional to the amplitude squared of each distance component making up the k-domain signal. The minimum and maximum values on both axes can also be modified. On the horizontal axis, it is also possible to view the approximate value of depth. The calculation of this value takes into account the axial resolution  $\delta z$  (eq. 50), the characteristics of the laser (**Center Wavelength** and **FWHM Wavelength** fields) defined by the user on the acquisition setup tab (Fig. 60) and considering that the index of refraction of the medium is 1.

All the processing related with the FFT is made with the Fourier class library provided from the software development tool from the Innovative Integration. This class uses a Cooley-Tukey mixed-radix algorithm to calculate the FFT, it allows ignoring the DC component in the spectrum output and enables defining a window to the input data. The window used is a Blackman. This windowing places more emphasis on the bulk of the data in the middle of the sample buffer and less emphasis on data near the beginning and ending edges of the sample buffer.

```

frmFFTs.h

// FFT configuration
Fft->Samples(NPacket * 2);
Fft->Window(Innovative::wtBlackman);
Fft->IgnoreDC(true);

...

// Calculates the FFT
Fft->Transform();

// Zero padding the first 5 FFT elements
for (size_t i = 0; i < 6; ++i) {
    Fft->Spectrum()[i] = 0.0f;
}

// Calculates the maximum value
float AScanMax = Fft->Spectrum().Max();
// Define de normalization factor
float SpectrumNorm = AScanMax / 255;
// proceeds to the FFT normalization
Fft->Spectrum().Normalize(0.0f, SpectrumNorm);

```

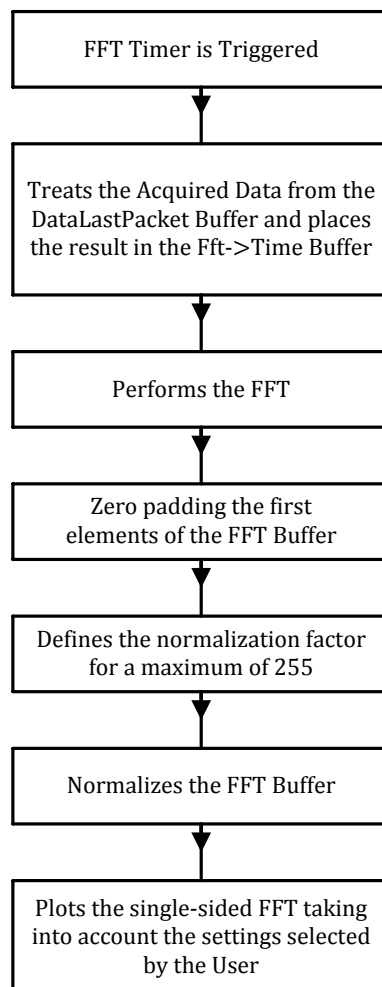


**Fig. 70** Flowchart of processing and plotting the FFT of a data frame.

The **Image** button opens a new window form (Fig. 71). This form is a thread that is invoked when a new B-scan raw image (DataRow buffer) is available to be treated and displayed. The received raw image buffer is first treated and saved in the DataSignal buffer, then the FFT of the individuals A-scan are calculated and normalized (DataFFT buffer), and finally the image is formed (DataImage buffer) and displayed. The user may also save the image into a file.

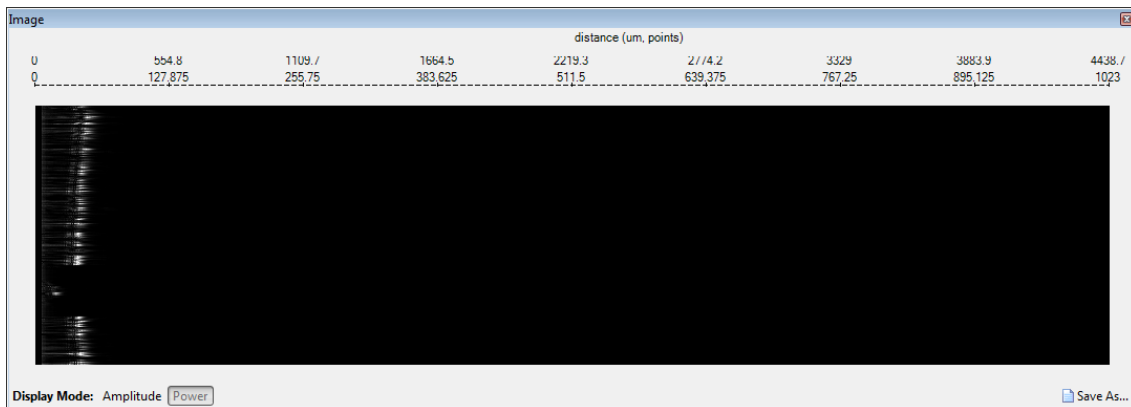
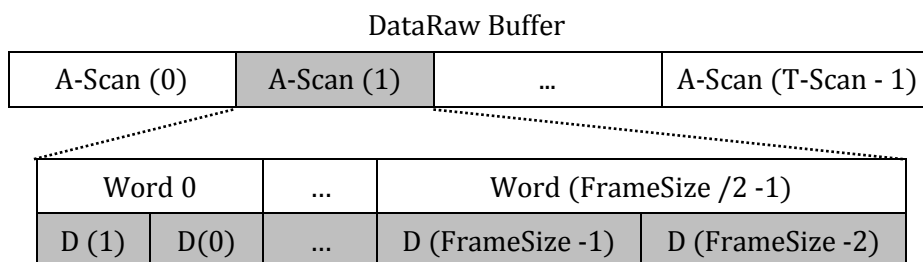


**Fig. 71** – B-Scan Image window.

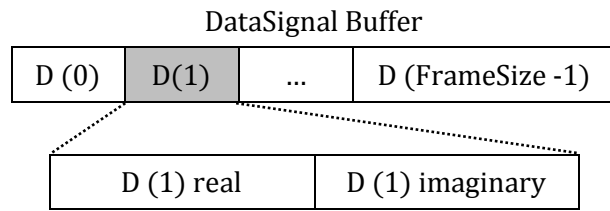
```
frmFFTs.h
// Treat the raw data
Reorder_Data(_DataRow);
// Process the FFT
Process_FFT();
// Construct the image array
Construct_Image();
// Display the image
OCTImage_Paint();
```

The DataRow buffer is a one-dimensional array that contains the individual A-scan of all T-Scan points acquired. Its size is equal to **Frame Size × T-Scan points**. In turns all the individual A-Scan that comes from the data acquisition board has a size of **Frame Size/2** data (32 bits each) and needs to be extracted, processed and reordered.





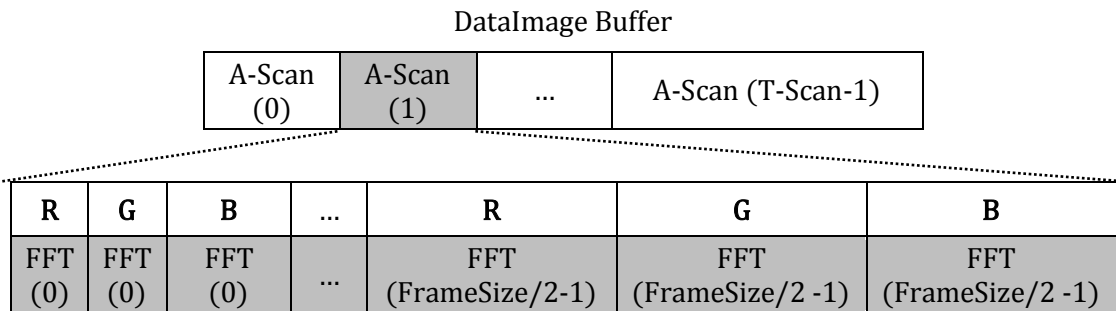
After the initial treatment of the above buffer, a new one-dimensional buffer is formed (DataSignal buffer). This new complex data buffer prepares the data to the FFT.



The single-sided results of the FFT are then normalized and saved on the one-dimensional DataFFT buffer. This new buffer is half the size of the DataSignal buffer.



After this, the one-dimensional DataImage is built. As we are building an image in shades of gray, one pixel of this image will have to take the same value for Red, Green and Blue.



The image is formed line by line taking into consideration the number of the positions of the galvo (T-Scan points) and the depth of each A-Scan.

T-Scan	A-Scan						
0	FFT (0)	FFT (0)	FFT (0)	...	FFT (FrameSize/2-1)	FFT (FrameSize/2 -1)	FFT (FrameSize/2 -1)
...	...	...	...	...	...	...	...
N.º points - 1	FFT (0)	FFT (0)	FFT (0)	...	FFT (FrameSize/2-1)	FFT (FrameSize/2 -1)	FFT (FrameSize/2 -1)

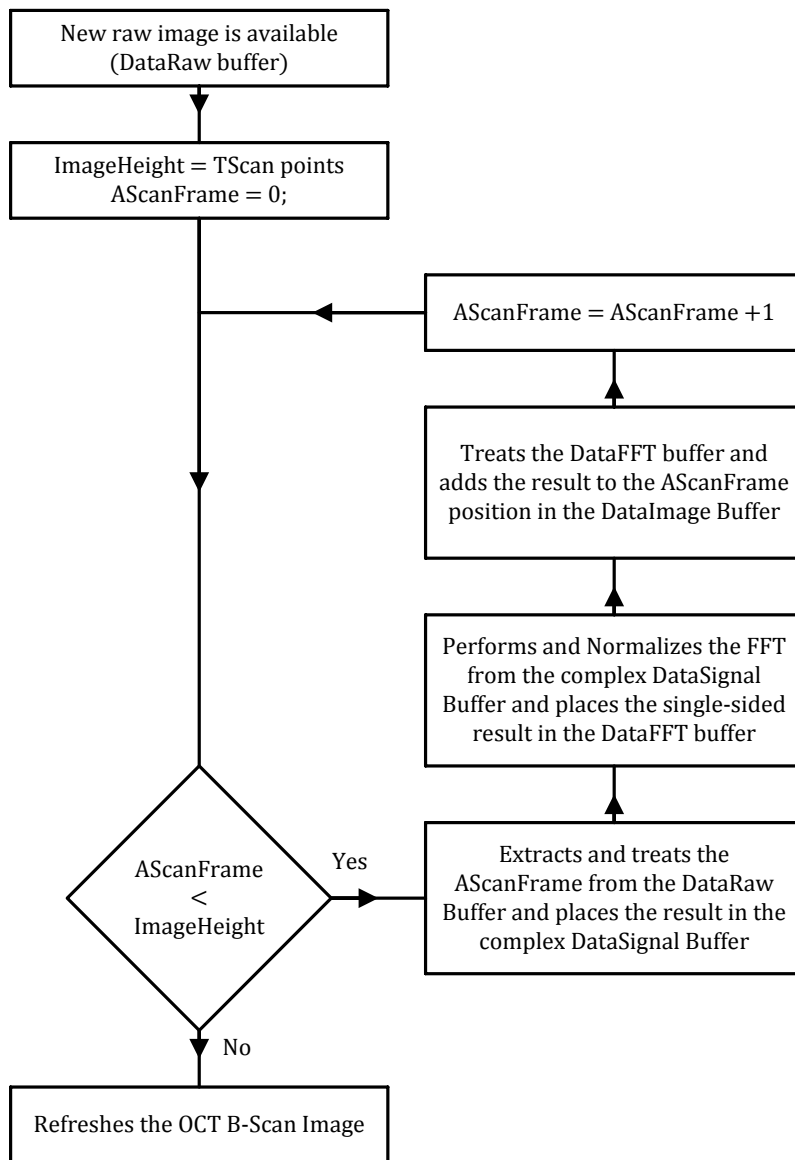


**Fig. 72** - Flowchart of processing and construction of the B-scan image.

# Chapter 5

## Results and Project Analysis

This chapter will focus the analysis of the five most important parameters to characterize an OCT setup. They are: sensitivity, sensitivity roll-off, dynamic range, axial resolution, and imaging speed [55].

Note that, so far, several assumptions have been made that do not apply for real FD-OCT setups. On the one hand, the ability to resolve the spectral components is finite and not infinite as assumed in the theoretical analysis. In SS-OCT,  $\delta\mathbf{k}$  is given by the instantaneous spectral linewidth of the wavelength-swept light source. Assuming a spectral resolution function  $\psi(\mathbf{k})$  centered at  $\mathbf{k} = \mathbf{0}$  with a width  $\delta\mathbf{k}$ , then equation 10 has to be convoluted with  $\psi(\mathbf{k})$ . Due to the convolution theorem, the correct result for  $\mathbf{i}_D(\mathbf{z})$  is obtained by the multiplication of equation 22 with the Fourier transform of  $\psi(\mathbf{k})$ , where the maximum is centered at  $\mathbf{z} = \mathbf{0}$  and the width is proportional to  $1/\delta\mathbf{k}$ . Therefore, the signal  $\mathbf{i}_D(\mathbf{z} = \Delta\mathbf{z})$  decreases with increasing imaging depth  $\Delta\mathbf{z}$  (Fig. 73 and Fig. 74).

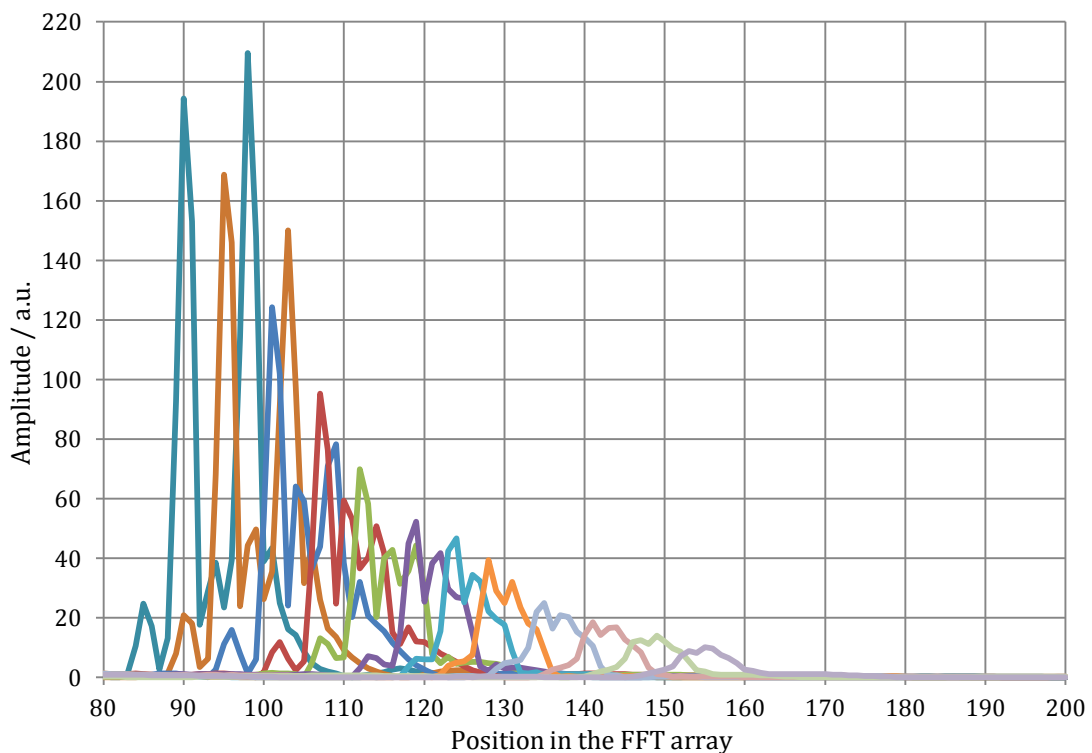


**Fig. 73** – FFT of the interference fringes for twelve positions, equally spaced (0-240  $\mu\text{m}$ ), of the sample arm (mirror). The first position (greater amplitude) is the PSF of the system.

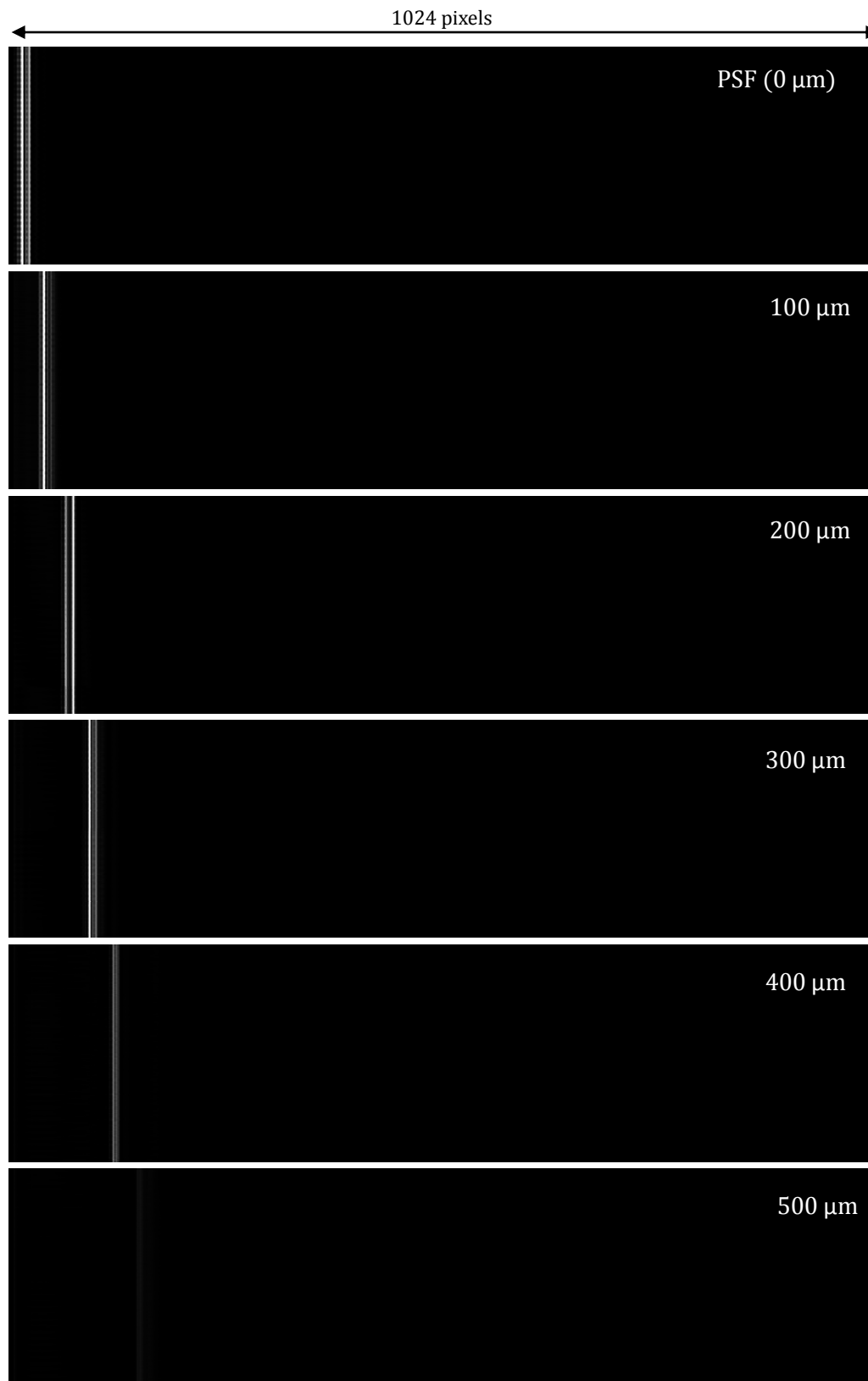
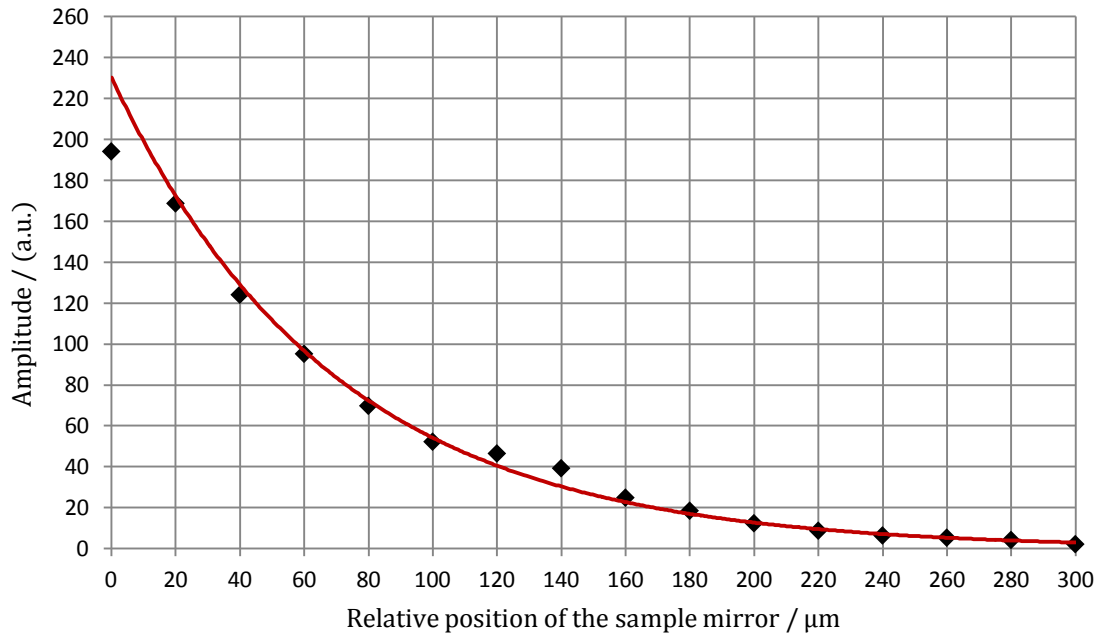


Fig. 74 - Image of the A-Scan for a sample mirror on six different positions (0-500 μm). The galvo is not moving. The first image corresponds to the **PSF** of the system at  $\mathbf{z} = \Delta\mathbf{z}$ .

We can also observe that the signal strength decreases exponentially with depth  $\Delta\mathbf{z}$  (Fig. 75).



**Fig. 75** – Peak of the FFT signal for sixteen positions, equally spaced (0-300  $\mu\text{m}$ ), of the sample arm (mirror). The reference position (0  $\mu\text{m}$ ) is the **PSF** of the system at  $\mathbf{z} = \Delta\mathbf{z}$ .

A measurement of the sensitivity  $S_{\text{dB}}$  at  $\mathbf{z} = \Delta\mathbf{z}$  was performed. This parameter specifies the highest possible attenuation in the sample arm (i.e. the smallest possible back reflection) which can still be detected. It was calculated as twenty times the base-10 logarithm of the ratio of the A-scan peak height  $i_{\text{D}}(\Delta\mathbf{z})$  to the standard deviation of the noise floor  $\sigma(\Delta\mathbf{z})$ .

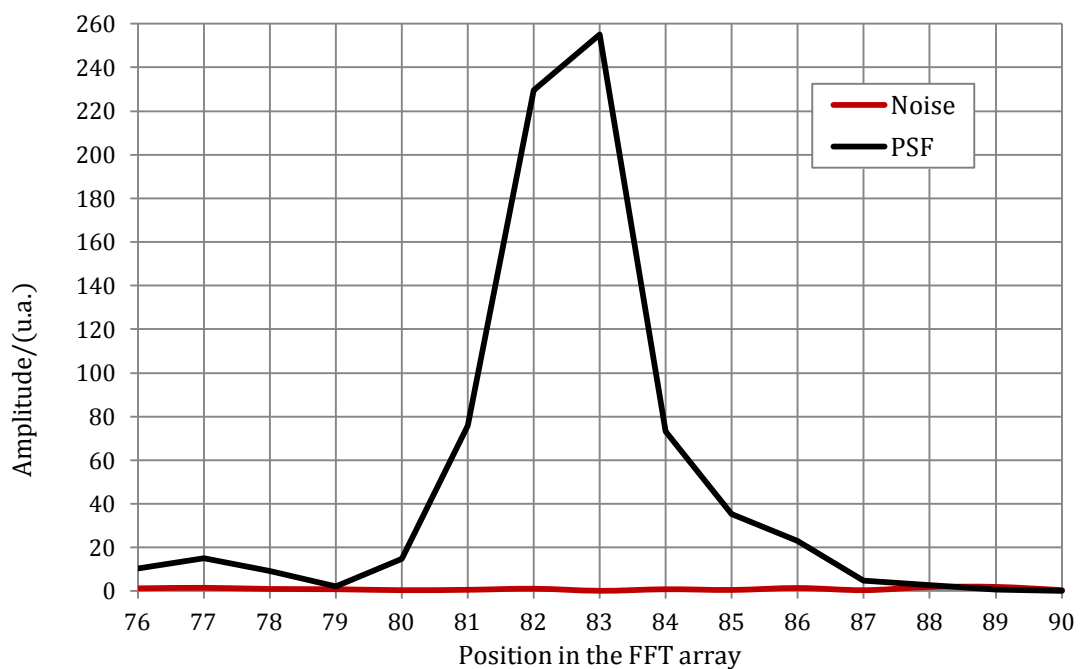


**Fig. 76** - FFT of the PSF (black) and the noise floor (red) in a window centered at  $\mathbf{z} = \Delta\mathbf{z}$ .

The noise floor standard deviation was taken at the location of the A-scan peak by blocking the sample arm (see chapter 2.4.4.).

$$S_{\text{dB}} = 20 \cdot \log\left(\frac{i_D(\Delta z)}{\sigma(\Delta z)}\right) = 20 \cdot \log\left(\frac{255}{0.520}\right) = 53.8 \text{ dB} \quad (58)$$

This value should be improved because it does not yet provide good enough image quality for biomedical applications (the sensitivity should be  $>95\text{dB}$  [55]).

An intrinsic characteristic of FD-OCT is the depth dependent sensitivity roll-off, which, in SS-OCT, is due to the finite instantaneous linewidth  $\delta k$  of the wavelength swept light source [55]. Typically, the experimental determination of this effect is simply carried out by measuring the **PSF** corresponding to different imaging depths  $\Delta z$ . This is accomplished by recording the fringe signal for different reference mirror positions. The same numerical resampling is applied to all fringe signal traces and the resulting Fourier transformed signals  $i_D(\mathbf{z})$  are plotted representing a typical sensitivity roll-off measurement. The sensitivity drop over imaging depth can then be directly derived from the decay of the peaks of the **PSFs**.

The sensitivity roll-off (sensitivity as a function of depth) is often specified in different ways in literature. A common way is to define it through the R-number (a measurement for coherence) which is given by the slope of a linear fit to the peak maxima of the PSFs (logarithmic representation). So, by the analysis of the data on the following figure the R-number value of sensitivity roll-off was found to be  $\approx 10 \mu\text{m}/\text{dB}$ .

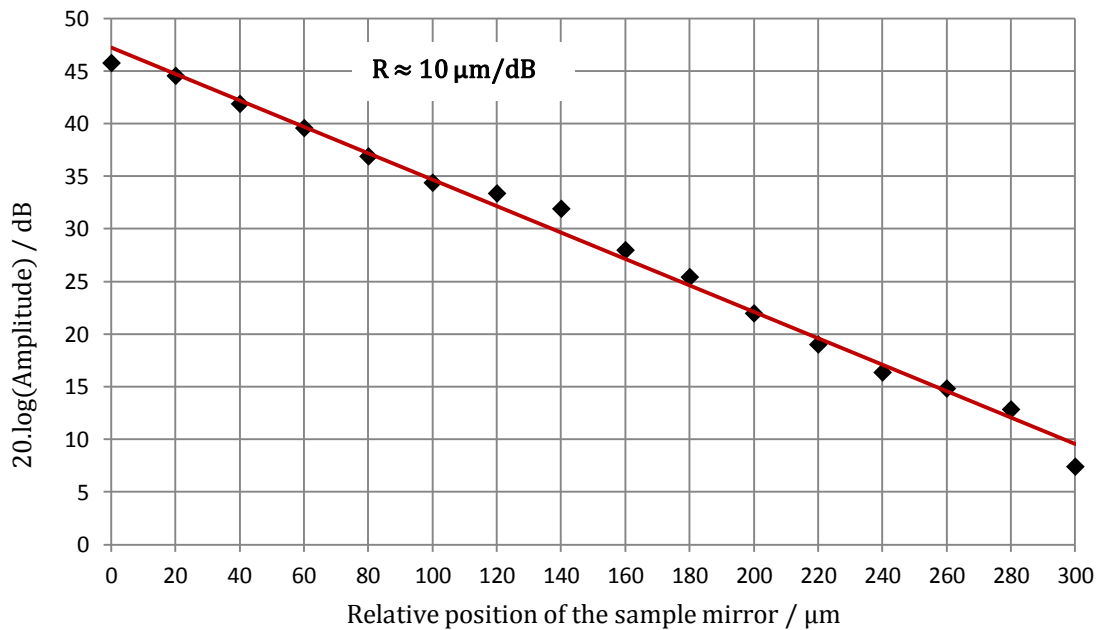


**Fig. 77** - Peak maxima of the FFT for different PSFs depths (logarithmic representation) equally spaced by  $20 \mu\text{m}$  (0-300  $\mu\text{m}$ ).

This value for the sensitivity roll-off is still clearly insufficient. This great decrease in the OCT signal strength with ranging depth is caused mainly by the short focus of the focal lens (ten times lower than it should be). A good OCT system should provide roll-off values of 20 dB or less over 2mm ranging depth, corresponding to R-number values of  $>100 \mu\text{m}/\text{dB}$  [55].

The measurement of dynamic range (ratio in signal strength between the strongest and the weakest reflection), which can be measured simultaneously within one A-scan, was performed similarly to the sensitivity measurement (see chapter 2.4.5.). However, the main difference to the determination of sensitivity is the fact that, here, both measurements have to be done simultaneously and not separately. The standard deviation of the noise floor is typically determined in a window close to the peak at  $\mathbf{z} = \Delta\mathbf{z}$ , where the coherence function  $\gamma(\mathbf{z})$  is negligibly small. Therefore, the dynamic range in logarithmic representation  $D_{\text{dB}}$  reads as follows:

$$D_{\text{dB}} = 20 \cdot \log\left(\frac{i_D(\Delta\mathbf{z})}{\sigma(\Delta\mathbf{z})}\right) = 20 \cdot \log\left(\frac{255}{6.28}\right) = 32.2 \text{ dB} \quad (59)$$

As expected, the dynamic range is typically smaller than the sensitivity but not large enough. OCT imaging quality and imaging range can be affected if the dynamic range is not sufficiently high to enable simultaneous detection of the weakest and the strongest reflections from biological tissue. Biomedical OCT images often have a dynamic range of  $\sim 35\text{dB}$ , so an OCT system should provide 40-50dB [55].

It is also important to establish and analyze the correlation between the FFT signal and the imaging depth  $\Delta\mathbf{z}$ . To do so, the reference mirror is moved with a micrometer in increments of  $20 \mu\text{m}$ , beginning at  $\mathbf{z} = \Delta\mathbf{z}$ . The relative position of the sample arm is then related to the point where the FFT signal has its maximum peak (Fig. 78). As expected, this relationship exhibits a good linearity.

Applying a linear regression to the graph (Fig. 78), each point in the FFT signal corresponds to  $3,43 \mu\text{m}$  in the imaging depth. Therefore, we can assume this value as the maximum possible axial resolution  $\delta\mathbf{z}$  of the system. This value meets with the theoretical value provided by this swept source obtained in chapter 3.2.3. ( $4,34 \mu\text{m}$ ), taking into account that this theoretical value is based on the assumption that the refractive index of the sample arm  $\mathbf{n} = 1$  and the spectral power exhibit a Gaussian shape.

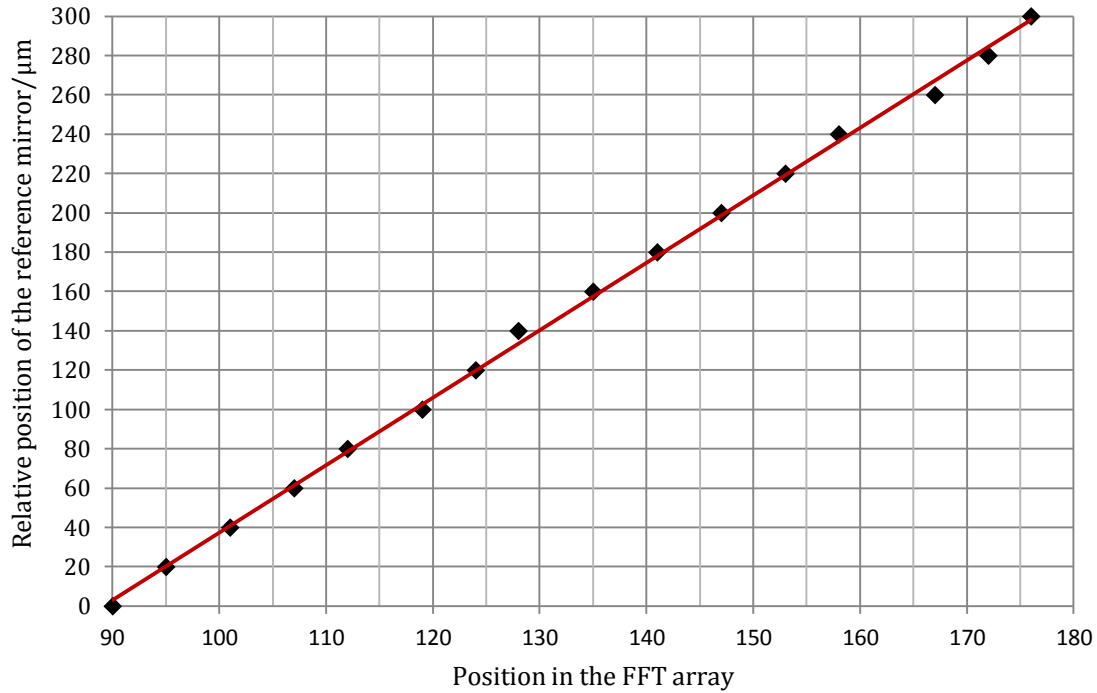


**Fig. 78** - Correlation between the FFT signal and the imaging depth  $\Delta z$ . The reference mirror is moved with a micrometer in increments of  $20 \mu\text{m}$  (0-300 $\mu\text{m}$ ).

Assuming a depth of focus  $\Delta z_f$  (see chapter 2.4.3.) equal to the depth of view  $\text{DOV}=0.58 \text{ mm}$  of the lens (see chapter 2.4.5.) and considering the previous relationship, the maximum number of depth points in the FFT after the best **PSF** ( $z = \Delta z$ ) is  $\approx 170$ . This value is consistent with the results achieved (Fig. 79).



**Fig. 79** - Image of the A-Scan for a sample mirror in position 0 and 500  $\mu\text{m}$ . The galvo is not moving. The first A-Scan corresponds to the **PSF** of the system at  $z = \Delta z$ .

Again, for greater depth information, it is important that the lens is replaced by another one with a higher depth of view  $\approx 5 \text{ mm}$  (see chapter 3.2.3 equation 51).

Another important result is the real axial resolution  $\delta z$  of the system. This can be obtained by measuring the full-width of half maximum (FWHM) of the signal peak of the FFT for a **PSF** corresponding to the imaging depth at  $z = \Delta z$  (Fig. 80).



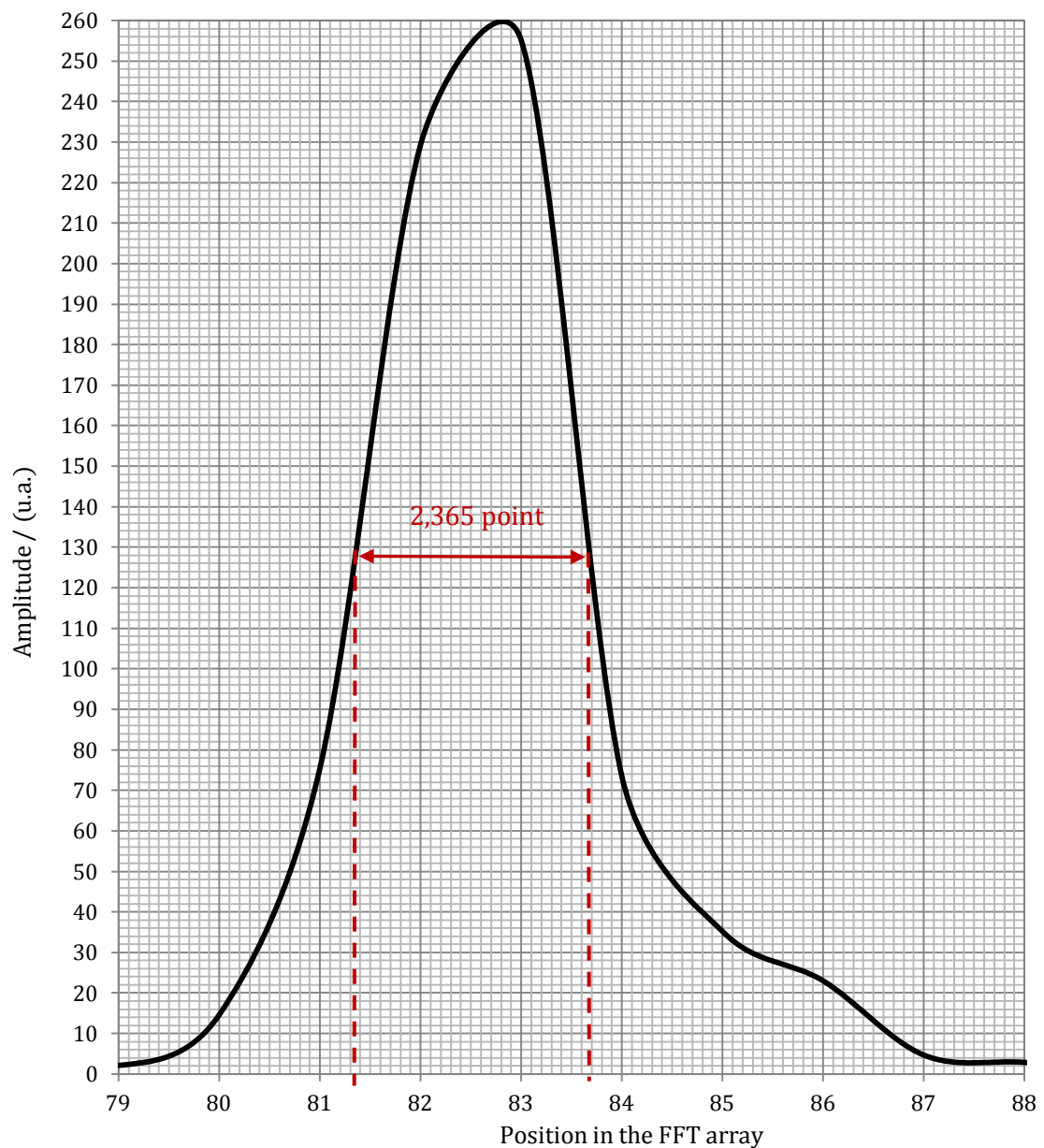


**Fig. 80** – Measurement of FWHM of the signal peak of the FFT for a **PSF** corresponding to the imaging depth at  $z=\Delta z$ .

Taking into account that the FFT of the interference signal exhibits a Gaussian shape and that each FFT point corresponds to  $3.43 \mu\text{m}$  in depth, the best value obtained for the axial resolution is  $\approx 8.1 \mu\text{m}$ . This is a good result because, to obtain a good image quality in biomedical applications, the resolution in tissue should be  $\leq 10 \mu\text{m}$  [55].

Imaging speed in OCT can be defined by the number of depth scans (A-Scans) per second or by the number of frames per second (B-Scans) [55].

In this phase of the project, the system is already capable of displaying B-Scan image for preview. For a B-Scan image with a dimension of  $1024 \times 256$  points (A-Scan  $\times$  T-Scan) the time period for displaying the image is  $\approx 175$  ms (5-6 images per second).

The following figure displays four B-Scan images for different T-Scan ranges (256, 512 and 1024). The sample arm is a mirror and the mechanical scan angle of the X-axis mirror is  $2^\circ$  for the three images on the left and  $1^\circ$  for the rightmost image.

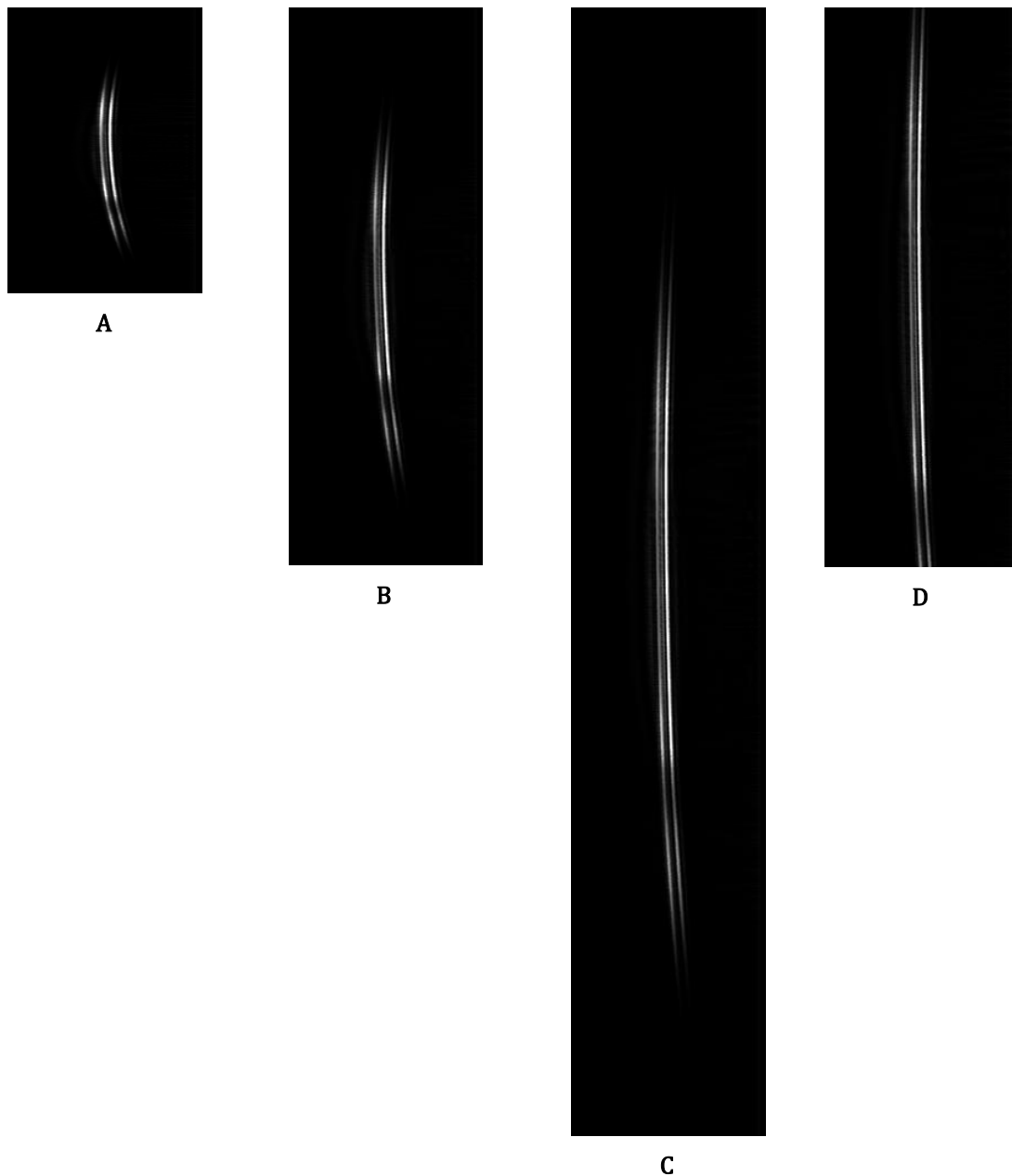


**Fig. 81** – B-Scan images for four different T-Scan ranges positions (256 - A, 512 - B and D, 1024 - C). The mechanical scan angle of the X-axis mirror is  $1^\circ$  (D) and  $2^\circ$  (A, B and C). The sample arm is a mirror.

The interference signal does not cover the whole picture (Fig. 81 - A, B and C) because the scan angle is double than what it is possible for the current assembly (see equation 57, chapter 3.7. and the example in chapter 4.5.). In this condition and for the

images on figure 81 the calculated value for the lateral resolutions in the focus is  $\approx 73.4 \mu\text{m}$  (image A),  $36.7 \mu\text{m}$  (image B) and  $18.4 \mu\text{m}$  (images C and D). Note that the lateral resolution is limited by the lens beam diameter in the field of focus (for the lens used is  $\approx 21 \mu\text{m}$ ).

A problem, still unresolved, is the double line that shows on the picture. Because the sample arm is a mirror, a simple line should be expected corresponding to a simple reflection (A-scan) for each T-scan. A hypothetical reason derives from the fact that the mirror used in the sample arm is a household glass mirror (coated on the back surface) and not an optical mirror (coated on the front). Remember that with a household glass mirror the reflecting surface (usually a thin layer of aluminum or silver) is placed on the back of the mirror and then covered with a protective layer. This means that, although the main reflected light comes from this surface, it will also be reflected from the front surface of the glass. This will give a secondary reflection which is weaker than the main one.

One more consideration, not yet tested, is the fact that the electric fields returning from both interferometer arms and superposing in the fiber coupler do not have the same polarization because the polarization state in standard single mode fiber is not preserved and can change considerably. Note that, because a balanced receiver has been used, much of the excess noise has identical time dependence in both detectors and is therefore cancelled. The dominant remaining noise contribution at moderate optical powers is often shot noise. However, in this configuration, the phase difference between the beams arriving at the two inputs of the detector for stray shows incoherent beams arising from unwanted reflections. The solution is to use a fiber polarization controller in, at least, one interferometer arm [56]. As it can be seen in Fig. 82, Zhang *et al.* [56] applied this solution with promising results (better sensitivity and SNR).

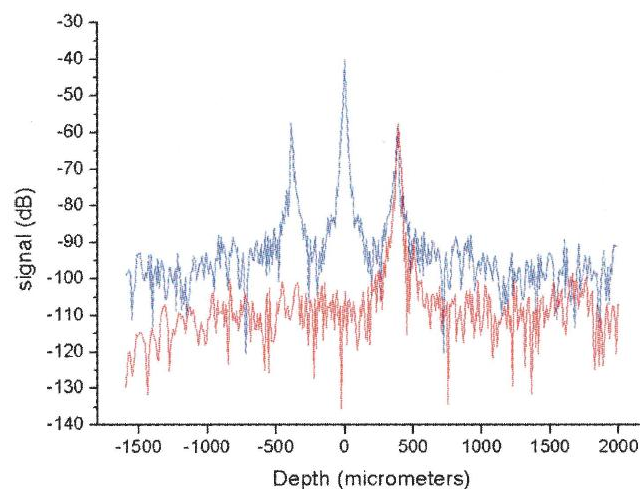


**Fig. 82** - Sensitivities measured with a 57.6dB reflector. Blue, without an EO (electro-optic phase modulator) phase modulator; red, with an EO phase modulator [56].



# Chapter 6

## Conclusion and Future Work

The most important at this moment for the physical enhancement part is in improving the pre-objective scanning setup and the sensitivity of the system.

The improvement of the first is made by changing the focal sample arm lens and shortening the distance between the galvo mirrors and the referred lens. The new lens must have a depth of view (greater depth information in the A-scan range) about  $\approx 6$  mm (to match the depth range of the laser) and a spot size as small as possible (to allow more lateral resolution). Note that, objective lenses with a lower numerical aperture decrease the lateral resolution which is always committed with depth of focus: increasing lateral resolution implies reducing depth of focus.

With the concrete implemented setup shortening the distance between the galvo mirrors and the lens, it will allow larger scan angle and therefore better lateral resolution or bigger T-scan range. Alternatively, we can use a lens with a small magnification or a larger field of view. So this way we can take advantage of the maximum scan angle of the galvo.

For a better sensibility, a component to control polarization can be included in the system. The goal is to improve the breadth and signal quality, since the interference generated by the superposition of beams on the photodetector is influenced by each beam polarization plan (only when both have the same polarization, the maximum interference occurs, corresponding to a minimum width in destructive interference and a maximum in constructive interference).

The processing and displaying of signals by the developed program is also subject to several object improvements. One of the most important is to optimize the image speed reconstruction algorithm as well as a better method for the synchronization between the position of the galvo and the data acquisition. The other one is to automatically store, into a data file, all data acquired over a B-scan and not just by sampling.

Another step to be developed in future works is to improve imaging: currently, the program generates two-dimensional images in amplitude scale with no posterior treatment. It is necessary to use algorithms to improve the contrast of the image and allow the visualization of the details that produce lower signal amplitude. One of the techniques

for this purpose is the generation of the image in false colors instead of grayscale. In the future, the incorporation of neighboring scans interpolation in the program is also aimed to improve the sharpness of the image. Finally, it is desired to have image sample in 3D from the union side scans.

The current developed program provides flexible control of the data acquisition and control over the system, and it is already possible to acquire B-scan images. This advancement in the project allows the automation of the OCT process and enables performing the first measurements of the key parameters for the OCT (see chapter 5). The results are still below the intended and should be improved in future works.

# Bibliography

- [1] Duguay, M. A.; Mattick, A. T.. **Ultrahigh Speed Photography of Picosecond Light Pulses and Echoes**. Applied Optics, vol. 10, no. 9, pages: 2162-2170, Sep. 1971.
- [2] Bruckner, A. P.. **Picosecond light scattering measurements of cataract microstructure**. Applied Optics, vol. 17, no. 19, pages: 3177-3183, Oct. 1978.
- [3] Fujimoto, J. G.; Silvestri, S.; Ippen, E. P.; Puliafito, C. A.; Margolis, R.; Oseroff, A.. **Femtosecond optical ranging in biological systems**. Optics Letters, vol. 11, no. 3, pages: 150-152, Mar. 1986.
- [4] Fercher, A. F.; Mengedoht, K.; Werner, W.. **Eye-length measurement by interferometry with partially coherent light**. Optics Letters, vol. 13, no. 3, pages: 186-188, Mar. 1988.
- [5] Clivaz, X.; Marquis-Weible, F.; Salathé, R. P.; Novák, R. P.; Gilgen, H. H.. **High-resolution reflectometry in biological tissues**. Optics Letters, vol. 17, no. 1, pages: 4-6, Jan. 1992.
- [6] Huang, D.; Swanson, E. A.; Lin, C. P.; Schuman, J. S.; Stinson, W. G.; Chang, W.; Hee, M. R.; Flotte, T.; Gregory, K.; Puliafito, C. A.; Fujimoto, J. G.. **Optical Coherence Tomography**. Science, New Series, vol. 254, no. 5035, pages: 1178-1181, Nov. 1991.
- [7] Brezinski, M. E.. **Optical Coherence Tomography-Principles and Application**. ISBN 978-0-12-133570-0, Academic Press - Elsevier (Burlington, USA), 2006.
- [8] Drexler, W.; Fujimoto, J. G.. **Optical Coherence Tomography: Technology and Applications (Biological and Medical Physics, Biomedical Engineering)**. ISBN 978-3-540-77549-2, Springer, Set. 2008.
- [9] Bouma, B. E.; Tearney G. J.. **Handbook of Optical Coherence Tomography**. ISBN 0-8247-0558-0, Marcel Dekker Inc. (New York, USA), 2002.
- [10] Swanson, E. A.; Huang, D.; Hee, M. R.; Fujimoto, J. G.; Lin, C. P.; Puliafito, C. A.. **High-speed optical coherence domain reflectometry**. Optics Letters, vol. 17, no. 2, pages: 151-153, Jan. 1992.

- [11] Fercher, A. F.; Hitzenberger, C. K.; Kamp, G.; Elzaiat, S. Y.. **Measurement of Intraocular Distances by Backscattering Spectral Interferometry.** Optics Communications, no. 117, pages: 43-48, 1995.
- [12] Wojtkowski, M.; Leitgeb, R.; Kowalczyk, A.; Bajraszewski, T.; Fercher, A. F.. ***In vivo* human retinal imaging by Fourier domain optical coherence tomography.** Journal of Biomedical Optics, vol. 7, no. 3, pages:457-463, Jul. 2002.
- [13] Chinn, S. R.; Swanson, E. A.; Fujimoto, J. G.. **Optical coherence tomography using a frequency-tunable optical source.** Optics Letters, vol. 22, no. 5, pages: 340-342, Mar. 1997.
- [14] Choma, M. A.; Sarunic, M. V.; Yang, C.; Izatt, J. A.. **Sensitivity advantage of swept source and Fourier domain optical coherence tomography.** Optics Express, vol. 11, no. 18, pages 2183-2189, Sep. 2003.
- [15] Leitgeb, R.; Hitzenberger, C. K.; Fercher, A. F.. **Performance of fourier domain vs. time domain optical coherence tomography.** Optics Express, vol. 11, no. 8, pages: 889-894, Apr. 2003.
- [16] Murali, S.; Rolland, J.. **Dynamic-focusing Microscope Objective for Optical Coherence Tomography.** International Optical Design Conference 2006, SPIE Digital Library, vol. 6342, Jul 2006.
- [17] Yun, S. H.; Tearney, G. J.; Boer, J. F. de; Bouma, B. E.. **Motion artifacts in optical coherence tomography with frequency-domain ranging.** Optics Express, vol. 12, issue 13, pages: 2977-2998, Jun 2004.
- [18] Hendargo, H. C.; McNabb, R. P.; Dhalla, A.; Shepherd, N.; Izatt, J. A.. **Doppler velocity detection limitations in spectrometer-based versus swept-source optical coherence tomography.** Biomedical Optics Express, vol. 2, issue 8, pages: 2175-2188, 2011.
- [19] Nezam, S. M. R. M.; Vakoc, B. J.; Desjardins, A. E., Tearney, G. J.; Bouma, B. E.. **Increased ranging depth in optical frequency domain imaging by frequency encoding.** Optics Letters, vol. 32, no. 19, pages: 2768-2770, Oct. 2007.
- [20] Biedermann, B. R.; Wieser, W.; Eigenwillig, C. M.; Klein, T.; Huber, R.. **Dispersion, coherence and noise of Fourier domain mode locked lasers.** Optics Express, vol. 17, no. 12, pages: 9947-9961, Jun. 2009.



- 
- [21] Lee, S. W.; Song, H. W.; Jung, M.-Y.; Kim, S.-H.. **Wide tuning range wavelength-swept laser with a single SOA at 1020 nm for ultrahigh resolution Fourier-domain optical coherence tomography**. Optics Express, vol. 19, no. 22, pages: 21227-21237, Oct. 2011.
- [22] Rollins, A. M.; Izatt, J. A.. **Optimal interferometer designs for optical coherence tomography**. Optics Letters, vol. 24, no. 21, pages: 1484-1486, Nov. 1999.
- [23] Anderson, L. K.; McMurtry, B. J.. **High-Speed Photodetectors**. Applied Optics Express, vol. 5, no. 10, pages: 1573-1587, Oct. 1996.
- [24] Podoleanu, A. G.. **Unbalanced versus balanced operation in an optical coherence tomography system**. Applied Optics, vol. 39, no. 1, pages: 173-182, Jan. 2000.
- [25] Schuman, J. S.; Puliafito, C. A.; Fujimoto J. G.; Duker, J. S.. **Optical Coherence Tomography of Ocular Diseases**. ISBN 978-1-55642-864-7, 3<sup>rd</sup> ed., SLACK Inc. (Thorafare, USA), 2010.
- [26] Fujimoto, J. G.. **Optical coherence tomography for ultrahigh resolution *in vivo* imaging**. Nature Biotechnology, Nature Publishing Group, vol. 21, no. 11, pages: 1361-1367, Nov. 2003.
- [27] Sattler, E.; Kästle, R.; Welzel, J.. **Optical coherence tomography in dermatology**. Journal of Biomedical Optics, vol. 18 (issue 6), pages: 061224-1 to 061224-6, Jun. 2013.
- [28] Chen Y. L.; Zhang, Q.; Zhu, Q.. **Optical Coherence Tomography in Dentistry, Selected Topics in Optical Coherence Tomography, Dr. Gangjun Liu (Ed.)**. ISBN 0-13-946053-5, InTech Europe (Rijeka, Croatia), Feb. 2012.
- [29] Haus, H. A.. **Waves and Fields in Optoelectronics**. ISBN 978-953-51-0034-8, Solid state physical electronics, Prentice-Hall Inc. (New Jersey, USA), 1984.
- [30] Webb, R. H.; Hughes, G. W.; Pomerantzeff, O.. **Flying spot TV ophthalmoscope**. Applied Optics, vol. 19, no. 17, pages: 2991-2997, Sep. 1980.
- [31] Swanson, E. A.; Izatt, J. A.; Hee, M. R.; Huang, D.; Lin, C. P.; Schuman, J. S.; Puliafito, C. A.; Fujimoto, J. G.. ***In vivo* retinal imaging by optical coherence tomography**. Optics Letters vol. 18, no. 21, pages: 1864-1866, Nov. 1993.

- [32] Radhakrishnan, S.; Rollins, A. M.; Roth, J. E.; Yazdanfar, S.; Westphal, V.; Bardenstein, D. S.; Izatt, J. A.. **Real-time optical coherence tomography of the anterior segment at 1310 nm.** Archives of Ophthalmology, vol. 119, pages: 1179-1185, Aug. 2001.
- [33] Brezinski, M. E.; Tearney, G. J.; Bouma, B. E.; Izatt, J. A.; Hee, M. R.; Swanson, E. A.; Southern, J. F.; Fujimoto, J. G.. **Optical coherence tomography for optical biopsy - Properties and demonstration of vascular pathology.** American Heart Association, Circulation, vol. 93, issue 6, pages: 1206-1213, Mar. 1996.
- [34] Chen, Z.; Milner, T. E.; Srinivas, S.; Wang, X.; Malekafzali, A.; Gemert, M. J. C.; Nelson, J. S.. **Noninvasive imaging of *in vivo* blood flow velocity using optical Doppler tomography.** Optics Letters, vol. 22, no. 14, pages: 1119-1121, Jul. 1997.
- [35] Ding, Z. H.; Zhao, Y. H.; Ren, H. W.; Nelson, J. S.; Chen, Z. P.. **Real-time phase-resolved optical coherence tomography and optical Doppler tomography.** Optics Express, vol. 10, no. 5, pages: 236-245, Jan. 2002.
- [36] Hee, M. R.; Huang, D.; Swanson, E. A.; Fujimoto, J. G.. **Polarization-Sensitive Low-Coherence Reflectometer for Birefringence Characterization and Ranging.** Journal of the Optical Society of America B, Optical Physics, vol. 9, no. 6, pages: 903-908, Jun. 1992.
- [37] Boer, J. F.; Milner, T. E.; Nelson, J. S.. **Determination of the depth-resolved Stokes parameters of light backscattered from turbid media by use of polarization-sensitive optical coherence tomography.** Optics Letters, vol. 24, no. 5, pages: 300-302, Mar. 1999.
- [38] Morgner, U.; Drexler, W.; Kartner, F. X.; Li, X. D.; Pitris, C.; Ippen, E. P.; Fujimoto, J. G.. **Spectroscopic optical coherence tomography.** Optics Letters, vol. 25, no. 2, pages: 111-113, Jan. 2000.
- [39] Koch, P.; Huttmann, G.; Schleiermacher, H.; Eichholz, J.; Koch, E.. **Linear OCT system with down conversion of the fringe pattern.** Coherence Domain Optical Methods and Optical Coherence Tomography in Biomedicine VIII, SPIE, vol. 5316, pages: 260-267, 2004.
- [40] Dubois, A.; Grieve, K.; Moneron, G.; Lecaque, R.; Vabre, L.; Boccara, C.. **Ultrahigh-resolution full-field optical coherence tomography.** Applied Optics, vol. 43, no. 14, pages: 2874-2883, May. 2004.

- 
- [41] Frosz, M. H.; Juhl, M.; Lang, M. H.. **Optical Coherence Tomography: System Design and Noise Analysis**. ISBN 87-550-2904-3, Risø National Laboratory (Roskilde, Denmark), Jul. 2001.
- [42] Tomlins, P H.; Wang, R. K.. **Theory, developments and applications of optical coherence tomography**. Institute of Physics Publishing, Journal of Physics D: Applied Physics, vol. 38, no. 15, pages: 2519-2535, Jul. 2005.
- [43] Xi, J.; Huo, L.; Li, J.; Li, X.. **Generic real-time uniform K-space sampling method for high-speed swept-Source optical coherence tomography**. Optics Express, vol. 18, no. 9, pages: 9511-9517, Apr. 2010.
- [44] Hale, G. M.; Querry, M. R.. **Optical Constants of Water in the 200-nm to 200-um Wavelength Region**. Applied Optics, vol. 12, no. 3, pages: 555-563, Mar. 1973.
- [45] Bashkatov, A. N.; Genina, E. A.; Kochubey, V. I.; Tuchin, V. V.. **Optical properties of human skin, subcutaneous and mucous tissues in the wavelength range from 400 to 2000 nm**. Institute of Physics Publishing, Journal of Physics D: Applied Physics, vol. 38, no. 15, pages: 2543-2555, Jul. 2005.
- [46] Biedermann, B. R.; Wieser, W.; Eigenwillig, C. M.; Huber, R.. **Recent developments in Fourier Domain Mode Locked lasers for optical coherence tomography: Imaging at 1310 nm vs. 1550 nm wavelength**. Journal of Biophotonics vol. 2, issue 6-7, pages: 357-363, Jul. 2009.
- [47] **Axsun OCT Swept source engine – Operator Manual (Rev. 11)**. Axsun Technologies, Inc. (Massachusetts, USA), 2010.
- [48] **Axsun Technologies - OCT Capabilities**. SPIE BIOS. Axsun Technologies, Inc. (Massachusetts, USA), Jan. 2010.
- [49] Choma, M. A.; Yang, C.; Izatt, J. A.. **Instantaneous quadrature low-coherence interferometry with 3x3 fiber-optic couplers**. Optics Letters, vol. 28, no. 22, Nov. 2003.
- [50] **PDB100 Series Balanced Amplified Photodetectors - Operation Manual V1.3**. Thorlabs Inc. Instrumentation (Germany), Apr. 2007.
- [51] **X5-400M - User's Manual Rev. 1.01**. Innovative Integration (California, USA), Nov. 2011.

- [52] **NI 6010 Specifications.** National Instruments Corporation (Redmond, USA), Mar. 2005.
- [53] **Scanning Galvo Systems - User Guide Rev. 16.** Thorlabs Inc. (New Jersey, USA), Aug. 2012.
- [54] Thorlabs Inc. (New Jersey, USA). Online in 14 Aug. 2013.  
<http://www.thorlabs.com/>
- [55] Wieser, W.; Biedermann, B. R.; Klein, T.; Eigenwillig, C. M.; Huber, R. **Multi-Megahertz OCT: High quality 3D imaging at 20 million A-scans and 4.5 GVoxels per second.** Optics Express, vol. 18, no. 14, pages: 14685-14704, Jul. 2010.
- [56] Zhang, J.; Nelson, J. S.; Chen, Z.. **Removal of a mirror image and enhancement of the signal-to-noise ratio in Fourier-domain optical coherence tomography by use of an electro-optical phase modulator.** Optics Letters, vol. 30, no. 2, Jan. 2015.
- [57] Anjul, A. M. D. **Development of Fourier domain optical coherence tomography for applications in developmental biology.** Dissertation submitted in partial fulfillment of the requirements for the degree of Doctor of Philosophy in the Department of Biomedical Engineering in the Graduate School of Duke University, 2008.
- [58] **GMAX™ SYSTEMS Multi-Axis Beam Handling – Reference Manual Rev. E.** GSI Lumonics (Wilmington, USA), 1996.